

**Simulation of flow and Sediment Transport in an Open Channel with
Obstacle using IRIC NAYS2DH**



Masuma Haque

**Department of Civil Engineering
Khulna University of Engineering and Technology
Khulna-9203, Bangladesh
May, 2018**

Simulation of flow and Sediment Transport in an Open Channel with Obstacle using IRIC NAYS2DH

A Project Report Submitted to the Department of Civil Engineering, Khulna Khulna University of Engineering and Technology in Partial Fulfillment of the Requirements for the Degree of

“Masters of Science in Civil Engineering”

Supervised by:

Dr. Md. Shahjahan Ali

Professor

Department of Civil Engineering

KUET, Khulna-9203

Prepared by

Masuma Haque

Roll No: 1301509

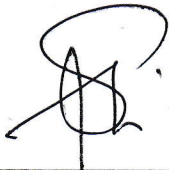
Department of Civil Engineering

KUET, Khulna-9203

**Department of Civil Engineering
Khulna Khulna University of Engineering and Technology
Khulna-9203, Bangladesh
May, 2018**

Declaration

This is to certify that the thesis work entitled “ Simulation of Flow and Sediment Transport in an Open channel with Obstacle using IRIC NAYS2DH” has been carried out by Masuma Haque in Department of Civil Engineering, Khulna University of Engineering & Technology, Khulna, Bangladesh. The above thesis work or any part of this work has not been submitted anywhere for the award of any degree or diploma.



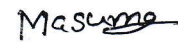
Dr. Md. Shahjahan Ali

(Supervisor)

Professor

Department of Civil Engineering

KUET, Khulna-9203




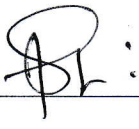
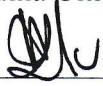
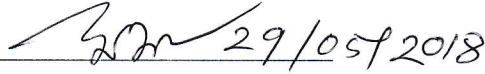
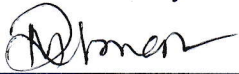
Masuma Haque

Roll No: 1301509

Approval

This is to certify that the thesis work submitted by **Masuma Haque** entitled '*Simulation of Flow and Sediment Transport in an Open Channel with Obstacle using iRIC Nays2DH*' has been approved by the board of examiners for the partial fulfillment of the requirements for the degree of *Master of Science in Civil Engineering* in the Department of Civil Engineering, Khulna University of Engineering & Technology, Khulna, Bangladesh in May 29, 2018.

BOARD OF EXAMINERS

1. 
_____ Chairman
(Supervisor)
Dr. Md. Shahjahan Ali
Professor, Department of Civil Engineering
Khulna University of Engineering & Technology
2. 
_____ Member
Dr. Md. Shahjahan Ali
Head, Department of Civil Engineering
Khulna University of Engineering & Technology
3. 
_____ Member
Dr. Kh. Md. Shafiul Islam
Professor, Department of Civil Engineering
Khulna University of Engineering & Technology
4. 
_____ Member
Dr. Khondoker Mahbub Hassan
Professor, Department of Civil Engineering
Khulna University of Engineering & Technology
5. 
_____ Member
(External)
Dr. Md. Munsur Rahman
Professor, Institute of Water and Flood Management
Bangladesh University of Engineering & Technology

ACKNOWLEDGEMENT

All praises go to almighty Allah, the most magnificent merciful. The author gratefully acknowledge their profound gratitude and indebtedness to project supervisor, prof. Dr. Md. Shahjahan Ali, Assistant professor, Department of Civil Engineering, Khulna University of Engineering & Technology (KUET) for his keen interest in this project, continuous supervision, guidance, encouragement, inspiration and thoughtful suggestion in completing the work.

Finally author would like to express her gratitude to all the faculty members of the Department for their kind Co-operation.

ABSTRACT

Hydraulic structures such as barbs, groins and spur dikes have been constructed in river bank in order to deflect the flowing water away from vulnerable zone. They are made of stone, gravel, rock, earth or piles, beginning at the river bank with a root and ending the regulation line with a head. River flow mechanisms with the hydraulic structures need to be intensively studied to protect the river bank from erosion, increase the bank stability, improve navigation and flood control. Such structure also plays an important role to enrich the biodiversity of different aquatic species by providing shelter them. The main objective of this thesis is to simulate the straight channel with the presence of several types of such structures by using 2D numerical simulation model, iRIC Nays2DH. The groin like structures can be oriented perpendicular or be inclined either upstream or downstream. Each orientation affects the stream in a different way and shows different result in the vicinity of the groin. In chapter, simulation of flow around groin, details of streamline variation, velocity vector and computed recirculation around groin are shown for 45°, 90° and 135° groin. The length of recirculation zone is found 1.2m, 1.04m and 1m, respectively. The simulated present study of velocity profiles and shear stress profiles are compared with previous experimental and numerical results. Good agreement is found for all of the cases. It is observed that predicted velocity profiles and predicted bed shear stress profiles for 45°, 90° and 135°, the position of maximum velocity and shear stress are found to be shifted towards downstream with increasing $y/l = 1, 1.5, 2, 3$ and 4 , respectively. For all the cases, peak of the velocity and shear stress are also deviated from upstream to downstream, 45° to 135° angled groin. From the velocity contour and shear stress contour, it is found that left bank is higher velocity and higher shear stress zone and right bank is lower velocity and lower shear stress zone. In chapter, local scour around groin, to determine the variation of scour depth and sediment deposition near the head of the groin, groins are orientated 45°, 90° and 135° at the upstream of the channel. The comparison of velocity field, bed level contour results, Elevation of bed profiles of 45°, 90° and 135° groin are given. Simulated present study are compared with previous numerical results and good agreement are found. 45°, 90° and 135° groin are simulated for 1 hour and 5 hours, respectively. After 5 hours, equilibrium scour is attended and maximum scour depth for 45°, 90° and 135° are found as 0.065m, 0.062m and 0.054m, respectively. In case of multiple groin, maximum scour are found 0.145m for discharge $0.035 \text{ m}^3/\text{s}$ and 0.24m for discharge $0.046 \text{ m}^3/\text{s}$. Bed deformation contour lines, velocity vectors, transverse and longitudinal bed profiles are depict in this chapter. Computed scouring are compared with previous experimental and numerical results. For discharge, $0.035 \text{ m}^3/\text{s}$, scour at first spur dikes to third spur dikes are 0.123m, 0.005m and 0.005m, respectively. Similarly, when discharge $0.046 \text{ m}^3/\text{s}$, scour at first to third spur dikes are 0.16m, 0.01m and 0.012m, respectively. The model is also used to evaluate and analyze flow patterns, streamline variation, velocity vector contour, vorticity, bed shear stress contour, scour and sediment deposition around a groin like structure on a straight channel.

Most of the natural flow are three dimensional; for example, in case of meandering channel, the flow passing through the bend is obviously of a three-dimensional (3D) nature because of the generation of secondary current due to the centrifugal force. When a flow in an open

channel passes an obstacle (such as groin), the deviation of flow causes the generation of secondary current and flow become highly 3D. Therefore, a 3D hydrodynamic model is necessary to accurately simulate the flows in a meandering channel. However, dealing with the practical engineering problems, such as alluvial geomorphic process, it is not computationally efficient to use 3D models. In such problems, a two-dimensional (2D) model is generally used. To predict the applicability of iRIC software in a flow field with strong secondary current, the model is also applied for 180° sharp and mildly bend. Water surface elevation contour and velocity vector are evaluated from the simulation. For both cases, the velocity of flow is greater in the inner section than the outer section. The results are compared with previous experiment result and found well agreed with previous experiments.

Table of Contents

ABSTRACT.....	i
ACKNOWLEDGEMENT	ii
TABLE OF CONTENTS.....	iii
LIST OF TABLES	vi
LIST OF FIGURES	vii
Chapter 1 INTRODUCTION	1
1.1 GENERAL.....	1
1.2 OBJECTIVE OF THE STUDY	3
1.3 ORGANIZATION OF THE REPORT	3
Chapter 2 LITERATURE REVIEW	4
2.1 INTRODUCTION	4
2.2 REVIEW OF PREVIOUS STUDIES	4
2.3 GENERALIZED SIMULATION PROCEDURE.....	5
2.3.1 Simulation and modeling	5
2.3.2 Summary of simulation process	5
2.3.3 Components of a numerical solution method	6
2.3.4 Discretization approaches	6
2.3.4.1 Finite Difference Method.....	7
2.3.5 Numerical grid	8
2.3.6 Properties of numerical simulation methods.....	8
2.3.7 Courant number	11
2.4 iRIC SOFTWARE	11
2.4.1 Features of the flow field calculation model	12
2.4.2 Features of the sediment transport and riverbed deformation calculation	13
2.4.3 other feathers.....	14
2.5 BASIC EQUATIONS.....	14
2.5.1 Basic flow equations	14
2.5.1.1 Basic equations in orthogonal coordinates.....	14
2.5.1.2 Transformation into general curvilinear coordinates	15
2.5.1.3 Basic equations in a general curvilinear coordinate system	16

2.5.2 Turbulent field calculation method	18
2.5.2.1 Constant eddy viscosity	18
2.5.2.2 Zero-equation model	18
2.5.2.3 K- ϵ model	19
2.5.3 Bottom friction calculation method	19
2.5.3.1 Constant value	19
2.5.4 Method of calculating resistance by vegetation	20
Chapter 3 SIMULATION TECHNIQUES	21
3.1 INTRODUCTION	21
3.2 SIMULATION TECHNIQUES	21
3.3 NAYS2DH	23
3.4 OPERATIONAL PROCEDURES	23
3.5 FLOW PARAMETERS	23
3.6 COMPUTATIONAL SCHEMES AND FLOW DOMAIN	25
Chapter 4 SIMULSTION OF FLOW AT A BEND	33
4.1 Introduction	33
4.2 Simulated result of 180° sharply curved channel	35
4.3 Simulated result of Mildly curved channel	38
Chapter 5 SIMULATION OF FLOW FIELD AROUND GROIN LIKE STRUCTURE	41
5.1 INTRODUCTION	41
5.2 NUMERICAL TEST	41
5.2.1. Flow domain and hydraulic parameter	41
5.2.2 Computational Scheme	43
5.3 SIMULATED FLOW FIELD	43
5.3.1 Streamline	44
5.4 COMPARISON OF SIMULATION RESULTS WITH PREVIOUS STUDIES	45
5.4.1 Computed velocity profiles	45
5.4.2 Computed bed shear stress	47
5.5 SIMULATED RESULTS FOR DIFFERENT CASE	49
5.5.1 Predicted velocity profiles	49
5.5.2 Predicted bed shear stress profiles	52
5.6 COMPUTED VELOCITY CONTOUR	54

5.7 COMPUTED SHEAR STRESS	56
Chapter 6 LOCAL SCOUR AROUND A GROIN	58
6.1 INTRODUCTION	58
6.2 BED DEFORMATION AROUND SINGLE GROIN	58
6.2.1 Velocity field	59
6.2.2 Bed elevation around the structure.....	64
6.2.3 Flow depth	75
6.3 SIMULATION OF CHANNEL WITH MULTIPLE GROIN	78
6.3.1 Flow Domain and Hydraulic Parameters.....	78
6.3.2 NUMERICAL SIMULATION RESULT.....	79
Chapter 8 CONCLUSION AND RECOMMENDATION.....	87
8.1 Conclusion	87
8.2 Recommendation	88
References.....	89

List of Figure

Figure 1.1: Schematic model of groyne-surrounding flow. (Sarveram et al., 2012)	2
Figure 2.1: Cartesian grid for FD method.....	7
Figure 2.2: Finite difference grid	8
Figure 2.3: Conceptual relationship between consistency, stability and convergence	9
Figure 2.4: An outline of the iRIC Software, its functions and features	12
Figure 3.1: Definition sketch and grid of an open channel with 180° sharply curved bend.....	26
Figure 3.2: Definition sketch and grid of an open channel with 180° mildly curved bend	27
Figure 3.3 : Sketch and preparation of grid of a straight channel by iRIC Software.....	28
Figure 3.4: Sketch and barb installation for 45° angled to the flow direction	28
Figure 3.5: Sketch and barb installation for 90° angled to the flow direction	29
Figure 3.6: Sketch and barb installation for 135° angled to the flow direction	29
Figure 3.7 : Sketch and barb installation for double barb on both side	30
Figure 3.8 : Sketch and grid preparation of a straight channel with three spur dikes.....	30
Figure 3.9: Groin orientation for 90° angled to the flow direction	31
Figure 3.10: Groin orientation for 45° angled to the flow direction	31
Figure 3.11: Groin orientation for 135° angled to the flow direction	32
Figure 4.1: Definition sketch of the flow pattern at the straight portion of the river.....	34
Figure 4.2: Definition sketch of the flow pattern at the bend of the river	34
Figure 4.3: Distribution of water surface elevation for Case II (in m), (a) Experiment by Rozovskii (1961), (b) Simulated by iRIC Nays.....	36
Figure 4.4 : Comparison of simulated water surface profile with experimental results for 180° sharply curved channel	37
Figure 4.5: Comparison of width wise variation of velocity vector at different section of the 180° sharply curved channel (a) Experimental by Rozovskii (1961), (b) Computation by iRIC Nays2DH.....	37
Figure 4.6: Velocity vector super imposed on the surface elevation contour (a) Experimental (b) Simulation by iRIC Nays	38
Figure 4.7: Distribution of depth-averaged velocity 180° mildly curved channel (a) Experiment by De Vriend (1979), (b) Simulation by iRIC Nays2DH	39
Figure 4.8: Comparison of simulated water surface profile	40

Figure 5.1: Computed velocity vector for (a) case-1, (b) case-2, (c) case-3 developed by iRIC Nays2DH.....	42
Figure 5.2: Computed recirculation around groin for (a) case-1, (b) case-2, (c) case-3 developed by iRIC Nays2DH	44
Figure 5.3: Streamline around a groin for (a) case-1, (b) case-2 and (c) case-3 developed by iRIC Nays2DH.....	44
Figure 5.4 : Comparison of resultant velocity profiles (W) with the available previous studies for 90° groin (case 1)	47
Figure 5.5: Comparison of bed shear stress profiles (τ) of predicted results with the available previous studies.....	49
Figure 5.6: Comparison between resultant velocity profiles (W) of present studies for case-1, case-2 & case-3 along lateral distance (a) $y/l=1$, (b) $y/l=1.5$, (c) $y/l=2$,(d) $y/l=3$, (e) $y/l=4$;	52
Figure 5.7 : Comparison between computed bed shear stress (τ) of the proposed model for case 1, case 2, and case 3 along lateral distance, $y/l = 1, 1.5, 2, 3$, and 4.....	54
Figure 5.8 : Velocity contoured around a groin for (a) case -1 (b) case-2, and case 3 at the end of simulation by iRIC Nays2DH.....	55
Figure 5.9: Bed shear stress contour around a groin for test (a) case 1 (b) case 2 and (c) case at the end of simulation by iRIC Nays2DH	56
Figure 6.1 : Velocity field simulation result at water surface into the channel without barb after 1 hour simulation (a) by Hossain et. al (2012) (b)present study	60
Figure 6.2 : Velocity field simulation result at water surface into the channel without barb after 5 hours simulation (a) by Hossain et. al (2012) (4) present study.....	61
Figure 6.3 : Velocity field with a barb installed one side of the channel after 1 hour simulation (a)by Hossain et al (2012) (b) present study	62
Figure 6.4: Velocity field with a 45° barb installed at one sidewall of the channel after 5 hour simulaion (a)Hossain <i>et. al.</i> ,2012). (8) present study	62
Figure 6.5 : Velocity field with 90° barb installed at one side of the channel (9) after 1 hour simulation. (10) after 5 hours simulation.....	63
Figure 6.6 : Velocity field with 135° barb installed at one sidewall of the channel (11) after 1 hours simulation (12) after 5 hours simulation	64
Figure 6.7 : Velocity field result with double barb installed at both sides at the channel (13) after 1 hour simulation (a) by Hossain <i>et. al</i> (2016) (b)present study	64
Figure 6.8 : Velocity field result with double barb installed at both sides at the channel (15) computed simulation after 5 hours.....	64
Figure 6.9 : Bed level contour result of the channel without any structure after 1 hour simulation (a)Hossain <i>et. el.</i> , 2012), (b) present study	65

Figure 6. 10 : Bed level contour result of the channel without any structure after 5 hour simulation (a) by Hossain <i>et. al</i> (2012) (b) present study	66
Figure 6.11: Bed level contour result of the channel with a barb installed at sidewall of the channel (a) by Hossain <i>et. al</i> (2012), (b) present study	66
Figure 6.12 : Bed level contour result of the channel with a 90° barb installed at one sidewall of the channel after 5 hour simulation	67
Figure 6.13 : Bed level contour result of the channel with a 90° barb installed at one sidewall of the channel after 5 hour simulation	67
Figure 6.14: Bed level contour result of the channel with a 135° barb installed at one sidewall of the channel (a) after 1 hour simulation, (b): after 5 hour simulation).....	68
Figure 6.15: Bed level contour line after installed barb both side of the channel top: after 1 hour simulation (a) by Hossain <i>et. al.</i> , 2016), (b) present study.....	68
Figure 6.16: Evolution of bed profile & Comparison before installing barb (a) after 1 hour (b) after 5 hours.....	69
Figure 6.17: Evolution of bed profile & Comparison (C) after 1 hour with 45° barb (d) after 5 hours with 45° barb.....	70
Figure 6.18: Evolution of bed profile (e) & (f) represents bed elevation with 90° barb after 1 hour and 5 hours.....	71
Figure 6.19 : Evolution of bed profile & comparison (g) & (h) represent bed elevation with 135° after 1 hour and 5 hours, respectively	72
Figure 6.20 : Evaluation of bed profile and comparison of double at both side bed evaluation (i) after 1 hour	73
Figure 6.21: Evaluation of bed profile and comparison of double barb at both sides & bed elevation of double barb (j) after 5 hours.....	73
Figure 6.22 : Comparison of 45°, 90° and 135° barbs (k) after 1 hour.....	74
Figure 6.23 : Comparison of 45° , 90° and 135° barbs after 5 hour	74
Figure 6.24: Water depth contour result of the channel with 135° barb installed at one sidewall of the channel (a) after 1 hours simulation, (b) after 5 hours simulation).....	75
Figure 6.25: Water depth contour result of the channel with a barb installed at one sidewall of the channel after 5 hours (a) by Hossain <i>et. al.</i> ,(2012) (b) present study	76
Figure 6.26: Water depth contour result of the channel with a 45° barb installed at one sidewall of the channel after 1 hour simulation (a) by Hossain <i>et. al</i> (2012), (b) present study	76
Figure 6.27: Water depth contour result of the channel with a 45° barb installed at one sidewall of the channel after 5 hour simulation (a) by Hossain <i>et. al.</i> ,(2012) (b) present study	77

Figure 6.28: Water depth contour result of the channel with 90° barb installed at one sidewall of the channel (a) after 1 hours simulation, (b) after 5 hours simulation)	77
Figure 6.29: Water depth contour result of the channel with 135° barb installed at one sidewall of the channel (a)after 1 hours simulation, (b) after 5 hours simulation).....	78
Figure 6.30: Bed deformation contour line of case S ₄ C ₁ simulated by iRIC Nays2DH.....	80
Figure 6.31: Bed deformation contour line of test S ₄ C ₂ simulated by iRIC Nays2DH.....	80
Figure 6.32 : Computed velocity vector in case of test S ₄ C ₁ developed by iRIC Nays2DH.....	81
Figure 6.33: Computed Velocity vector in case of test S ₄ C ₂ developed by iRIC Nays2DH.....	81
Figure 6.34: Definition sketch for different cross and longitudinal sections,.....	81
Figure 6.35 Bed changes comparison of the E1 results found by iRIC Nays2DH with FLOW-3D and experimental results.....	83
Figure 6.36: Bed changes comparison of the E2 results found by iRIC Nays2DH with FLOW-3D and experimental results.....	85

List of Table

Table 2.1 Model constants	19
Table 3.1 Hydraulic parameters for numerical simulation in series 1	24
Table 3.2 Hydraulic parameters for numerical simulation in series 2	24
Table 3.3 Hydraulic parameter for numerical simulation in series 3.....	25
Table 3.4: Hydraulic parameters for numerical simulation in series 4	25
Table 6.3: Comparison of the scouring amount in iRIC Nays2DH results with Flow-3D (pourshahbaz et al., 2017) and experimental results (karami et al., 2014)	85

List of Symbols

ρ	Density
u	Velocity in the x direction
v	Velocity in the y direction
w	Velocity in z direction
ΔA	Surface area
ΣF_x	Sum of the external forces on the control volume
t	Time
Δt	Time step
h	Water depth
g	Gravitational acceleration
H	Water depth
τ_x	Riverbed shearing force in the x direction
τ_y	Riverbed shearing force in the y direction
F_x	Resistance by vegetation in the x direction
F_y	Resistance by vegetation in the y direction
C_f	Riverbed shear coefficient.
ν_t	Eddy viscosity coefficient.
C_D	Drag coefficient of vegetation.
a_s	Area of interception by vegetation per unit volume.
θ	Represents the angle formed by the x axis and the ζ axis (or the y axis and the η axis).
ν_t	Eddy viscosity coefficient
l	Length
α	Proportional constant
k	Karman coefficient
C_μ	Model constant

$C1\varepsilon, C2\varepsilon, \sigma_k$ and $\sigma\varepsilon$	K- ε model constants
C_f	Coefficient of riverbed shearing force
n	Manning's roughness parameter
k_s	Relative roughness height
d	Sediment diameter
g	Gravitational acceleration.
C_d	Drag coefficient of vegetation
α_s	Vegetation per unit volume
n_s	Number of vegetation
D_s	Average diameter of trunks
S_s	Sampling grid width.
L	Length of the straight portion
Q_0	Upstream discharge
h_0	Mean depth
S	Bottom slope
n	Manning's coefficient
V_r	Velocity ratio
u_0	Mean velocity

Chapter 1

INTERODUCTION

1.1 GENERAL

In the field of hydraulic engineering and river engineering the most commonly used structures are the groins, spur dykes and barbs. These hydraulic structures have been constructed in river bank in order to deflect the flowing water away from vulnerable zone. For the purpose of river training, construction of such obstacles against water flow causes significant change in flow patterns, sediment transport and bed topography. The main purpose of built up of such obstacles on natural river bank is to divert the direction of water flow so that bank erosion can be eliminated. The shape of obstacle is similar to a trapezoidal structure with inclined sides and a wide sloped crest. This obstacle behaves as a partially submerged structure (weir) when flow is low and fully submerged when bankfull flow conditions are present. When pointed upstream, the submerged weir section forces the water flowing over the structure into a hydraulic jump (Fox, 2002). The flow separation induced by the hydraulic jump promotes the formation of eddies and sediment deposition on the leeward side of the barb (Lloyd and Stansby, 1997). Generally, barbs are used to protect banks for gentle (wide radius) meanders, or relatively straight banks. The primary function of barbs is to deflect the strong main flow away from critical zones towards the channel centre and therefore, prevent erosion of banks (Hansen and Winter, 1996). The approaches to protect stream banks from erosion during periods of high flows including various bio-technical type channel revetments (Schiechl and Stern, 1997) and groin like structure including bend-way weirs (Davinroy, 1990, 1994) and barbs (USDA, 2001). Barbs have been used by the Natural Resources conservation Service (NRCS) of US department of agriculture, in Oregon for river and stream bank protection since the late 1980. According to Chow (1959), barbs are a trapezoidal shaped rock structure, which extends into the main flow of the river.

Many experimental and numerical researches have been done in order to examine flow pattern and scouring around groins (Rajaratnam and Nwachukwu, 1983). Those studies were carried out in different conditions in terms of groyne length, groyne installation angle towards the approaching flow, permeable or impermeable states, submerged and non-submerged states and number of groins, etc. (Yeo et al., 2005). Due to the variety of groins flow separation and recirculating length would be greatly different which is a challenge to the applications of numerical models (Quanhong and Pengzhi, 2007). The groin which is located at the river main flow with perpendicular orientation, causes narrowing and deviation of the flow and this in turn gives a complex three dimensional form to flow around a groin (Tingsanchali and Maheswaran, 1990). As local scouring, sediment transport and settlement around groin require clarifying the two-dimensional flow pattern, it is necessary to consider the flow pattern around a groin, which is important and necessary to conduct experimental examinations (Jamieson et al., 2013). However, for a full understanding of this flow pattern, one has to use numerical techniques.

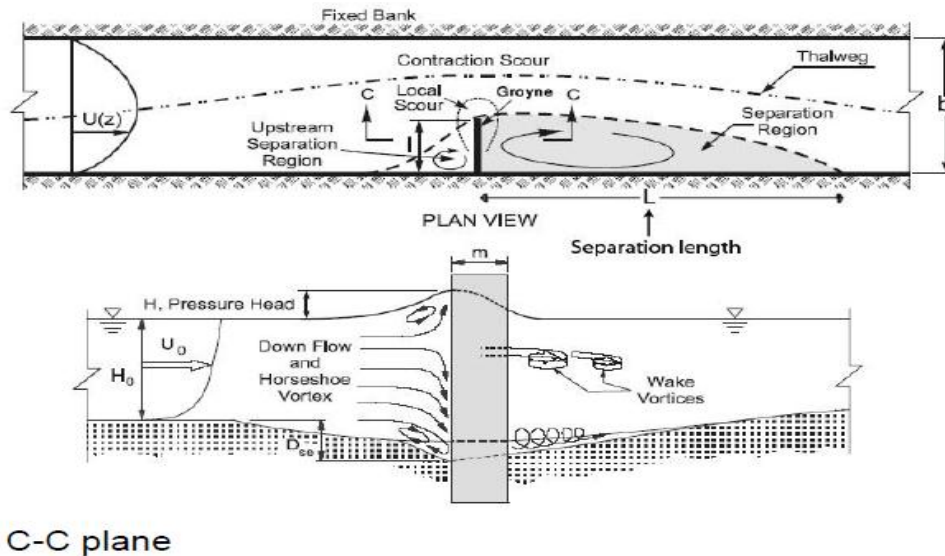


Figure 1.1: Schematic model of groyne-surrounding flow. (Sarveram et al., 2012)

In the flow field with groyne or spur dikes, the flow is separated at upstream of spur dikes and went to levees and created vortexes move to the downstream which finally causes local deposition surface scouring around the structure. In the usage of spur dikes for any purposes, maximum scour depth and scour around spur dikes are so important as can be seen in many researches such as: Ahmad (1951,1953), Garde et al (1961), Gill (1972), Richardson et al (1975), Rajaratnam et al (1983), Shields et al (1995), Kuhnle et al (1999), Kothyari et al (2001), Barbhuiya et al (2004), Kang et al (2011). These structures are mainly built in groups and the flow characteristic would vary in peak and between spur dikes. Researchers such as Chang et al (2013) and Karami et al (2014) investigated the scour depth in groups of spur dikes. Due to the greater interaction between flow and sediment and revealing turbulent flow in group of spur dikes, exact scour depth forecasting needs consideration of flow turbulence in scouring hole Mendoza (1993).

Most of the natural flow are three dimensional for example, in case of meandering channel, the flow passing through the bend is obviously of a three-dimensional (3D) nature because of the generation of secondary current due to the centrifugal force. When a flow in an open channel passes an obstacle (such as groin), the deviation of flow causes the generation of secondary current and flow become highly 3D. Therefore, a 3D hydrodynamic model is necessary to accurately simulate the flows in a meandering channel. However, dealing with the practical engineering problems, such as alluvial geomorphic process, it is not computationally efficient to use 3D models. In such problems, a two-dimensional (2D) model is generally used. To predict the applicability of iRIC software, the model is also applied for sharp 180° and 180° mildly curved bend to simulate the flow field.

In this study, several case studies for open channel flow are simulated after installing the groins with 45° , 90° and 130° angled with the river bank. In addition to the flow field, the local scour around single and multiple groins are also studied.

1.2 OBJECTIVE OF THE STUDY

The main objective of this study is to develop numerical model using iRIC NAYS2D (a computational flow model for multi-dimensional river flow and river bed variation analysis solver package) and to examine the flow and sediment transport behavior in open channel with different topographic configuration and obstacles. The specific objective of this study are outlined as below:

- To simulate two-dimensional open channel flows with 180° sharply curved and mildly curve channel to examine the performance of the software in determining the flow field with strong secondary current.
- To simulate the flow field around a groin with different orientation and flow conditions.
- To simulate the local scour around single and multiple groin fields/stream barbs.

1.3 ORGANIZATION OF THIS REPORT

This thesis is divided into seven chapters. In Chapter 1, the introduction is mentioned. In Chapter 2, Review of literature and detail descriptions of basic equations used for simulation are given. The simulation technique is illustrated in Chapter 3. In Chapter 4, Simulation of flow at a bend is discussed, in which the secondary flow behavior in a sharply and mildly bend channel is studied by using iRIC Nays2DH. In Chapter 5 discussed about simulation of flow field around groin like structure where performance of 45° , 90° and 135° angled groin on the flow direction of an open channel is studied. In Chapter 6, the detail of sediment transport around groin is mentioned, where scour and deposition phenomena is studied in the presence of different angle barb on the flow of a channel. Besides, multiple spur dikes performances are studied in this chapter. In addition, the Chapter 7 contains the conclusion of the present study and recommendations for further study.

Chapter 2

LITERATURE REVIEW

2.1 INTRODUCTION

In this chapter, the available previous studies on experimental and numerical results are reported on groin/stream barb/spur dikes. Besides, some basic equation and concept of iRIC Nays2DH software are illustrated

2.2 REVIEW ON PREVIOUS STUDIES

Kim and Choi (2003) conducted an experiment on numerical simulations of open-channel flows in a bend using the finite element method. They used the 2D numerical algorithm for this simulation. The proposed model was applied to 180° bend experimented by Rozovskii (1961). The simulated results compare favorably to measured data. Then, the model was used to simulate flows in a 7.7 km curved reach in the Han River, Seoul, Korea. They also investigate the impact of planting vegetation on each side of floodplain.

Hsieh and Yang (2003) studied the suitability of 2D models for bend flow simulation by using both a conventional model and a bend-flow model. Analysis of the simulation results indicated that the maximum relative difference in longitudinal velocity is mainly related to the relative strength of the secondary current and the relative length of the channel. Empirical relations connecting the maximum relative difference in longitudinal velocities, the relative strength of the secondary current, and the relative length of the channel, were all proposed to be used as a guideline for model users.

Hossain et al. (2012) applied a numerical model on a rectangular straight channel which is 13.3m long and 0.8m wide. The barb structure is installed as an obstacle at 45°, 90° and 135° on the upstream portion of river channel. The length of the barb is 24cm, one third of the cross-section. The numerical simulations have been done considering sediment transport. Barbs have been used by Natural Resources conservation Service (NRCS) of US department of agriculture, in origin for river and stream bank protection since the late 1980. The Washington State Department of Transportation (WSDOT) has employed barbs for bank protection along highways or river crossing and /or to improve aquatic conditions, especially in shallow gravel bed streams (Papanicolaou et al. 2004). There are various researches have been done for flows around hydraulic structures like spur dikes, barbs, groins, submerged vanes etc, the majority of the investigations have treated flow around these structures and prevent erosion of the bank. Kothyari and Raju (2001) reported that, the primary focus of previous investigations, such as, Gill (1972), Grade et al. (1961) and Ahmad (1953), on the study of scour at abutments and spur dikes was to predict an equilibrium or maximum design scour depth. Barbs induced energy re-distribution away from the outer bank towards the center of the channel results in scour near the ends of the barbs and realignment of the thalweg. Field

observation and laboratory result showed by Johnson, et. al. (2001), Matsuura and Townsend (2004), Kuhnle et. Al.(2002) that, the scour depth occurs at the barbs end and immediately downstream of the structure.

The research in flow field carried out by Francis et al. (1968) was considering separation zone for various types of groynes in a rectangular flume, but they did not measure the flow velocities. Researches done by Rajaratnam and Nwachukwu (1983) contain velocity measurements in the flow field in the presence of groin. Ettema and Muste (2004) examined the effect of groyne length on downstream separation region by considering the effect of scale. Researches by Yeo et al. (2005) also deal with an experimental examination of the downstream separation region of a groin under various groyne lengths, various installation angles and various degrees of groyne permeability (Zhanfeng and Xiaofeng, 2006).

Tingsanchali and Maheswaran (1990) used a two-dimensional depth-averaged model, incorporating a correction factor used in the $k-\epsilon$ model and introducing a three-dimensional correction factor to improve the computed bottom stresses. Molls et al. (1995) also developed a general mathematic model to solve the unsteady two-dimensional depth averaged equations by combining it with a constant eddy viscosity turbulent model (Ettema and Muste, 2004). A great deal of research has been carried out in recent years, especially by Chinese researchers such as Zhanfeng and Xiaofeng (2006), Quanhong and Pengzhi (2007) and Tang and Ding (2007). They studied the model and scouring around groyne by using various models of Turbulence under different conditions of flow and groyne dimension.

2.3 GENERALIZED SIMULATION PROCEDURE

2.3.1 Simulation and modeling

Simulation of a system is used for understanding the physics of the process of the system in time and space. For example in water resources system: effects of land use and climate changes on the balance, groundwater levels, stream flow variability, water quality, etc.

- In the present context the term `model' refers to simulation model and such a model is a representation of natural or human constructed world.
- This model is simpler than the prototype system and can reproduce some characteristics thereof.
- The simulation model produces series of outputs.

2.3.2 Summary of simulation process

Generally the simulation process contains following steps:

- Conceptualization of process of physical system.

- Transforming the process of physical system by into partial differential equation.
- Transforming the partial differential equation into algebraic equations or numerical equations.
- Development of the solution algorithm of the numerical equations.
- The computed codes are written.
- Finally, the model is validated.

2.3.3 Components of a numerical solution method

A numerical solution method contains following components –

- Mathematical Model.
- Discretization Approach.
- Coordinate and Basis Vector Systems.
- Numerical Grid.
- Finite Approximations.
- Solution Method.
- Convergence Criteria

Discretization Approach and Numerical Grid are two most important components. Here we will explain these.

2.3.4 Discretization approaches

There are three discretization approaches-

- Finite Difference Method
- Finite Volume Method
- Finite Element Method

In the present code that has been used here is Finite Difference Method. So, this method is explained below in brief.

2.3.4.1 Finite Difference Method

It is the easiest method to use for simple geometries. The starting point is the conservation equation in differential form. The solution domain is covered by a grid. At each grid point, the differential equation is approximated by replacing the partial derivatives by approximations in terms of the nodal values of the functions. The result is one algebraic equation per grid node, in which the variable value at that and a certain number of neighbor nodes appear as unknown. Finite Difference method is applied to structured grids. These grids consist of families of grid lines with the property that members of a single family do not cross each other and cross each member of other families only once. The position of any grid point within the domain is uniquely identified by a set of 2D indices.

Taylor series expansion or polynomial fitting is used to obtain approximations to the first and second derivatives of the variables with respect to the coordinates. When necessary, these methods are also used to obtain variable values at locations other than grid nodes (interpolation).

FD method is especially easy to obtain higher order schemes on regular grids. The disadvantage of FD method is that the conservation is not enforced unless special care is taken. Cartesian grid for FD method is shown in Figure 2.1.

The idea behind finite difference approximations is borrowed directly from the definition of a derivative:

$$\left(\frac{\partial \phi}{\partial x}\right)_{xi} = \lim_{\Delta x \rightarrow 0} \frac{\phi(x_i + \Delta x) - \phi(x_i)}{\Delta x}$$

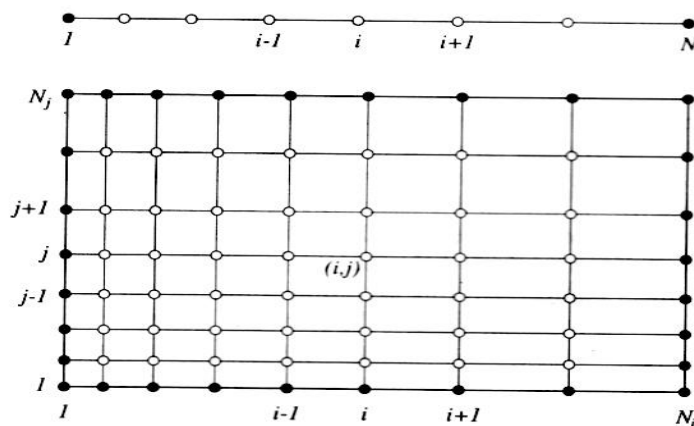


Figure 2.1 : Cartesian grid for FD method

Using Taylor Series Expansions, approximate expressions are obtained for the first and higher derivatives at point x_i in terms of the function values at neighboring points as follows:

$$\left(\frac{\partial \phi}{\partial x}\right)_{xi} = \frac{\phi_{i+1} - \phi_i}{x_{i+1} - x_i} - \frac{x_{i+1} - x_i}{2} \left(\frac{\partial^2 \phi}{\partial x^2}\right)_i - \frac{(x_{i+1} - x_i)^3}{6} \left(\frac{\partial^3 \phi}{\partial x^3}\right)_i + H \quad 2.1$$

Another expression may be obtained by using Taylor Series Expansions at both x_{i-1} and x_{i+1}

$$\left(\frac{\partial \phi}{\partial x}\right)_i = \frac{\phi_{i+1} - \phi_{i-1}}{x_{i+1} - x_{i-1}} - \frac{(x_{i+1} - x_i)^2 - (x_i - x_{i-1})^2}{2(x_{i+1} - x_{i-1})} \left(\frac{\partial^2 \phi}{\partial x^2}\right)_i - \frac{(x_{i+1} - x_i)^3 + (x_i - x_{i-1})^3}{6(x_{i+1} - x_{i-1})} \left(\frac{\partial^3 \phi}{\partial x^3}\right)_i + H \quad 2.2$$

Here, H means “higher order terms”. Higher-order approximations of the first derivative can be obtained by using more points to eliminate more of the truncation error terms. Using ϕ_{i-1} is to obtain an expression for the second derivative at x_i and substituting this expression in equation 2.3, the following second order approximation is obtained:

$$\left(\frac{\partial \phi}{\partial x}\right)_i = \frac{\phi_{i+2}(\Delta x_i)^2 - \phi_{i-2}(\Delta x_{i+2})^2 + \phi_i[(\Delta x_{i+2})^2 - (\Delta x_i)^2]}{\Delta x_{i+2} \Delta x_i (\Delta x_i + \Delta x_{i+2})} - \frac{\Delta x_{i+2} \Delta x_i}{6} \left(\frac{\partial^3 \phi}{\partial x^3}\right)_i + H \quad 2.3$$

2.3.5 Numerical grid

The discrete locations at which the variables are to be calculated are defined by numerical grid which is essentially a discrete representation of the geometric domain. It divides the solution domain into a finite number of sub domains (grid, elements, control volumes etc.)

- Continuous function is replaced by discrete function as grid or elements in a process which is called discretization. Finite difference grid is shown below (Figure 2.2).
- Continuous time is approximated by discrete time steps.

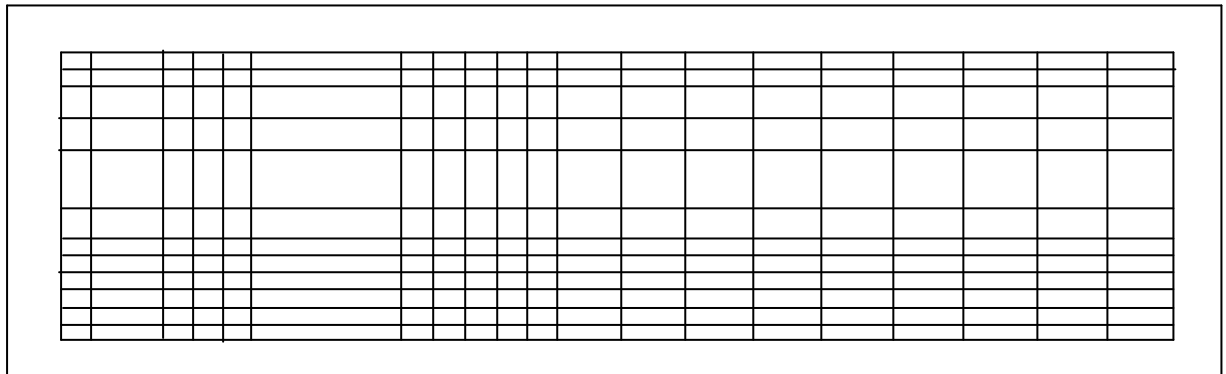


Figure 2.2: Finite difference grid

2.3.6 Properties of numerical solution methods

The solution method should have certain properties. In most cases it is not possible to analyze the solution method. One analyzes the components of the method; if the components do not possess the desired properties, neither will the complete method but the reverse is not necessarily true. Some important properties are given below

- Consistency

- Stability
- Convergence
- Conservation
- Boundedness
- Realizability
- Accuracy

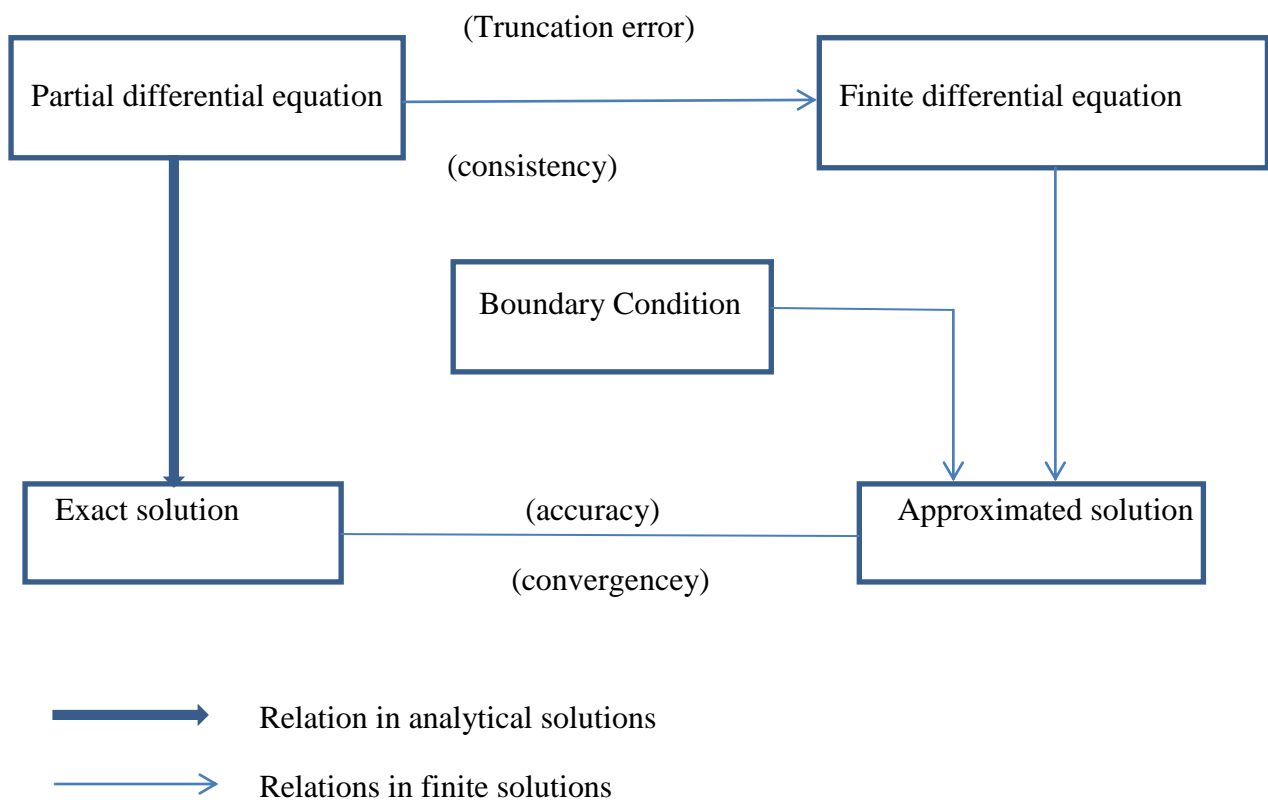


Fig. 2.3: Conceptual relationship between consistency, stability and convergence.

- Consistency

A finite difference scheme is said to be consistent or compatible when the truncation error tends to vanish and the solutions to the finite difference equations approach the solution to the differential equations as the computational mesh is refined (i. e. $\Delta x \rightarrow 0$ and $\Delta t \rightarrow 0$). It is incompatible.

- Stability

The stability of a difference method concerns the amplification errors. These errors may be introduced by inaccurate initial and boundary conditions. Stability is tested by asking if a particular part of the solution is likely to amplify without limit until it destroys the calculation.

The explicit and implicit finite difference schemes are subject to different stability criteria. The following stability criterion can be discerned.

- I. Courant-Friedrichs-Lawy criteria
- II. Von-Neumann criterion

Courant-Friedrichs-Lewy criterion

The condition for stability of an explicit finite difference scheme may be defined as

$$\Delta t \leq \Delta x / C$$

Or $|\sigma| = |c| \Delta t / \Delta x \leq 1$

Where c is the celerity and σ is the Courant number. This is called the Courant Friedrichs-Lewy (CFL) condition or simply the Courant condition and was first established by the three mathematicians in 1928. This is the usual criterion for the stability of explicit finite difference methods.

Von-Neumann criterion

This criterion applies to both explicit and implicit finite difference schemes and states that the amplitude of a particular wave should remain the same or decrease in time, i.e. should not increase with time. This condition is expressed by a complex amplification factor ρ which gives the relationship between the value of a variable at the time level n and that at the advance time level $(n+1)$, e.g.

$$\Phi(j, n+1) = \phi \rho(j, n)$$

The amplitude of the wave is multiplied by $|\rho|$ and there is a phase shift equal to $\arg |\rho|$ and there is a phase shift equal to $\arg(\rho)$

where

$$|\rho| = [(\text{real part of } \rho)^2 + (\text{imaginary part of } \rho)^2]^{1/2}$$

and $\arg(\rho) = \tan^{-1} [\text{imaginary part of } \rho / \text{real part of } \rho]$

Now if the absolute value of the amplification factor is less than unity for any value of the wave length, the amplitude of the numerical solution will decrease and the scheme is numerically stable. But when the amplification factor is greater than unity in absolute value. The amplitude of the numerical solution will be multiplied by a factor greater than one at each time step, causing any perturbation to grow without limit. In such a case the finite

difference scheme will be numerically unstable. Hence a necessary and sufficient condition for stability is that

$$-1 \leq \rho \leq 1$$

$$|\rho| \leq 1$$

Convergency

If the discrete solutions to the governing differential equations approach the exact solutions to the governing equations as the computational mesh is refined, i.e. as $\Delta x \rightarrow 0$ and $\Delta t \rightarrow 0$, for a consistent finite difference scheme, then it is said to be a convergent scheme, then it is said to be a convergent scheme. According to the Lax' equivalence theorem, the necessary and sufficient conditions for a finite difference scheme to be convergent are that the scheme is consistent and stable, i. e.

Consistency + stable = convergency

Accuracy

A finite difference method is said to be accurate if the solution of the finite difference equation we obtain approaches the exact solution of the partial differential equation.

These are three ways of investigating the accuracy of the numerical methods:

1. By determining the truncation error
2. By analyzing the wave propagation and comparing the analytical and the numerical solutions
3. By doing experiments with difference numerical parameters (Δx , Δt etc).

2.3.7 Courant number

The quantity $C = u\Delta t / \Delta x$ is called Courant number. It is the ratio of time step Δt to the characteristics convection time, $u/\Delta x$, the time required for a disturbance to be convected a distance Δx . When courant number is less than 1.

2.4 iRIC SOFTWARE

The International River Interface Cooperative is an informal organization made up of academic faculty and government scientists with the goal of developing, distributing, and providing education for a public-domain software interface for river modeling. Formed in late 2007, the group released the first version of this interface, iRIC, in 2009. The purposes of the activities of this project are creation of opportunities for interaction and provision and exchange of information on issues to utilize knowledge and engineering about rivers to support creation of more beneficial and sustainable river environments among administrative engineers, construction consultant companies, river researchers and students focusing on

development of software for analysis of stream flows, river bed fluctuations and floods. The iRIC software interface includes models for two- and three-dimensional flow, sediment transport, bed evolution, groundwater-surface-water interaction, topographic data processing, and habitat assessment, as well as comprehensive data and model output visualization, mapping, and editing tools. All of the tools within iRIC are specifically designed for use in river reaches and utilize common river data sets. The models are embedded within a single graphical user interface so that many different models can be made available to users without requiring them to learn new pre and post-processing tools. iRIC provides a comprehensive, unified environment in which data that are necessary for river analysis solvers (hereafter: solvers) can be compiled, rivers can be simulated and analytical results can be visualized. The highly flexible iRIC interface allows various solvers to be imported, or you can use one of the iRIC solvers. Upon selecting the solver, iRIC selects functions suitable for the solver and prepares the optimal simulation environment. Because the iRIC functions vary depending on the solver, the method of using the iRIC application depends on the solver.

The iRIC software consists of three functions: preprocessor, postprocessor, and solver (Figure 2.3).

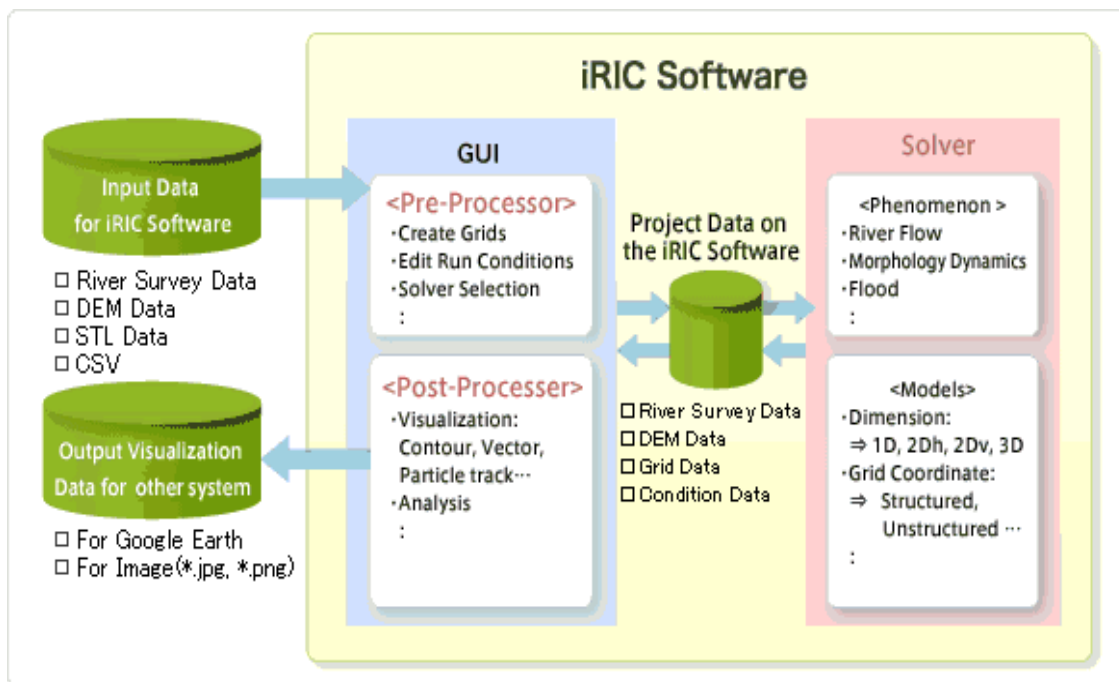


Figure 2.4 : An outline of the iRIC Software, its functions and features.

2.4.1 Features of the flow field calculation model

- As a coordinate system, the general curvilinear coordinate system is adopted, allowing direct consideration of complex boundaries and riverbed shapes.
- Calculations involving the confluence of a main channel and a tributary can be performed.

- For the finite-difference method applied to the advection terms in equations of motion, the user can choose the upwind difference method (primary precision) or the CIP method (This is a high-order finite-difference method. By using a cubic polynomial as an interpolation function, numeric diffusion is reduced, thus enabling high-precision local interpolation).
- For the turbulent field calculation method, the user can select from among [Constant eddy viscosity], [Zero-equation model] and [K- ϵ model].
- Various settings are possible for boundary conditions of the upstream and downstream ends, including periodic boundary conditions, downstream end water surface elevation setting and upstream end velocity setting. This makes it easy to set boundary conditions from limited observation data.
- For setting the initial water surface profile, the user can select from among [Constant slope], [Line], [Uniform flow calculation] and [Non-uniform flow calculation].
- The bottom friction evaluation method is set by using Manning's roughness parameter. This parameter can be set to each computational cell.
- Any obstacle within the calculation target area can be taken into account on a calculation-cell basis. For each calculation cell, a flag can be set to define an obstacle. By this means, river structures such as bridge piers can be easily incorporated in calculation.
- The effect of vegetation for the flow calculation can be introduced as a drag force. The user can set the density of vegetation in each computational.

2.4.2 Features of the sediment transport and riverbed deformation calculation model

- The model allows the user to select between performing flow regime calculation only and performing riverbed deformation calculation along with flow regime calculation.
- For sediment transport, the user can select between bed load only and bed load + suspended load.
- For grain size distribution, the user can select between uniform and non-uniform. When non-uniform grain size is chosen, changes in the grain size distribution in the depth direction during calculation can be stored on a multilayer basis.
- The model can incorporate a slope collapse model. The unrealistic steep slope sometimes can occur in the bed evolution computations, if the bed evolution is simulated by using only Exner equation which expresses the mass conservation of riverbed. In this model, if the angle of riverbed exceeds the critical angle, which is a user parameter, the bed is instantaneously corrected as satisfying the critical angle. By

introducing this model, you can treat the morphologic evolution processes such as bank erosion, which cannot be well captured by using only continuity equation of riverbed.

- Bank erosion takes into account of the tangent of angle of repose. More specifically, when the riverbed slope exceeds the angle of repose as riverbed deformation proceeds, adjustment is made by exchanging sediment with surrounding cells such that the angle of repose is not exceeded. In addition, if the channel widens from bank erosion, calculation grids are automatically moved accordingly.
- Hot Start is provided (continues calculation from where the previous calculation left off, based on the previous calculation results).

2.5 BASIC EQUATIONS

2.5.1 Basic flow equations

2.5.1.1 Basic equations in orthogonal coordinates

The basic equations in an orthogonal coordinate system (x, y) before transformation (mapping) into a general curvilinear coordinate system are as follows:

[Equation of continuity]

$$\frac{\partial h}{\partial t} + \frac{\partial(hu)}{\partial x} + \frac{\partial(hv)}{\partial y} = 0 \quad 2.4$$

[Equations of motion]

$$\frac{\partial(uh)}{\partial t} + \frac{\partial(hu^2)}{\partial x} + \frac{\partial(huv)}{\partial y} = -hg \frac{\partial H}{\partial x} - \frac{\tau_x}{\rho} + D^x + \frac{F_x}{\rho} \quad 2.5$$

$$\frac{\partial(vh)}{\partial t} + \frac{\partial(huv)}{\partial x} + \frac{\partial(hv^2)}{\partial y} = -hg \frac{\partial H}{\partial y} - \frac{\tau_y}{\rho} + D^y + \frac{F_y}{\rho} \quad 2.6$$

in which

$$\frac{\tau_x}{\rho} = C_f u \sqrt{u^2 + v^2} \quad \frac{\tau_y}{\rho} = C_f v \sqrt{u^2 + v^2} \quad 2.7$$

$$D^x = \frac{\partial}{\partial x} \left[v_t \frac{\partial(uh)}{\partial x} \right] + \frac{\partial}{\partial y} \left[v_t \frac{\partial(uh)}{\partial y} \right] \quad 2.8$$

$$D^y = \frac{\partial}{\partial x} \left[v_t \frac{\partial(vh)}{\partial x} \right] + \frac{\partial}{\partial y} \left[v_t \frac{\partial(vh)}{\partial y} \right] \quad 2.9$$

$$\frac{F_x}{\rho} = \frac{1}{2} C_d a_s h u \sqrt{u^2 + v^2} \quad \frac{F_y}{\rho} = \frac{1}{2} C_d a_s h v \sqrt{u^2 + v^2} \quad 2.10$$

where h is water depth, t is time, u is velocity in the x direction, v is velocity in the y direction, g is gravitational acceleration, H is water depth, τ_x is riverbed shearing force in the x direction, τ_y is riverbed shearing force in the y direction, F_x is resistance by vegetation in the x direction, F_y is resistance by vegetation in the y direction, C_f is riverbed shear coefficient, ν_t is eddy viscosity coefficient, C_D is drag coefficient of vegetation and a_s is area of interception by vegetation per unit volume.

2.5.1.2 Transformation into general curvilinear coordinates

Next, basic equations of two-dimensional plane flow at orthogonal coordinates are transformed into general coordinates (ξ, η) . By transforming the equations into general coordinates, it becomes possible to set a calculation mesh of any shape (in keeping with the boundary conditions). The following describes how the equations can be transformed from orthogonal coordinates into general curvilinear coordinates:

$$\frac{\partial}{\partial x} = \frac{\partial \xi}{\partial x} \frac{\partial}{\partial \xi} + \frac{\partial \eta}{\partial x} \frac{\partial}{\partial \eta} \quad 2.11$$

$$\frac{\partial}{\partial y} = \frac{\partial \xi}{\partial y} \frac{\partial}{\partial \xi} + \frac{\partial \eta}{\partial y} \frac{\partial}{\partial \eta} \quad 2.12$$

or,

$$\begin{pmatrix} \frac{\partial}{\partial x} \\ \frac{\partial}{\partial y} \end{pmatrix} = \begin{pmatrix} \xi_x & \eta_x \\ \xi_y & \eta_y \end{pmatrix} \begin{pmatrix} \frac{\partial}{\partial \xi} \\ \frac{\partial}{\partial \eta} \end{pmatrix} \quad 2.13$$

where,

$$\xi_x = \frac{\partial \xi}{\partial x}, \xi_y = \frac{\partial \xi}{\partial y}, \eta_x = \frac{\partial \eta}{\partial x}, \eta_y = \frac{\partial \eta}{\partial y} \quad 2.14$$

likewise,

$$\frac{\partial}{\partial \xi} = \frac{\partial x}{\partial \xi} \frac{\partial}{\partial x} + \frac{\partial y}{\partial \xi} \frac{\partial}{\partial y} \quad 2.15$$

$$\frac{\partial}{\partial \eta} = \frac{\partial x}{\partial \eta} \frac{\partial}{\partial x} + \frac{\partial y}{\partial \eta} \frac{\partial}{\partial y} \quad 2.16$$

or,

$$\begin{pmatrix} \frac{\partial}{\partial \xi} \\ \frac{\partial}{\partial \eta} \end{pmatrix} = \begin{pmatrix} x_\xi & y_\xi \\ x_\eta & y_\eta \end{pmatrix} \begin{pmatrix} \frac{\partial}{\partial x} \\ \frac{\partial}{\partial y} \end{pmatrix} \quad 2.17$$

where,

$$x_\xi = \frac{\partial x}{\partial \xi}, x_\eta = \frac{\partial x}{\partial \eta}, y_\xi = \frac{\partial y}{\partial \xi}, y_\eta = \frac{\partial y}{\partial \eta} \quad 2.18$$

Hence,

$$\begin{pmatrix} \frac{\partial}{\partial \xi} \\ \frac{\partial}{\partial \eta} \end{pmatrix} = \frac{1}{\xi_x \eta_y - \xi_y \eta_x} \begin{pmatrix} \eta_y & -\eta_x \\ -\xi_y & \xi_x \end{pmatrix} \begin{pmatrix} \frac{\partial}{\partial x} \\ \frac{\partial}{\partial y} \end{pmatrix} = \begin{pmatrix} x_\xi & y_\xi \\ x_\eta & y_\eta \end{pmatrix} \begin{pmatrix} \frac{\partial}{\partial x} \\ \frac{\partial}{\partial y} \end{pmatrix} \quad 2.19$$

Here, assuming, $J = \xi_x \eta_y - \xi_y \eta_x$ we obtain,

$$\frac{1}{J} \begin{pmatrix} \eta_y & -\eta_x \\ -\xi_y & \xi_x \end{pmatrix} = \begin{pmatrix} x_\xi & y_\xi \\ x_\eta & y_\eta \end{pmatrix} \quad 2.20$$

Therefore,

$$x_\xi = \frac{1}{J} \eta_y, y_\xi = -\frac{1}{J} \eta_x, x_\eta = -\frac{1}{J} \xi_y, y_\eta = \frac{1}{J} \xi_x \quad 2.21$$

Or,

$$\eta_y = J x_\xi, \eta_x = -J y_\xi, \xi_y = -J x_\eta, \xi_x = J y_\eta \quad 2.22$$

$$J = \xi_x \eta_y - \xi_y \eta_x = J^2 (x_\xi y_\eta - x_\eta y_\xi) \quad 2.23$$

Thus we obtain,

$$J = \frac{1}{x_\xi y_\eta - x_\eta y_\xi} y_\eta \quad 2.24$$

Letting the (ξ, η) components of velocity be (u^ξ, u^η) , then

$$u^\xi = \xi_x u + \xi_y v \quad 2.25$$

$$u^\eta = \eta_x u + \eta_y v \quad 2.26$$

or,

$$\begin{pmatrix} u^\xi \\ u^\eta \end{pmatrix} = \begin{pmatrix} \xi_x & \xi_y \\ \eta_x & \eta_y \end{pmatrix} \begin{pmatrix} u \\ v \end{pmatrix} \quad 2.27$$

$$\begin{pmatrix} u \\ v \end{pmatrix} = \frac{1}{J} \begin{pmatrix} \eta_y & -\xi_y \\ -\eta_x & \xi_x \end{pmatrix} \begin{pmatrix} u^\xi \\ u^\eta \end{pmatrix} \quad 2.28$$

2.5.1.3 Basic equations in a general curvilinear coordinate system

Basic equations as obtained by transforming basic equations in an orthogonal coordinates system (x, y) into a general curvilinear coordinate system are shown below:

[Equation of continuity]

$$\frac{\partial}{\partial t} \left(\frac{h}{J} \right) + \frac{\partial}{\partial \xi} \left(\frac{h u^\xi}{J} \right) + \frac{\partial}{\partial \eta} \left(\frac{h u^\eta}{J} \right) = 0 \quad 2.29$$

[Equations of motion]

$$\begin{aligned} \frac{\partial u^\xi}{\partial \tau} + u^\xi \frac{\partial u^\xi}{\partial \xi} + u^\eta \frac{\partial u^\xi}{\partial \eta} + \alpha_1 u^\xi u^\xi + \alpha_2 u^\xi u^\eta + \alpha_3 u^\eta u^\eta = \\ -g \left[(\xi_x^2 + \xi_y^2) \frac{\partial H}{\partial \xi} + (\xi_x \eta_x + \xi_y \eta_y) \frac{\partial H}{\partial \eta} \right] \\ - \left(C_f + \frac{1}{2} C_D \alpha_s h \right) \frac{u^\xi}{hJ} \sqrt{(\eta_y u^\xi + \xi_y u^\eta)^2 + (-\eta_x u^\xi + \xi_x u^\eta)^2} + D^\xi \end{aligned} \quad 2.30$$

$$\begin{aligned}
& \frac{\partial u^\eta}{\partial t} + u^\xi \frac{\partial u^\eta}{\partial \xi} + u^\eta \frac{\partial u^\eta}{\partial \eta} + \alpha_4 u^\xi u^\xi + \alpha_5 u^\xi u^\eta + \alpha_6 u^\eta u^\eta = \\
& -g \left[(\eta_x \xi_x + \eta_y \xi_y) \frac{\partial H}{\partial \xi} + (\eta_x^2 + \eta_y^2) \frac{\partial H}{\partial \eta} \right] \\
& - \left(C_f + \frac{1}{2} C_D \alpha_s h \right) \frac{u^\eta}{h_j} \sqrt{(\eta_y u^\xi - \xi_y u^\eta)^2 + (-\eta_x u^\xi + \xi_x u^\eta)^2} + D^\eta
\end{aligned} \tag{2.31}$$

where,

$$\alpha_1 = \xi_x \frac{\partial^2 x}{\partial \xi^2} + \xi_y \frac{\partial^2 y}{\partial \xi^2}, \alpha_2 = 2 \left(\xi_x \frac{\partial^2 x}{\partial \xi \partial \eta} + \xi_y \frac{\partial^2 y}{\partial \xi \partial \eta} \right), \alpha_3 = \xi_x \frac{\partial^2 x}{\partial \eta^2} + \xi_y \frac{\partial^2 y}{\partial \eta^2} \tag{2.32}$$

$$\alpha_4 = \eta_x \frac{\partial^2 x}{\partial \xi^2} + \eta_y \frac{\partial^2 y}{\partial \xi^2}, \alpha_5 = 2 \left(\eta_x \frac{\partial^2 x}{\partial \xi \partial \eta} + \eta_y \frac{\partial^2 y}{\partial \xi \partial \eta} \right), \alpha_6 = \eta_x \frac{\partial^2 x}{\partial \eta^2} + \eta_y \frac{\partial^2 y}{\partial \eta^2}$$

$$\begin{aligned}
D^\xi &= \left(\xi_x \frac{\partial}{\partial \xi} + \eta_x \frac{\partial}{\partial \eta} \right) \left[v_t \left(\xi_x \frac{\partial u^\xi}{\partial \xi} + \eta_x \frac{\partial u^\xi}{\partial \eta} \right) \right] \\
&+ \left(\xi_y \frac{\partial}{\partial \xi} + \eta_y \frac{\partial}{\partial \eta} \right) \left[v_t \left(\xi_y \frac{\partial u^\xi}{\partial \xi} + \eta_y \frac{\partial u^\xi}{\partial \eta} \right) \right]
\end{aligned}$$

2.33

$$D^\eta = \left(\xi_x \frac{\partial}{\partial \xi} + \eta_x \frac{\partial}{\partial \eta} \right) \left[v_t \left(\xi_x \frac{\partial u^\eta}{\partial \xi} + \eta_x \frac{\partial u^\eta}{\partial \eta} \right) \right] + \left(\xi_y \frac{\partial}{\partial \xi} + \eta_y \frac{\partial}{\partial \eta} \right) \left[v_t \left(\xi_y \frac{\partial u^\eta}{\partial \xi} + \eta_y \frac{\partial u^\eta}{\partial \eta} \right) \right] \tag{2.34}$$

$$\xi_x = \frac{\partial \xi}{\partial x}, \xi_y = \frac{\partial \xi}{\partial y}, \eta_x = \frac{\partial \eta}{\partial x}, \eta_y = \frac{\partial \eta}{\partial y} \tag{2.35}$$

$$u^\xi = \xi_x u + \xi_y v, u^\eta = \eta_x u + \eta_y v \tag{2.36}$$

$$J = \frac{1}{x_\xi y_\eta - x_\eta y_\xi} \tag{2.37}$$

As for diffusion terms D^ξ and D^η in the motion equation in general coordinates, since developing those terms will make the number of terms huge, they are simplified by assuming the following conditions:

The second-order derivative for the metric coefficient is assumed to be locally zero.

Those terms are locally treated as pseudo-orthogonal coordinates.

As a result, the diffusion terms can be approximated as follows:

$$D^\xi \cong \frac{\partial}{\partial \xi} \left(v_t \eta_r^2 \frac{\partial u^\xi}{\partial \xi} \right) + \frac{\partial}{\partial \eta} \left(v_t \eta_r^2 \frac{\partial u^\xi}{\partial \eta} \right) \tag{2.38}$$

$$D^\eta \cong \frac{\partial}{\partial \xi} \left(v_t \xi_r^2 \frac{\partial u^\eta}{\partial \xi} \right) + \frac{\partial}{\partial \eta} \left(v_t \xi_r^2 \frac{\partial u^\eta}{\partial \eta} \right) \tag{2.39}$$

where ξ_r and η_r are parameters each representing the ratio of the local grid size in general coordinates to the full-scale length of the grid. They are defined as follows:

$$\frac{\Delta \xi}{\Delta \xi} = \xi_r, \frac{\Delta \eta}{\Delta \eta} = \eta_r \tag{2.40}$$

Note that to derive the approximate equations of D^{ζ} and D^{η} above; the following relations are used, based on the assumption of a relationship of local orthogonality.

$$\xi_x^2 + \xi_y^2 = \xi_r^2 (\tilde{\xi}_x^2 + \tilde{\xi}_y^2) = \xi_r^2 (\sin^2 \theta + \cos^2 \theta) = \xi_r^2 \quad 2.41$$

$$\xi_x \eta_x + \xi_y \eta_y = \xi_r \eta_r (\tilde{\xi}_x \tilde{\eta}_x + \tilde{\xi}_y \tilde{\eta}_y) = \xi_r \eta_r (-\cos \theta \sin \theta + \cos \theta \sin \theta) = 0 \quad 2.42$$

$$\eta_x^2 + \eta_y^2 = \eta_r^2 (\tilde{\eta}_x^2 + \tilde{\eta}_y^2) = \eta_r^2 (\sin^2 \theta + \cos^2 \theta) = \eta_r^2 \quad 2.43$$

$$I = \xi_x \eta_y - \xi_y \eta_x = \xi_r \eta_r (\tilde{\xi}_x \tilde{\eta}_y - \tilde{\xi}_y \tilde{\eta}_x) = \xi_r \eta_r (\sin^2 \theta + \cos^2 \theta \sin \theta) = \xi_r \eta_r \quad 2.44$$

where θ represents the angle formed by the x axis and the ζ axis (or the y axis and the η axis).

2.5.2 Turbulent field calculation method

Turbulence means disordered flow that contains eddies of various sizes and structures. Nays2D allows the user to select the turbulent field calculation method from among [Constant eddy viscosity], [Zero-equation model] and [k- ϵ model].

2.5.2.1 Constant eddy viscosity

Eddy viscosity coefficient ν_t is the apparent kinetic viscosity coefficient of a flow in turbulent state. When [Constant eddy viscosity] is selected, calculation is performed with ν_t in equations 3.5 and 3.6 being taken as 0.000001 m²/s.

2.5.2.2 Zero-equation model

Eddy viscosity coefficient ν_t is generally represented as the product of the turbulence representative velocity v_t and the representative length l .

$$\nu_t = v_t l \quad 2.45$$

For a flow field where depth and roughness change only slowly in the transverse direction, assuming that the eddy viscosity coefficient in the horizontal direction and the eddy viscosity coefficient in the vertical direction are on the same order, and considering that the bottom friction velocity and the depth dominantly dictate momentum transport, the eddy viscosity coefficient ν_t is expressed by the following equation.

$$\nu_t = \alpha u_* h \quad 2.46$$

where, α is a proportional constant.

Since α value related to momentum transport in the vertical direction, according to experiments by Fisher and Webel and Schatzmann, is around 0.07, the eddy viscosity coefficient ν_t is expressed using the Karman coefficient k (0.4) as per the following formula:

$$\nu_t = \frac{k}{6} u_* h \quad 2.47$$

Since this modeling does not require any transportation equation for turbulence statistics, it is called the "zero-equation model".

2.5.2.3 K-ε model

The eddy viscosity coefficient ν_t in the standard k-ε model is expressed by the following equation:

$$\nu_t = C_\mu \frac{k^2}{\epsilon} \quad 2.48$$

where C_μ is a model constant. k and ϵ are obtained by the following equations:

$$\frac{\partial k}{\partial t} + u \frac{\partial k}{\partial x} + v \frac{\partial k}{\partial y} = \frac{\partial}{\partial x} \left(\frac{\nu_t}{\sigma_k} \frac{\partial k}{\partial x} \right) + \frac{\partial}{\partial y} \left(\frac{\nu_t}{\sigma_k} \frac{\partial k}{\partial y} \right) + P_h + P_{kv} - \epsilon \quad 2.49$$

$$\frac{\partial \epsilon}{\partial t} + u \frac{\partial \epsilon}{\partial x} + v \frac{\partial \epsilon}{\partial y} = \frac{\partial}{\partial x} \left(\frac{\nu_t}{\sigma_\epsilon} \frac{\partial \epsilon}{\partial x} \right) + \frac{\partial}{\partial y} \left(\frac{\nu_t}{\sigma_\epsilon} \frac{\partial \epsilon}{\partial y} \right) + C_{1\epsilon} \frac{\epsilon}{k} P_h + P_{\epsilon v} - C_{2\epsilon} \frac{\epsilon^2}{k} \quad 2.50$$

Table 2.1 Model constants

C_μ	$C_{1\epsilon}$	$C_{2\epsilon}$	σ_k	σ_ϵ
0.09	1.44	1.92	1.0	1.3

where $C_{1\epsilon}$, $C_{2\epsilon}$, σ_k and σ_ϵ are model constants whose respective values are shown in Table 2.1

Note that P_{kv} and $P_{\epsilon v}$ are calculated with the following equations:

$$P_{kv} = C_k \frac{u_*^3}{h}$$

$$P_{\epsilon v} = C_\epsilon \frac{u_*^4}{h^2}$$

2.5.3 Bottom friction calculation method

In Nays2DH, bottom friction is set using Manning's roughness parameter. For Manning's roughness parameter, the user can define this parameter in each computational cell.

2.5.3.1 Constant value

In Equation 2.4, riverbed shearing forces τ_x and τ_y are expressed by using coefficient of riverbed shearing force C_f . The coefficient of riverbed shearing force C_f is estimated by Manning's roughness parameter n_m as follows:

$$C_f = \frac{gn_m^2}{h^{\frac{1}{3}}} \quad 2.51$$

This Manning's roughness parameter can be estimated from the relative roughness height, k_s , by using the Manning – Strickler equation as follows.

$$n_m = \frac{k_s^{\frac{1}{6}}}{7.66\sqrt{g}} \quad 2.52$$

where k_s is the relative roughness height which is defines as d , d is a sediment diameter and g is the gravitational acceleration.

2.5.4 Method of calculating resistance by vegetation

In Nays2D, resistance exerted by vegetation is set with the drag coefficient of vegetation C_D and the area of interception by vegetation per unit volume α_s . The area of interception by vegetation per unit volume α_s can be set in each computational cell.

The area of interception by vegetation per unit volume α_s is calculated with the following equation proposed by Shimizu et al:

$$\alpha_s = \frac{n_s D_s}{S_s^2} \quad 2.53$$

here n_s is the number of vegetation, D_s is the average diameter of trunks and S_s is the sampling grid width.

Chapter 3

SIMULATION TECHNIQUE

3.1 INTRODUCTION

In this chapter, the simulation techniques for different test cases, details of flow domain and flow parameters are presented. A brief description of 2D numerical model iRIC Nays2DH is given and its operational procedure is explained.

3.2 SOFTWARE USED

In this study, iRIC Nays2DH is used to simulate the flow fields in an open channel with groins. iRIC (International River Interface Cooperative) is a pre- and post-processing software application and framework for computational models of flow and sediment-transport in rivers. The application is a Graphical User Interface (GUI) that allows the model user to build, run, and visualize the results of the system's computational models. The GUI provides tools for building both structured and unstructured grids, defining topography and other boundary conditions on the grid, and defining grid-dependent values such as grain size, vegetation, and obstacles by mapping measured values to the grid or by creating user-defined polygons with attributes of grid dependent value. It combines the functionality of MD_SWMS, developed by the USGS (U.S. Geological Survey) and RIC-Nays, developed by the Foundation of Hokkaido River Disaster Prevention Research Center.

Nays2D is an analytical solver for calculation of unsteady 2D plane flow and riverbed deformation using boundary-fitted coordinates within general curvilinear coordinates. The solver's prototype was initially developed by Professor Yasuyuki Shimizu of Hokkaido University in the 1990s. After many improvements, it was first adopted in 2004 as a calculation solver for incorporation in the RIC-Nays riverbed deformation calculation pre-post software of the Foundation of Hokkaido River Disaster Prevention Research Center (Version 1.0).

Later refined by the inclusion of dynamic memory allocation by Ichiro Kimura of Hokkaido University and outfitted with a bank erosion model by Yasuyuki Shimizu and a HotStart function by Toshiki Iwasaki of Hokkaido University, Nays2DH (Version 2.0) was distributed as one of the solvers included with iRIC in 2010 at the release of iRIC Version 1.0.

Further functional additions included the incorporation of a mixed-diameter multilayer model proposed by Toshiki Iwasaki, and a river confluence model proposed by Takuya Inoue and Michihiro Hamaki of Kaihatsu Koei Co. Ltd. Nays2DH was registered as a calculation solver for iRIC Version 2.0 in March 2011 under the planning and supervision of Kazutake Asahi from the Foundation of Hokkaido River Disaster Prevention Research Center (Version 3.0).

This model has an established reputation for calculation of unsteady flows accompanied with turbulence and laminar flow and it is capable of dynamically showing the realistic motions of unsteady eddies. In addition, its riverbed deformation calculations can reproduce the generation, development and migration of sandbars with high precision. There have been many examples of Nays2D being used on actual rivers for purposes such as assessing the effects of trees and vegetation, making flood calculations, studying the effects of inflowing rivers and simulating bank erosion disasters.

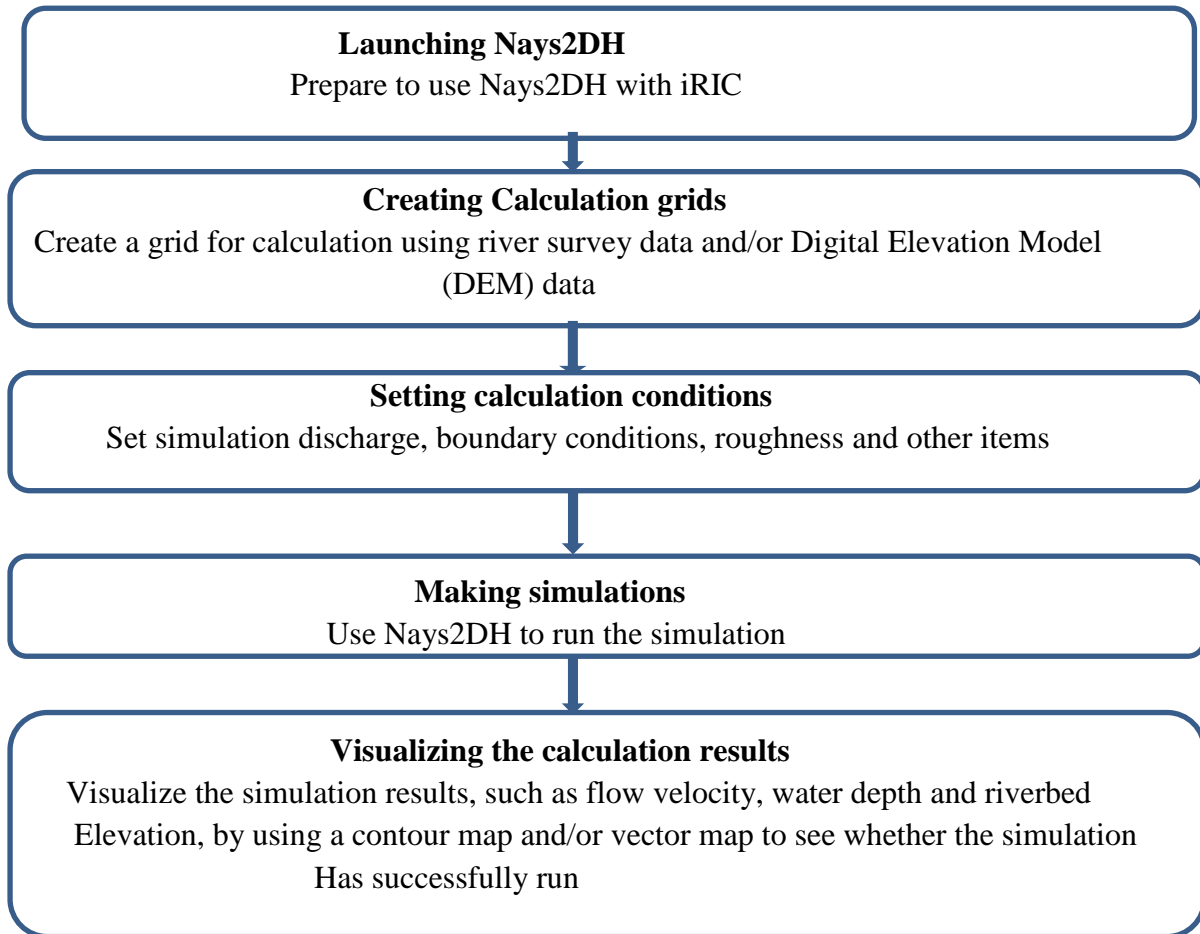
Nays is a model developed at Hokkaido University; the details of the model are described in Shimizu (2002). The title of the model is not an acronym; it is an Ainu word meaning “small river”. There are four primary features of Nays:

- It is two-dimensional (vertically integrated).
- It is fully unsteady.
- It is cast in a general, nonorthogonal coordinate system with variable cell size.
- It includes a much more sophisticated method for treating turbulence that includes both a horizontal large eddy simulation and a suite of turbulence closures.

The non-orthogonal coordinate system allows more precise fitting of the coordinate system to suit arbitrary channel curvature and variable width. More importantly, the more detailed treatment of turbulence and large eddies allows predictions of time-variable behavior even for steady discharges. Nays is currently the most sophisticated model within iRIC in terms of handling advection of momentum and strong local unsteadiness. Nays also includes full sediment-transport capabilities and morphologic change prediction, so the impacts of unsteadiness on bed change can be assessed with this approach. Furthermore, Nays provides a variety of particle-tracking information.

3.4 OPERATIONAL PROCEDURE OF SOFTWARE

The following are the basic procedures for operating Nays2DH with iRIC



3.5 FLOW PARAMETER

The numerical tests consist four series, where each series contains several set of simulation cases.

Series 1 : Simulation of 180° sharp and mildly curved bend.

Series 2 : Simulation of open channel flow with different orientation of groin.

Series 3: Simulation of flow and local scour around a single barb (groin) with different orientations.

Series 4 : Simulation of flow and local scour around a group of three groins.

The hydraulic parameters for 180° bend channel are shown in Table 3.1. The parameters for case of 180 degree sharp bend were taken same as the experiments by Rozovskii (1961). The parameters for case of 180 degree mild bend were taken same as the experiments by De Vriend (1979).

Table 3.1 : Hydraulic parameters for numerical simulation in Series 1 are given below(Case S₁C₁ is the case for sharp bend and S₁C₁ is for mild bend)

Case no.	L (m)		W, m	Q ₀ , m ³ /s	h ₀ , m	Bottom slope, S ₀	Δt, sec	R/B	n	Courant number
	U/S	D/S								
S ₁ C ₁	6	3	0.8	0.0123	0.0600	0	0.005	1.0	0.0102	0.04
S ₂ C ₁	6	6	1.7	0.0671	0.1953	0.016	0.020	3.5	0.0350	0.0149

Δt = Time step, L = Length of the straight portion, Q₀ = Upstream discharge, h₀ = Mean depth, S₀ = Bottom slope, n = Manning's coefficient.

Table 3.2 Hydraulic parameters for numerical study in series 2 are given below(S₂C₁ is for 45° groin, S₂C₂ is for 90° groin and S₂C₃ is for 135° groin)

Case no	Groin Position	L (m)		W (m)	Q ₀ (m ³ /s)	h ₀ (m)	S ₀	Δt (sec)	
		U/S	D/S						
S ₂ C ₁	45°	2	4	0.9	0.0430	0.189	0.001	0.003	0.01
S ₂ C ₂	90°	2	4	0.9	0.0430	0.189	0.001	0.003	0.01
S ₂ C ₃	135°	2	4	0.9	0.0430	0.189	0.001	0.003	0.01

Here, L = Length of the straight channel, W=Width of channel, Q₀=Upstream discharge, h₀ = Water depth at downstream, n = manning's roughness co-efficient.

The parameters for case-S₂C₁ for the flows in an open channel with groin of 45⁰ angled to the direction of flow were taken same as the experiments by Rajaratnam and Nwachukwu (1983) and in Table 3.2. The hydraulic parameters for the 90⁰ and 135⁰ angled groin are the same as the case-S₂C₁.

The hydraulic parameters for the bed evaluation in an open channel with 45° angled barb were taken as same as the numerical model presented by Hossain et al (2012) and shown in Table 3.2. Hydraulic parameter for both 90° and 135° angled barb were taken same as 45° angled barb.

Table 3.3 : Hydraulic parameters for numerical study in series 3 are given bellow

(Case S_3C_1 is for without barb, S_3C_2 is for 45° stream barb, S_3C_3 is for 90° stream barb, S_3C_4 is for 135° stream barb and S_3C_5 is for barb at both sides)

Case no	Groin position	L (m)	B(m)	S (m/m)	B/D	D(m)	Q (m ³ /s)	U m/s	d ₅₀ mm
S_3C_1	No barb	13.3	0.8	0.005	18	0.044	0.028	0.64	0.77
S_3C_2	45°	13.3	0.8	0.005	18	0.044	0.028	0.64	0.77
S_3C_3	90°	13.3	0.8	0.005	18	0.044	0.028	0.64	0.77
S_3C_4	135°	13.3	0.8	0.005	18	0.044	0.028	0.64	0.77
S_3C_5	Double barb	13.3	0.8	0.005	18	0.044	0.028	0.64	0.77

Here, L = length of the channel, B = width of the channel, S = slope of the channel, D = water flow depth at downstream, Q = Discharge of the channel, U = velocity, Fr = Froude number. d₅₀ = sediment size.

The flow parameters for three parallel spur dikes in a straight open channel were taken same as both the experiment and numerical study presented by karami et al (2014) in table 3.4.

Table 3.4 Hydraulic parameter for numerical study in series 4 are given bellow

(Case S_4C_1 is for three spur dikes with discharge 0,035 m³/s and S_4C_2 is for three spur dikes with discharge 0.046 m³/s).

Case no.	L	B	Y	Q	U	Fr	d ₅₀
	m	m	m	m ³ /s	m/s	-	mm
S_4C_1	5	1	0.15	0.035	0.233	0.19	0.91
S_4C_2	5	1	0.15	0.046	0.307	0.25	0.91

Here, L = length of the channel, B = width of the channel, S = slope of the channel, Y = water depth, U = velocity of the channel, Fr = Froude number, d₅₀ = Sediment size.

3.6 COMPUTATIONAL SCHEMES AND FLOW DOMAIN

The governing equations for mean velocities and turbulent flows are discretized with the finite difference method based on full staggered boundary fitted coordinate system. The basic equations are discretized as fully explicit forms and solved successively with the time increment in step by step. It is solved using iterative procedure at each time step. Constant discharge at upstream and constant depth with zero velocity gradients was given as downstream boundary conditions. Finite volume method was used for the solution of the equations. 2D grid, Q, h_e and initial flow conditions were given as input.

3.6.1 Series 1

Figure 3.1 shows the sketch of the flow domain for 180° sharp bend which was performed under the same conditions of the experiments conducted by Rozovskii (1961). Figure 3.2 shows the sketch of the flow domain for 180° mild bend which was performed under the same conditions of the experiments conducted by De Vriend (1979). For the first Case 163 x 25 and for the second Case 126 x 25 grids were used with moveable bed condition.

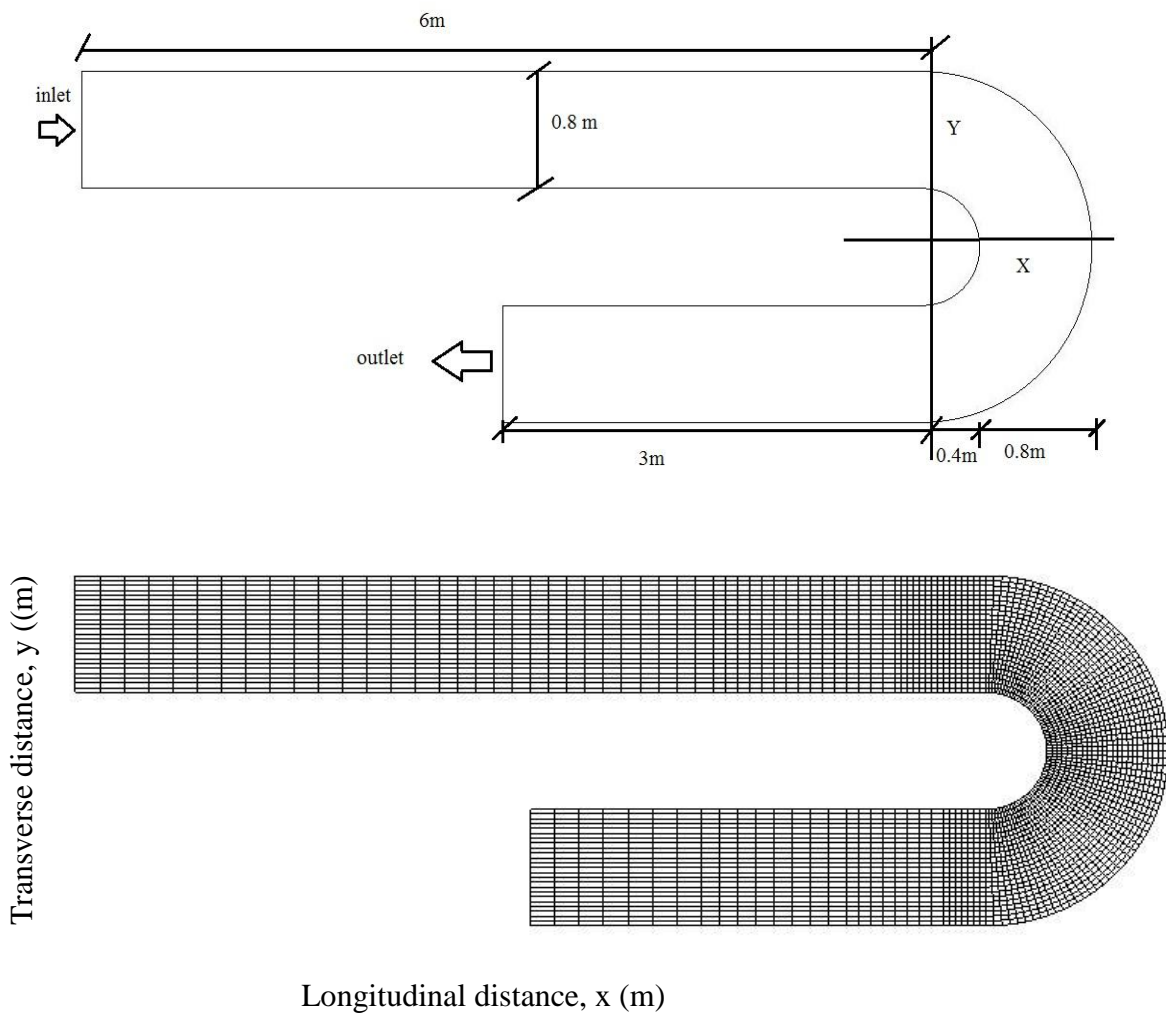


Figure 3.1: Sketch and grid of an open channel with 180° sharply curved bend (Case S₁C1).

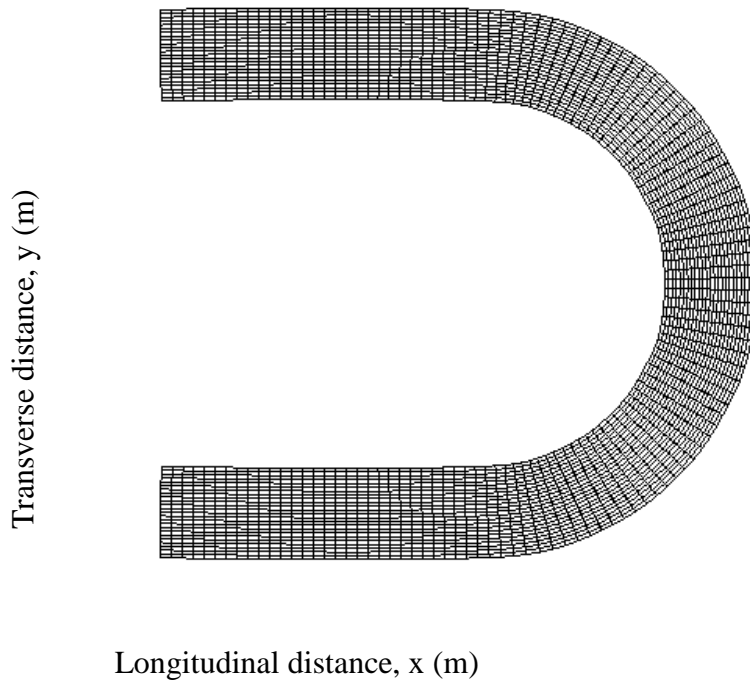
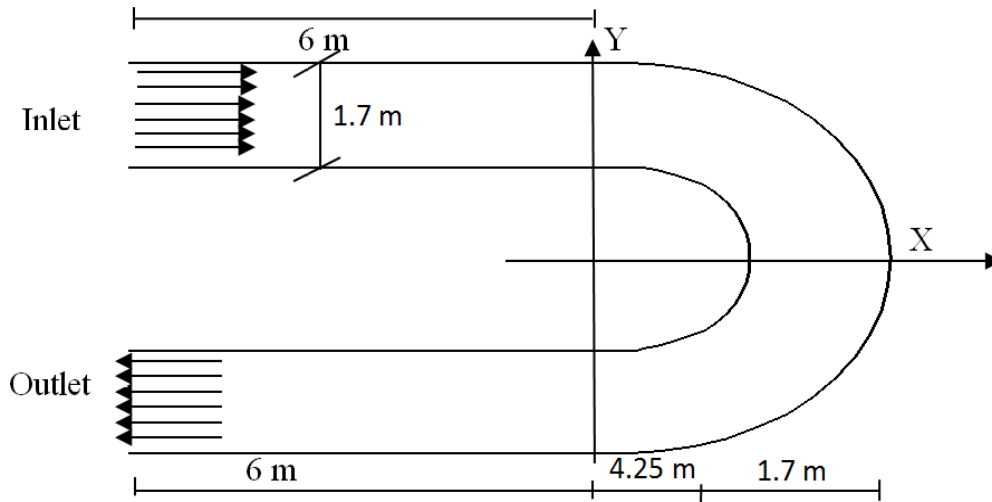


Figure 3.2: Sketch and grid of an open channel with 180° mildly curved bend prepared by iRIC software (Case S₁C₂).

3.6.2 Series 2

Figure 3.3 shows the sketch of the flow domain for flows in an open channel with groin of 90° angled to the direction of flow which was performed under the same conditions of the experiments conducted by Rajaratnam and Nwachukwu (1983). Figure 3.4 and Figure 3.5 show the sketch of the flow domain for 45° and 135° which were performed under the same conditions as case-1. For all these cases 120 x 20 grids were used and the bed of the channel was fixed.

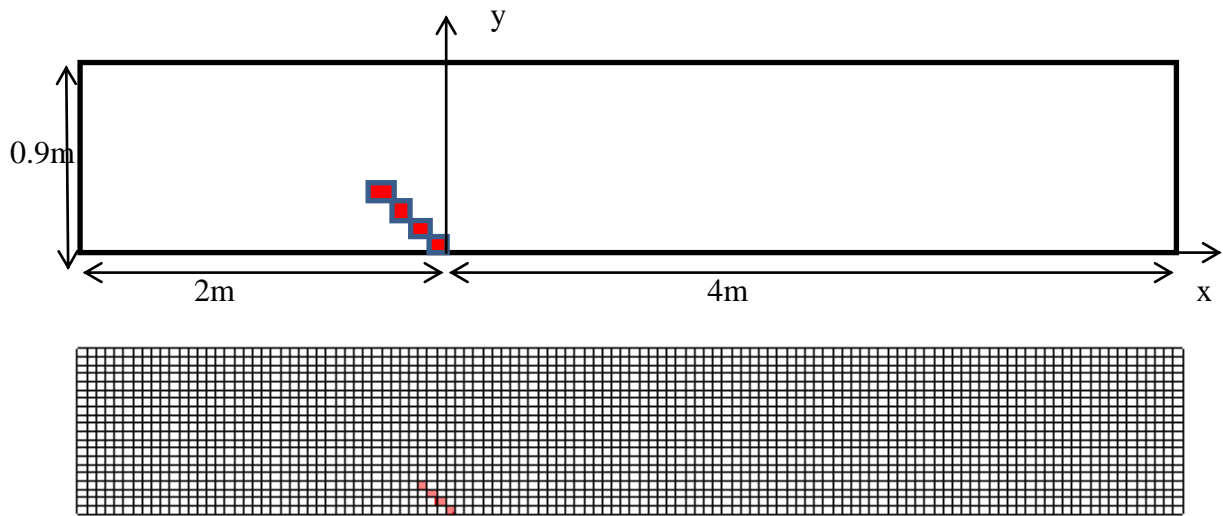


Figure 3.3 : Sketch and groin orientation for 45° angled to the flow direction (Case S₂C1).

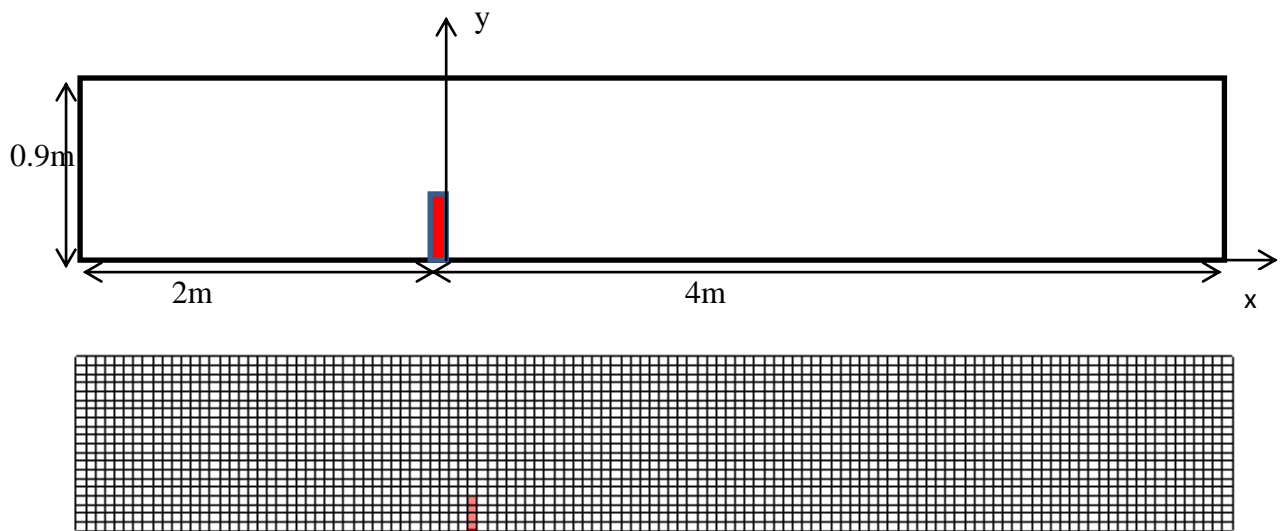


Figure 3.4: Sketch and groin orientation for 90° angled to the flow direction (Case S₂C2).

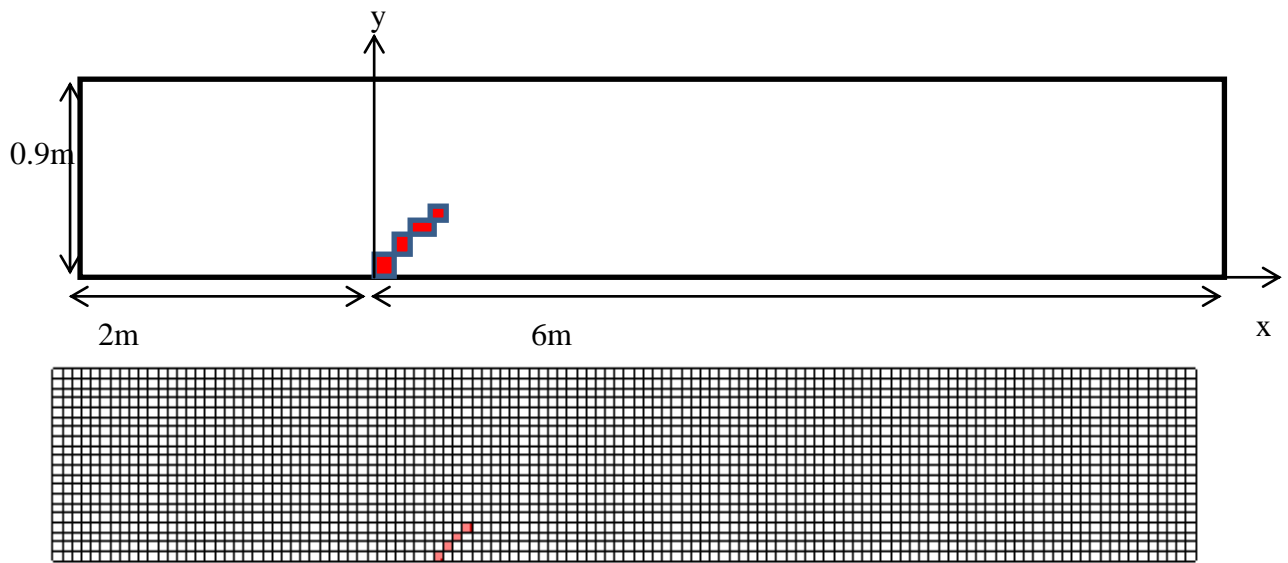


Figure 3.5: Sketch and groin orientation for 135° angled to the flow direction (Case S₂C₃).

3.6.3 Series 3

Figure 3.7 shows the sketch of the flow domain for flows in a straight open channel with groin of 45° angle to the direction of flow which was performed under the same condition conducted by Hossain et al (2012).

Figure 3.8 and Figure 3.9 show the sketch of the flow domain for 90° and 135° which were performed under the same conditions . For all these cases 100 x 10 grids were used and the bed of the channel was moveable.

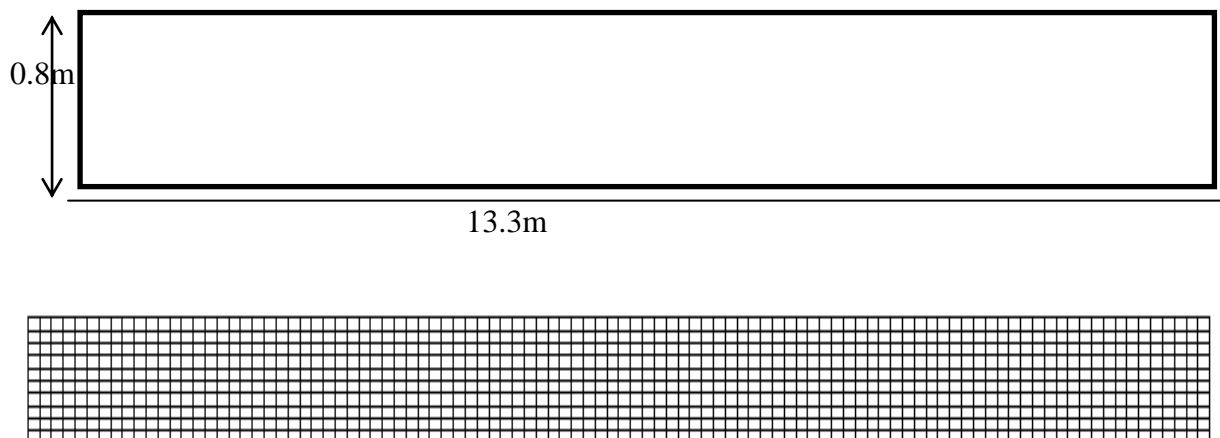


Figure 3.6: Sketch and Preparation of grid of a straight channel by iRIC Software (Case S₃C₁)

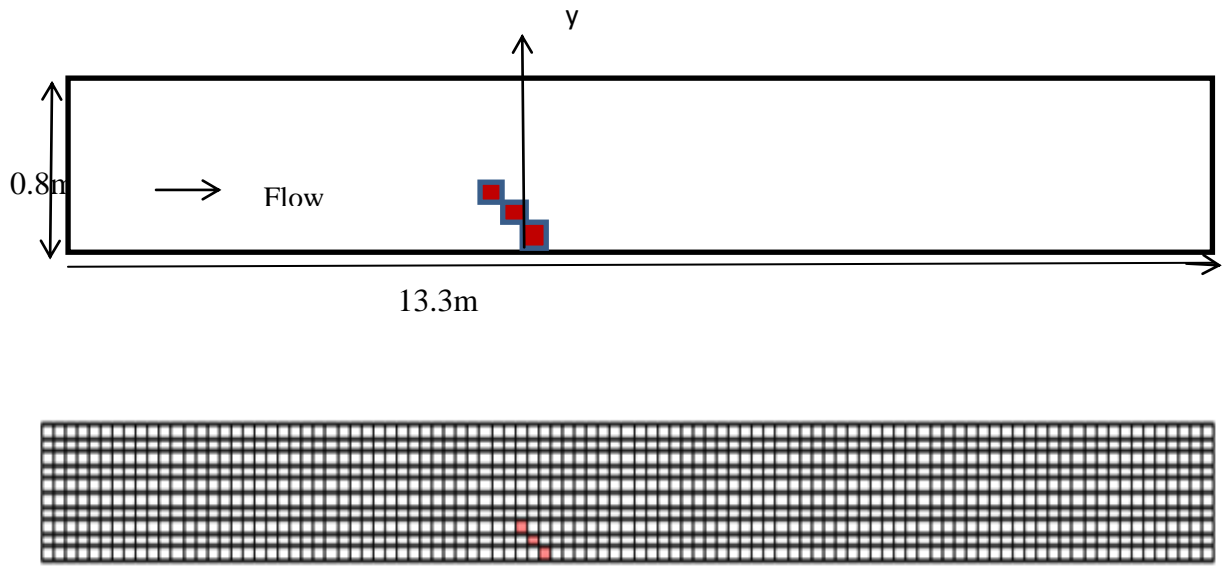


Figure 3.7: Sketch and barb installation for 45° angled to the flow direction prepared by iRIC software (Case S_3C_2).

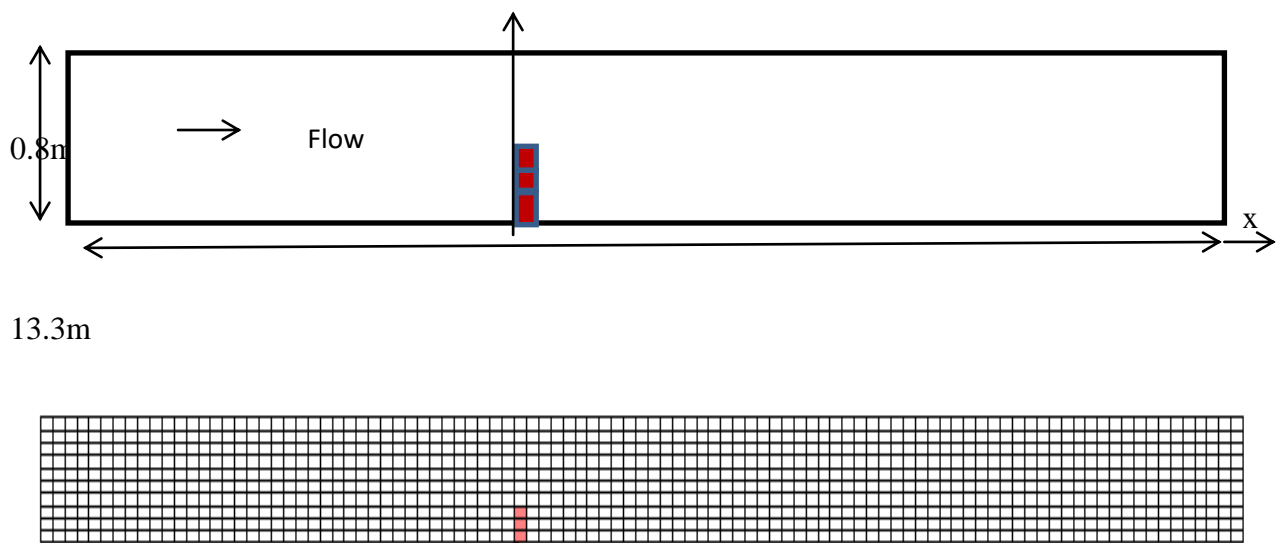


Figure 3.8: Sketch and barb installation for 90° angled to the flow direction prepared by iRIC software (Case S_3C_3).

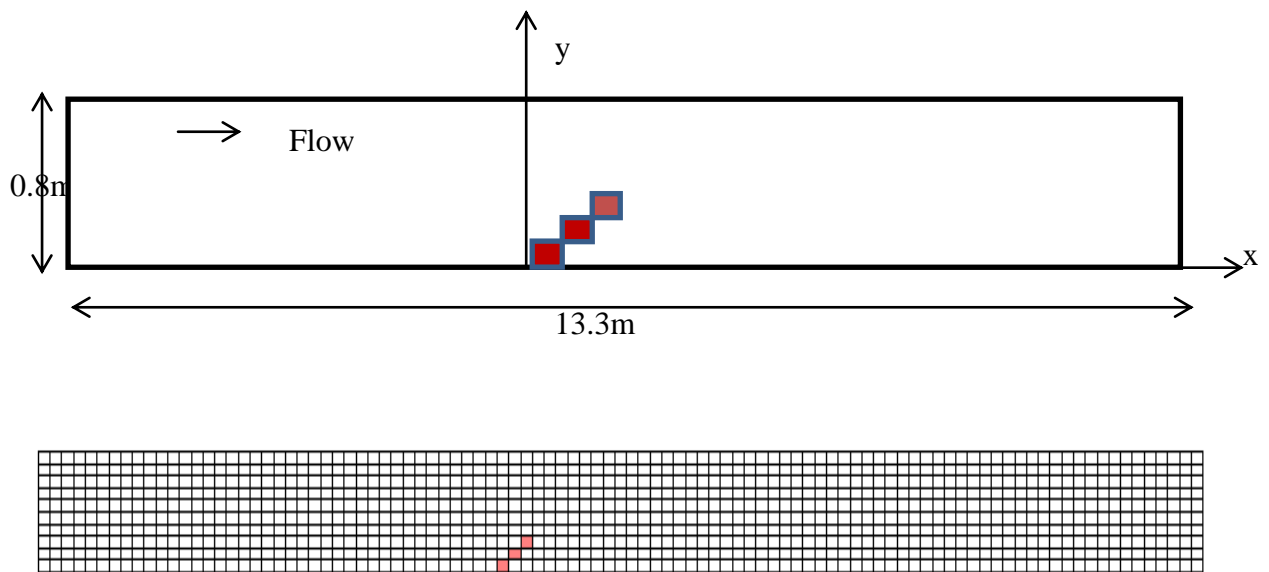


Figure 3.9 : Sketch and barb installation for 135° angled to the flow direction prepared by iRIC software (Case S_3C_4).

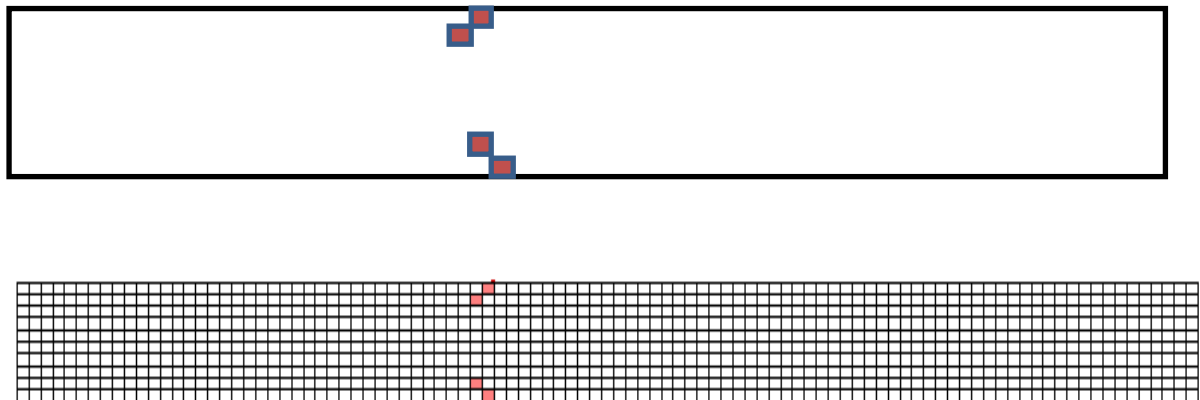


Figure 3.10: Sketch and barb installation for double barb on both side prepared by iRIC software (Case S_3C_4).

3.6.4 Series 4

Figure 3.11 shows the sketch of the flow domain for a straight channel with three perpendicular groin which was based on experimental study presented by karami et al (2014). In this case, 120×26 grid were used.

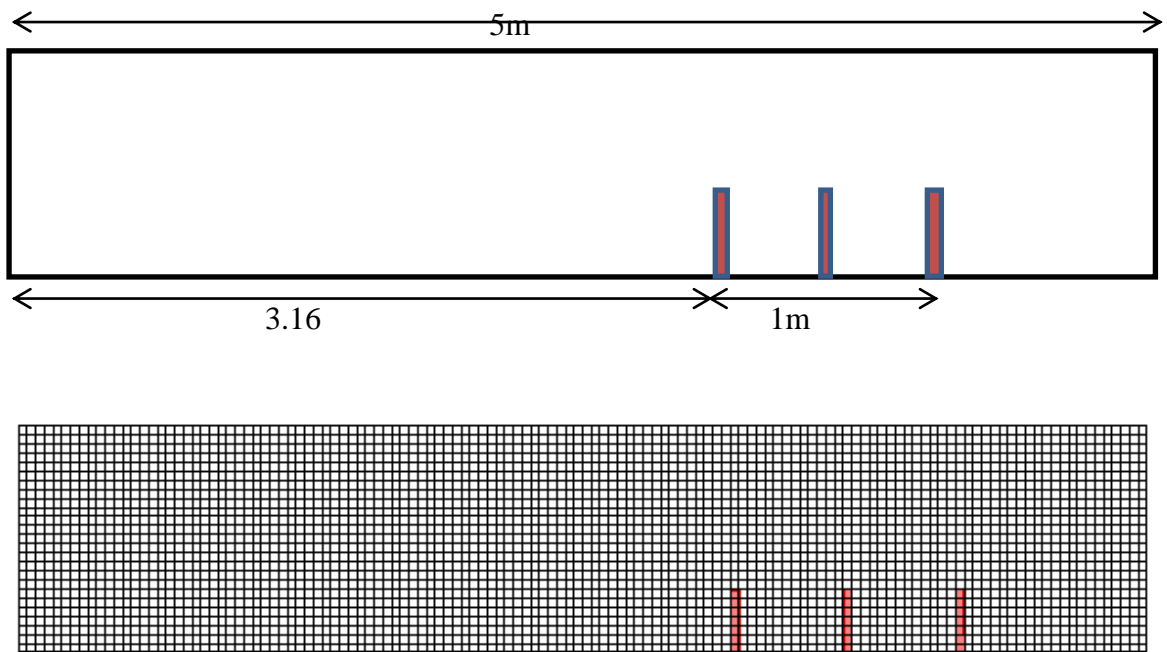


Figure 3.11 Sketch and grid preparation of a straight channel with three spur dikes

Chapter 4

SIMULATION OF FLOW AT A BEND

4.1 INTRODUCTION

2D numerical model, iRIC Nays2DH, is used to simulate a 180° sharply and 180° mildly curve bend to assess the predictability of the model for the flow field having strong secondary current. The numerical simulation has been performed on fixed bed condition and the simulated velocity field and water surface profile are compared with previous experimental result to evaluate the capability of the model.

Natural river are characterized by complex geometrics such as channel expansions and contractions, bends and variable bed and bank variable bed and bank roughness. In the field of river engineering, it is important to understand the flow behavior exits at sharp bends. Because of having river's highly turbulent in nature, it is difficult, time consuming and costly in order to obtain all necessary details by lab experiment and field observation. So, numerical simulation can be better option to get all necessary details within a short time. The computational fluid dynamic (CFD) is branch of fluid dynamics which provides fast, accurate and flexible fluid flow simulation. Computational fluid dynamics is based on Navier-Stokes equation. 3D hydrodynamic model is required in order to accurately simulate the flow in a meandering channels. For this purpose several 3D models have been developed by Wang and Hu (1990), de Vriend (1980) and Shimizu et al (1990) to simulate the flow field in meandering channels. To avoid some practical engineering problems, such as alluvial geomorphic engineering problems, such as alluvial geomorphic processes, to use 3D model is not efficient. Flow passing through meandering channels also has influence of the secondary flow in which there is a transverse circulation introduced by the centrifugal force. Measurement by Rozovskii (1961) and de Vriend (1979,1980, 1981) have shown that the secondary flow near the water surface moves toward the outer bank and that near the bed moves toward the inner bank.

As shown in Figure 4.1, the two-dimensional flow has only two velocity components; they are longitudinal or stream wise and transverse or width wise velocities. Vertical or depth wise velocity component is ignored. At the straight portion, the width-wise variation of flow is very small, and only the stream wise velocity or the longitudinal velocity dominates the flow.

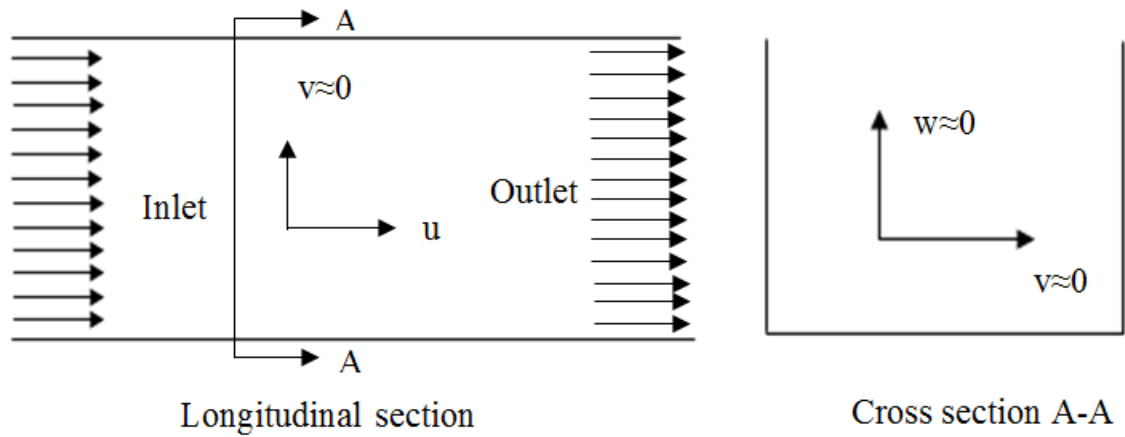


Figure 4.1: Definition sketch of the flow pattern at the straight portion of the river.

At the bend, the flows of water are dominated by both the longitudinal and transverse velocity components as shown in Figure 4.2. Secondary current is generated due to the centrifugal force at the bend when water enters into the bend. Though the water depth is equal for the inner bank and outer bank at the straight portion, it differs from inner bank to outer bank at the bend of the river. This difference in water level results from the transverse slope caused by the centrifugal force. It causes a higher velocity at the inner bank than the outer.

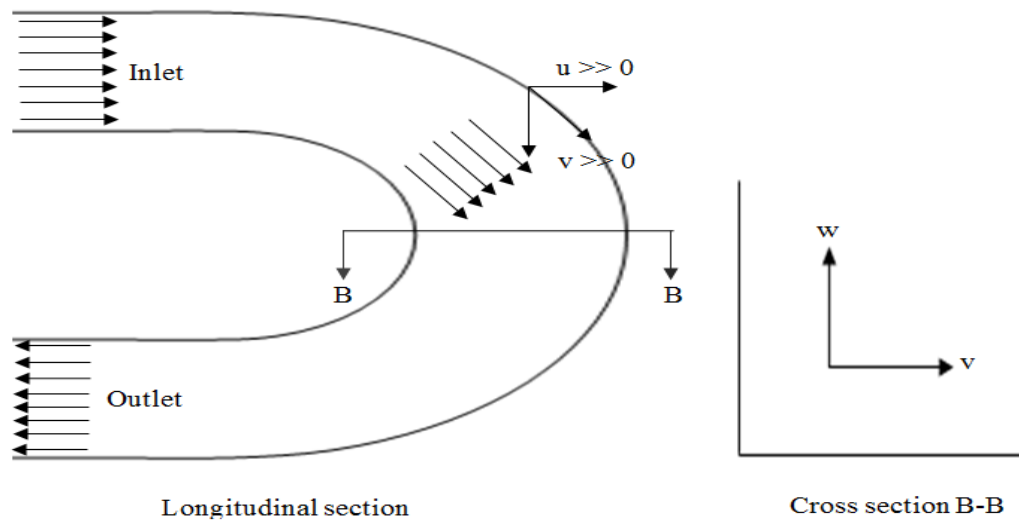


Figure 4.2 : Definition sketch of the flow pattern at the bend of the river.

To simulate meandering channel flow by 2D models, generally the depth-averaged Navier–Stokes equations numerically by using finite element technique and the simplified depth-averaged Navier–Stokes are used. The momentum transfer due to the secondary flow is inadequately accounted for by the depth averaged models and various empirical functions

have to be introduced in these models to approximate the secondary flow. In many practical cases, the effect of secondary flow is not significant when the channels are not curved or the curvature effect is small. This study employed the Cartesian coordinate so that the hydrodynamic model can be easily applied to both meandering and non-meandering channels.

4.2 SIMULATED RESULTS OF 180° SHARPLY CURVED CHANNEL (Case S₁C₁)

The flow domain consists of 0.8 m wide channel having a rectangular cross section. The straight reaches at the upstream has an effective length of about 6.0 m and downstream has an effective length of about 3.0 m. The internal and external radius of curvature is 0.4 m and 1.2 m respectively. The ratio of radius of curvature to channel width is 1.0. The cross section of the channel bend is a 0.8 m wide rectangle, and entire channel bed is horizontal. The channel bottom is made smooth. The discharge at the inlet is 0.0123 m³/s, the averaged mean velocity is 0.265 m/s, and the averaged flow depth is 0.06 m. The computational mesh is 163 x 25 with 163 cross sections in the longitudinal direction and 25 nodes in each cross section. The logarithmic law at the sidewalls was used in the numerical simulation. The simulation reach consists of the U bend and the effective straight reaches at the upstream and downstream. Constant discharge at upstream and constant depth with zero velocity gradients was given as downstream boundary conditions. Sharply curved channel is simulated of Standard Solver type with finite differential method and discretizing the advection terms as upwind scheme by iRIC Nays. iRIC Nays results are compared with experimental results.

Figure 4.3 (a) shows the measured contours of water surface of Rozovskii's (1961) experiment. Figure 4.3 (b) shows the simulated result. It can be seen that the numerical model successively reproduces the higher water surface elevation along the outer bank than the inner bank. So the overall agreement between measured and simulated profiles appears to be quite good.

The longitudinal distribution of water surface along the inner bank and outer bank are compared in Figure 4.4. The horizontal axis in the figure is the dimensionless distance from the entry of the channel bend. From this Figure it is seen that, the water surface elevation at the outer bank is much higher than that in the inner bank throughout the bend. It can be also seen that the computed flow depth is close to the measured data and the agreement between measured and simulated profiles is satisfactory.

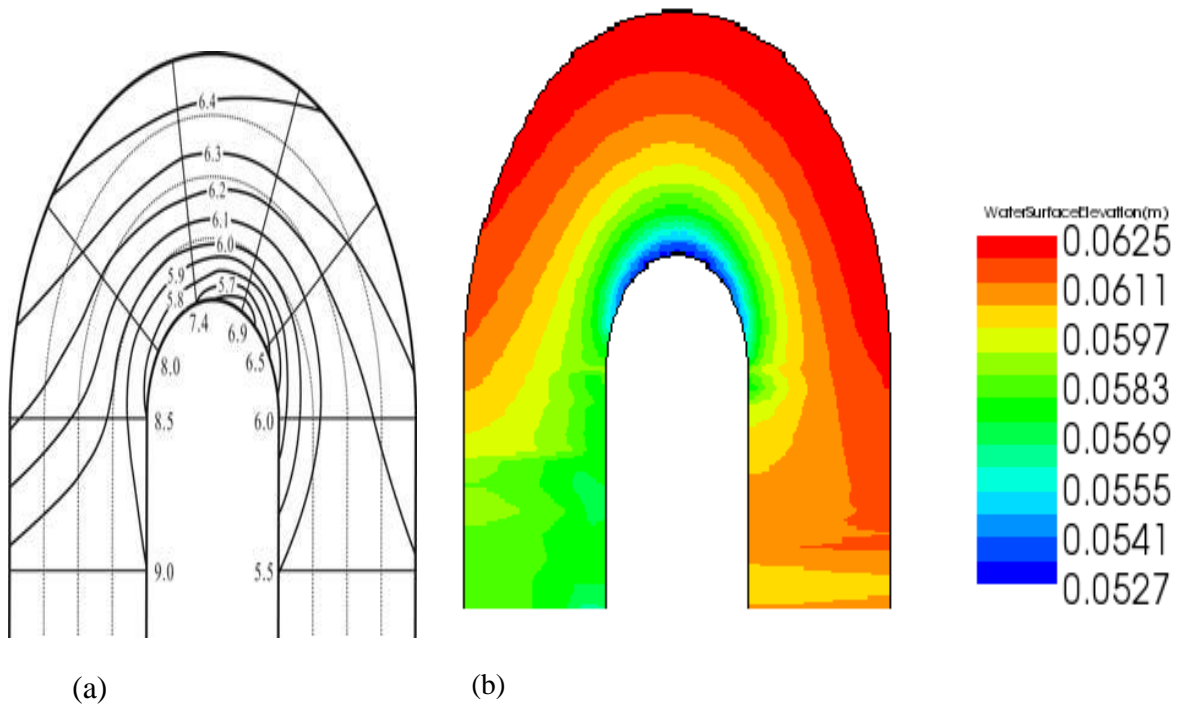


Figure 4.3: Distribution of water surface elevation for Case S₁C₁ (a) Experiment by Rozovskii (1961), (b) Simulated by iRIC Nays.

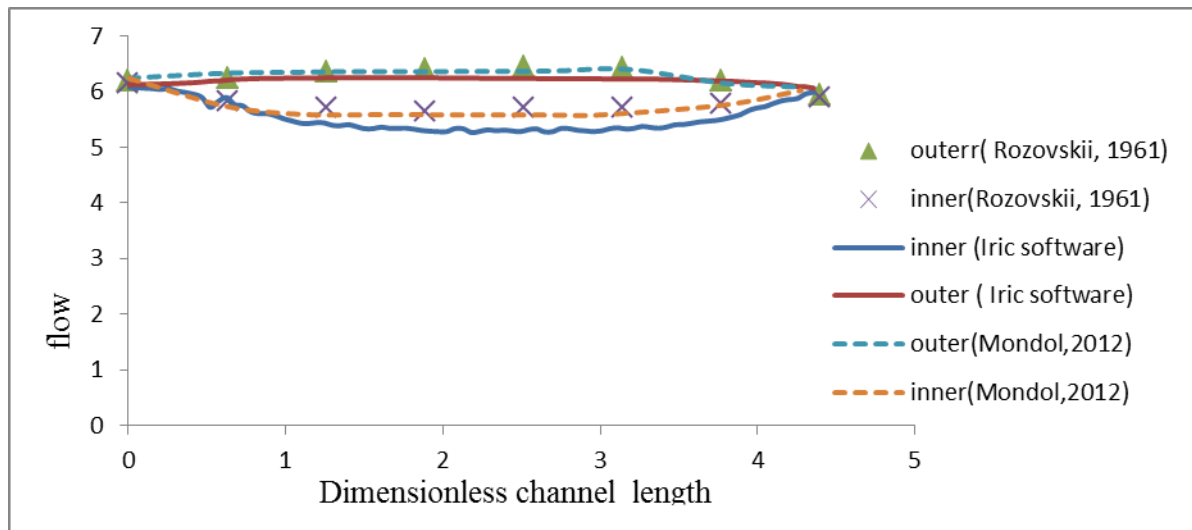


Figure 4.4 : Comparison of simulated water surface profile with experimental results for 180° sharply curved channel.

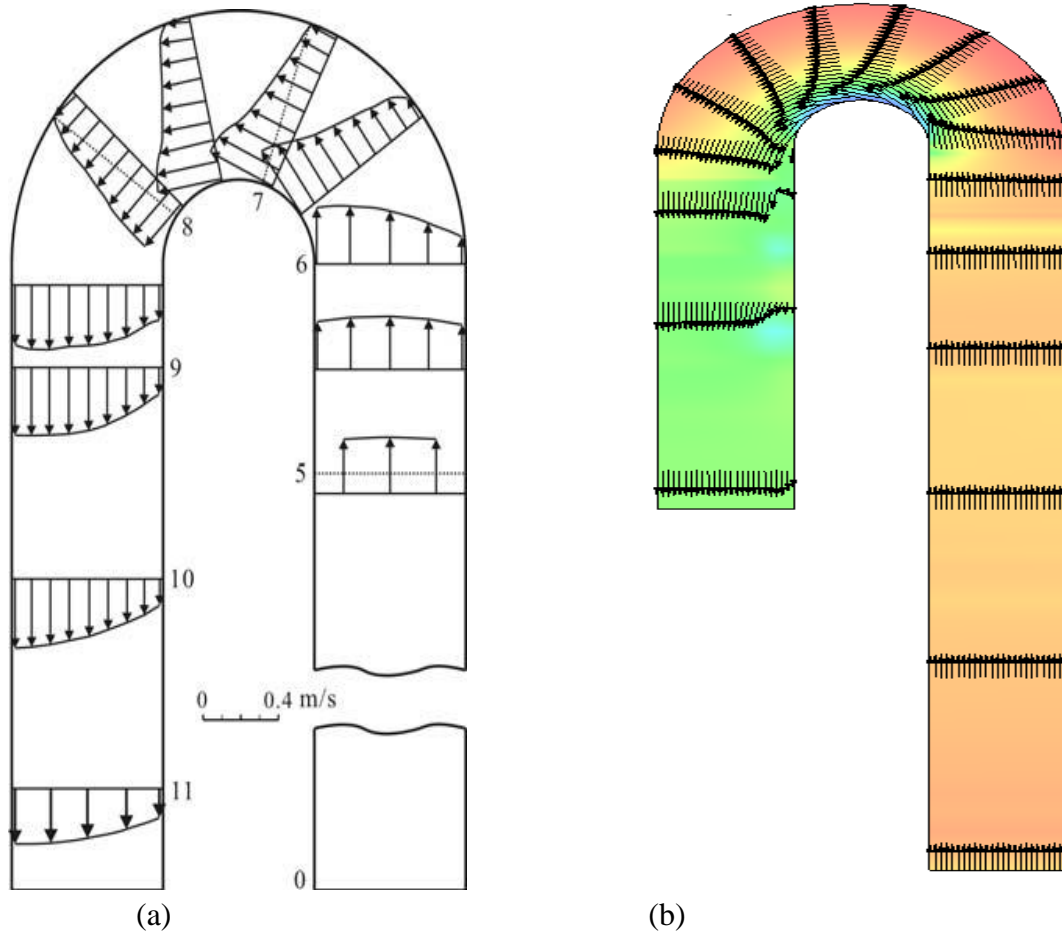


Figure 4.5: Comparison of width wise variation of velocity vector at different section of the 180° sharply curved channel (Case S_1C_1) (a) Experimental by Rozovskii (1961), (b) Computation by iRIC Nays2DH.

Figure 4.5 (a) present the measured result by Rozovskii (1961) and 4.5 (b) shows the field predicted velocity vector field in the channel bend. The simulated result by iRIC Nays is found to be well compared with the experiment. For both the cases the velocity of flow is greater in the inner section than the outer section. The velocity in the inner bend is found to be decreased when the flow enters the straight portion after the bend. From experimental and iRIC Nays result, it is observed that in the straight portion at outlet, the outer bank velocity is higher than inner bank. For a sharp bend, the radius of curvature is in the order of the width of the channel, thus the effect of secondary flow is very strong.

4.3 SIMULATED RESULT OF 180° MILDLY CURVED CHANNEL (Case S_1C_2)

In this section, the experiment by De Vriend (1979) is numerically reproduced. The channel consists of 1.7 m wide flume having a rectangular cross section. The bottom of the channel is horizontal and the sidewalls are vertical. The radius of curvature of the flume axis in the

bend is 4.25 m and the upstream and downstream straight reaches have an effective length of about 6.0 m. The ratio of radius of curvature to the channel width is 3.5. The discharge at the inlet is $0.0671 \text{ m}^3/\text{s}$, the averaged velocity is 0.202 m/s and the averaged flow depth is 0.1953 m . The logarithmic laws at the sidewalls were used in the numerical simulation. The simulation reach consists of the U bend and the effective straight reaches at the upstream and downstream. Constant discharge at upstream and constant depth with zero velocity gradients was given as downstream boundary conditions.

Figure 4.6 plots the simulated flow field as velocity vector field and the surface elevation in shaded color. The velocity vectors at inlet and outlet straight portion are found to be uniform. The velocity along the inner bank is higher than the outer bank at the bend. Water surface elevation at inlet is higher than the outlet straight portion. At the bend, the water surface elevation along the outer bank is higher than the inner bank.

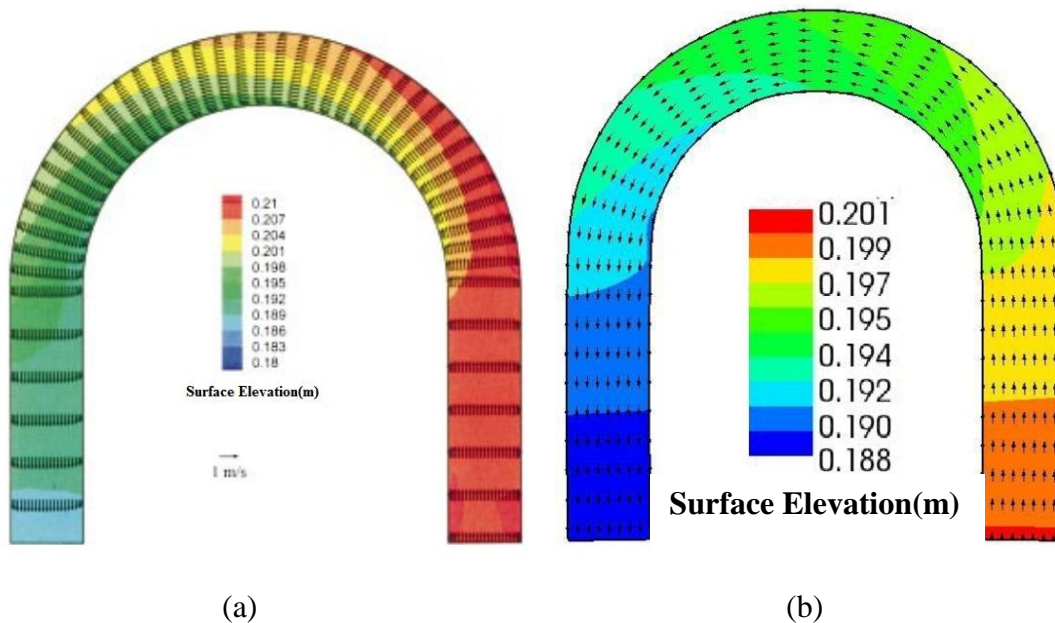


Figure 4.6: Velocity vector super imposed on the surface elevation contour (Case S_1C_2) (a) Experiment by De Vried (1979) (b) Simulation by iRIC Nays2DH.

The comparison of the simulated velocity with previous experiments is shown in Figure 4.7. Figure 4.7 (a) shows the experimental velocity distribution and Figure 4.7 (b) shows the computed velocity distribution. The comparison shows good agreement both at bend and straight portion of the channel. It is observed that the velocity vector along the inner bank is longer than the outer bank. The acceleration of the stream wise velocity at the inner bank is due to the transverse convection of momentum induced by the secondary current. However, for this mild bend, the radius of channel curvature is much larger than the width of the channel and thus the effect of secondary flow not very strong.

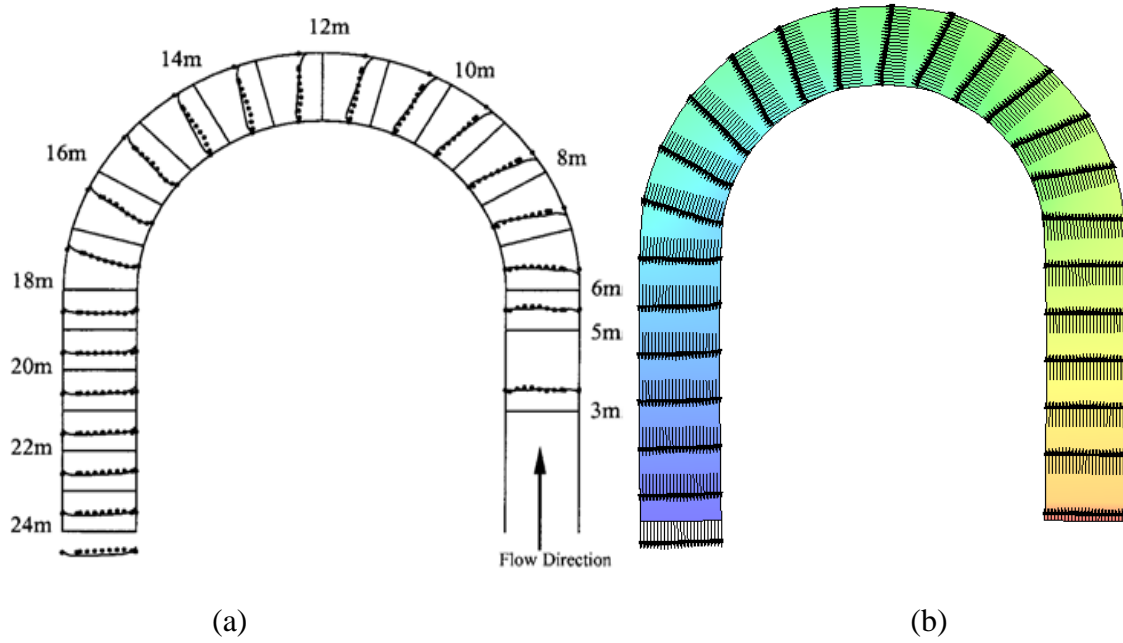


Figure 4.7: Distribution of depth-averaged velocity 180° mildly curved channel (Case S_1C_2)
 (a) Experiment by De Vriend (1979), (b) Simulation by iRIC Nays2DH.

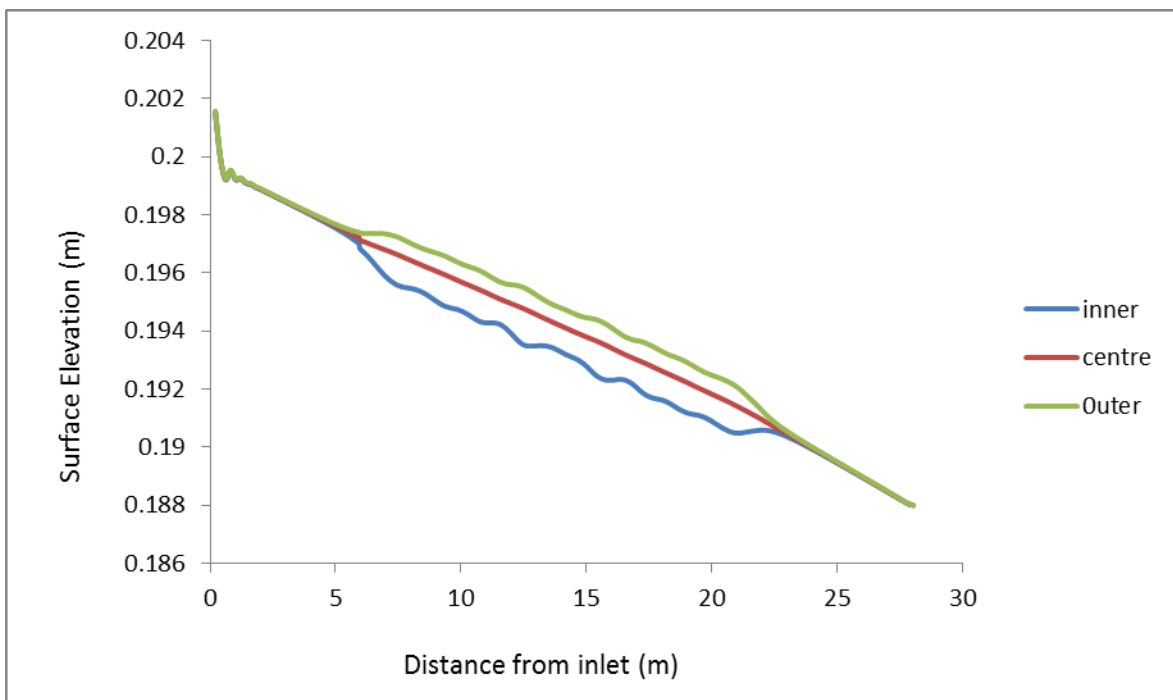


Figure 4.8: Water surface profile of 180° mildly bend channel (S_1C_2) .

The comparison of simulated water surface elevation at the inner bank, centerline, and outer bank was plotted in Figure 4.8. From the Figure 4.8, it is clear that the water surface elevation at the outer bank is much higher and at the inner bank is much lower than that of center of the channel water surface elevation throughout the bend. The rise of flow at the outer bank results from the centrifugal force. This change in water surface elevation starts from just before to the entrance of the bend and continued up to just after the exit of the bend.

Chapter 5

SIMULATION OF FLOW FIELD AROUND GROIN

5.1 INTRODUCTION

2D numerical model Nays2DH is used to simulate the flow field in a straight open channel with 45°, 90° and 135° groin angled with the flow direction. Depth-averaged k-ε model is used as turbulence closure model with finite differential advection as upwind scheme during simulation. The simulation has performed to evaluate and analysis the velocity profile and bed shear stress profile.

5.2 NUMERICAL TEST

5.2.1 Flow domain and hydraulic parameters

The hydraulic parameters for different test cases that were simulated shown in Table 5. 1. The parameters for case 1 of flow in a straight open channel with groin of 90° angle to the direction of flow were taken the same as the experiments by Rajaratnam and Nwachuku. In their experiment, a 37 m long, 0.9 m wide and 0.76 m deep flume with smooth bed and sides were used. The groin was an aluminum plate with 3 mm thickness and 152 mm length and was projected partly above the water surface. The hydraulic parameter for the 45° and 135° angled groin are the same as case 1.

Figure 3.3 in Chapter 3 shows the sketch of the flow domain for flows in a straight open channel with groin of 90° angled to the direction of flow which was performed under the same conditions of the experiment conducted by Rajartnam and Nwachukwu. Figures 3.4 and 3.5 in chapter 3 show the sketch of the flow domain for 45° and 135° which were performed under the same condition as case 1. For all these case, 120 * 20 grids were used considering fixed bed condition. Figures 4 shows a sample of computational mesh that consists of 120 grids in longitudinal direction and 20 grids in transverse direction.

For all the cases, the computational domain was 6 m in length and 0.9 m in width. The upstream and downstream boundaries were located at 2m and 4m away from the groin, respectively. The constant discharge at upstream was 0.043 m³/s, and at the downstream the constant flow depth was 0.189 m. Manning's roughness coefficient $n = 0.01$ and the time step $\Delta t = 0.003$ sec are assigned in the present computation. The simulation are performed in fixed bed condition with bottom slope, $S_0 = 0.001$.

Quanhong and pengzhi also used the same experimental data of Rajaratnam and Nwachukwu to validate their model. Governing equations of their model were shallow water equations and depth-averaged k-ε model as the turbulence model. According to Quanhong and pengzhi

model, the computational domain was 6 m in length and 0.9 m in width. Flow flux of $0.047817 \text{ m}^2/\text{s}$ and water depth of 0.189 m are specified at the upstream and downstream boundaries, respectively. The simulation is performed under movable bed condition.

Table 5.1 : Model constant for nonlinear k- ϵ model

Cases	Groin		L (m)		W (m)	Q_0 (m^3/s)	h_0 (m)	S	n
	Position	U/s		D/s					
Case S_2C_1	45°	2	4		0.9	0.043	0.189	0.001	0.01
Case S_2C_2	90°	2	4		0.9	0.043	0.189	0.001	0.01
Case S_2C_3	135°	2	4		0.9	0.043	0.189	0.001	0.01

Here, L = length of the straight channel, w = width of channel, Q_0 = upstream discharge, h_0 = water depth at downstream, S_0 = channel slope, and n = Manning's roughness coefficient.

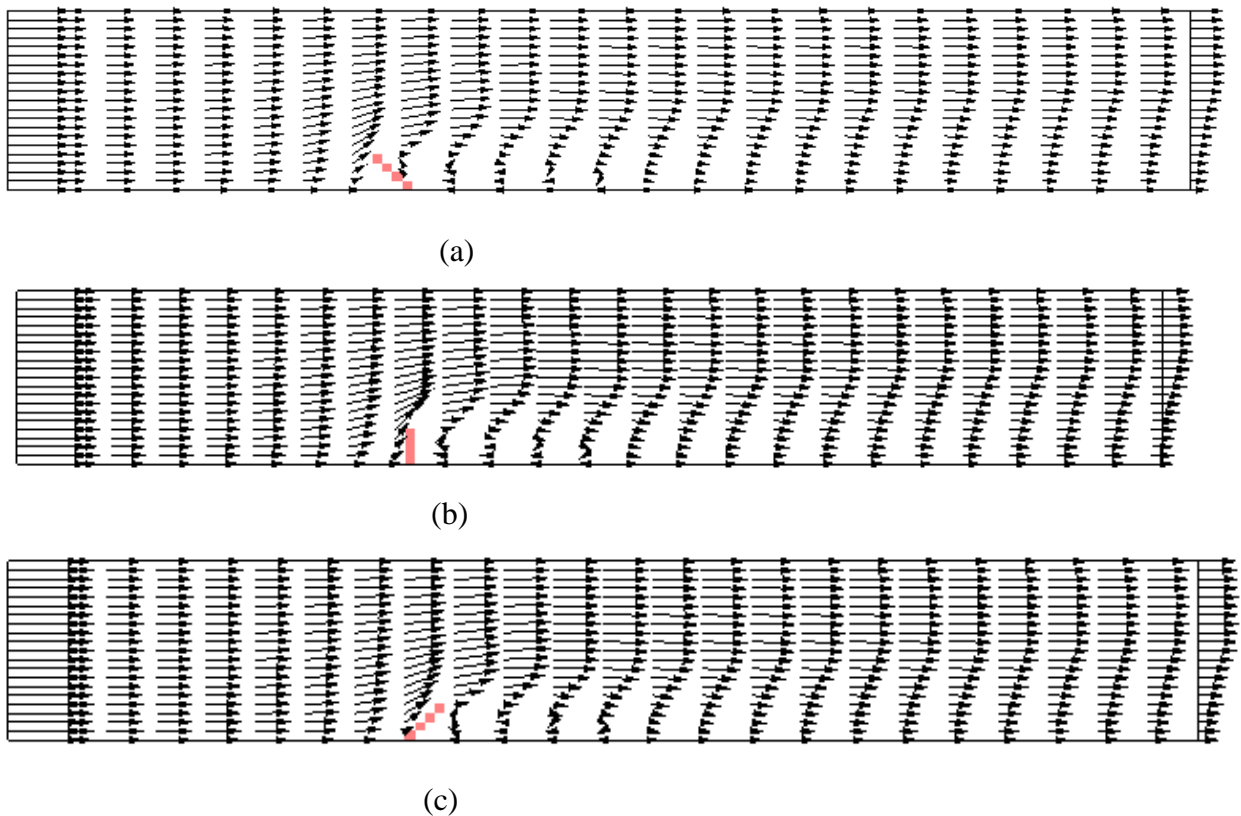


Figure 5.1: Computed velocity vector for (a) case S_2C_1 , (b) case S_2C_2 , (c) case S_2C_3 developed by iRIC Nays2DH.

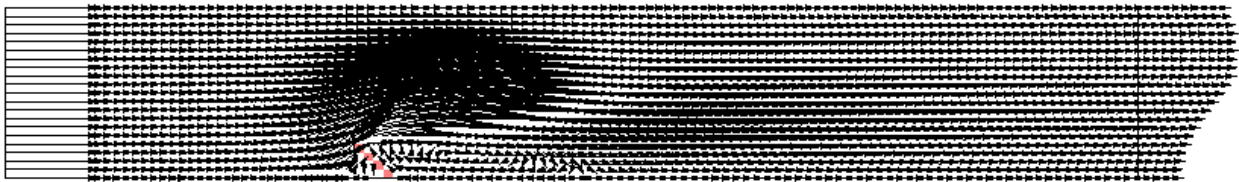
From the simulated results it is seen that the flow is deviated towards the left bank than the right bank due to obstruction of flow by groin.

5.2.2 Computational Scheme

The governing equation for mean velocities and turbulent flows were discretized with the finite difference method based on full staggered boundary fitted coordinate system. The basic equation are discretized as fully explicit forms and solved successively with the time increment step by step. It is solved using iterative procedure at each time step. Constant discharge at upstream and constant depth with zero velocity gradients were given as downstream boundary conditions. Finite difference scheme was used for the solution of the equations, where the nonlinear convection terms were discretized with the upwind scheme.

5.3. SIMULATION FLOW FIELD

Figures 5.2 show the predicted velocity vector of the flow field around the groin for different angles with the flow. For all the cases, the model is found to reproduce the general flow features of the flow field around the groin successfully. From the simulated results, it is seen that at the upstream boundary the flow is uniform and hence the flow vectors are straight and parallel to bank. However, when the flow approaches the groin, the flow is deviated towards the left bank compared to the right due to obstruction of flow by the groin. A recirculation zone is observed just downstream region of the groin for all the cases. Figure 5.2 depict that for case S_2C_1 (45° groin) the deviations of the vectors are higher than the case S_2C_2 (90° groin). 135° groin for case S_3C_3 shows the least deviation compared to other cases.



(a)



(b)

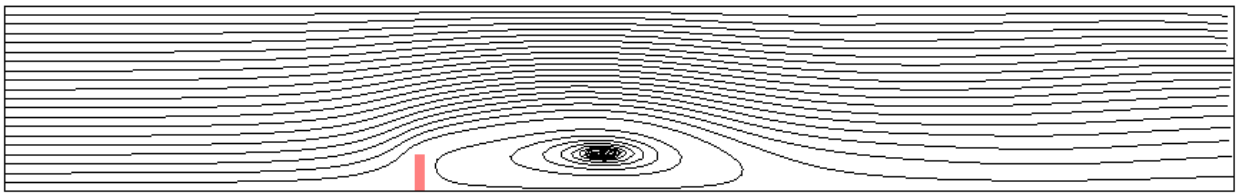


(c)

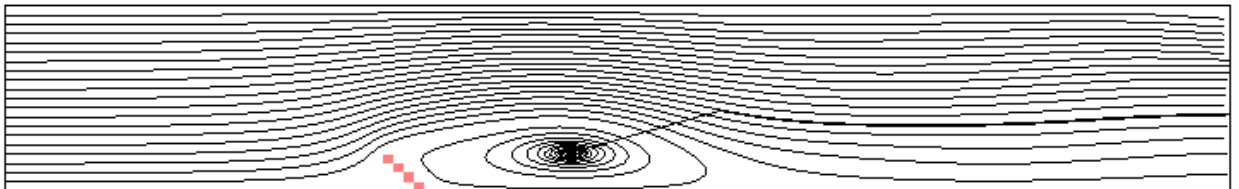
Figure 5.2: Computed recirculation around groin for (a) case S_2C_1 , (b) case S_2C_2 , (c) case S_2C_3 developed by iRIC Nays2DH.

5.3.1 Streamline

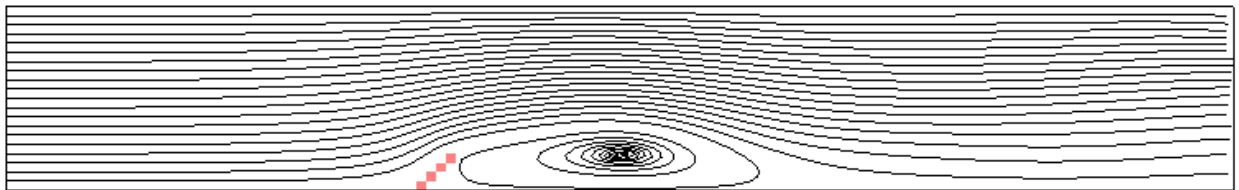
Figure 5.3 shows the streamline around a groin, which is obtained by the present study. From the streamline contour it is found that at the position of groin head the flow is deviated towards the opposite bank and at the downstream of the groin there is a circulation. Figures 6.3 depict that case S_2C_1 (45° groin) the deviations of streamline are higher compared to case S_2C_2 (90° groin). 135° groin for case S_2C_3 shows the least deviation compared to the other cases. The length of circulation zone at downstream of the groin is also higher for case S_2C_2 and lower in case S_2C_3 .



(a)



(b)



(c)

Figure 5.3: Streamline around a groin for (a) case S_2C_1 , (b) case S_2C_2 and (c) case S_2C_3 developed by iRIC Nays2DH.

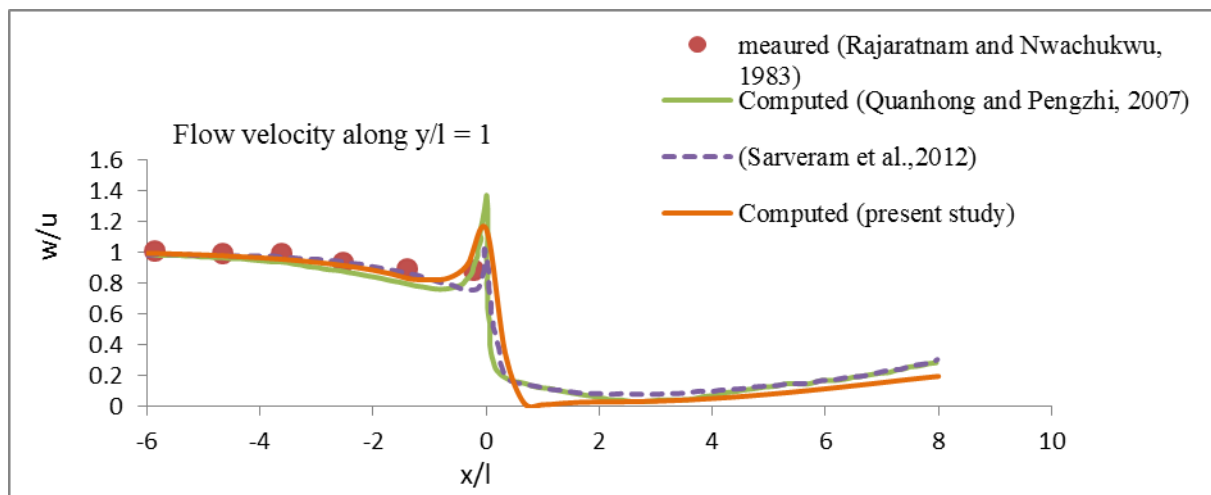
5.4 COMPARISON OF SIMULATED RESULT WITH PREVIOUS STUDIES

Simulated results such as computed velocity profiles and bed shear stress profile for 90° groin (case S₂C₂) are compared with previous experimental as well as available previous simulation results. The comparison is described in the following sections.

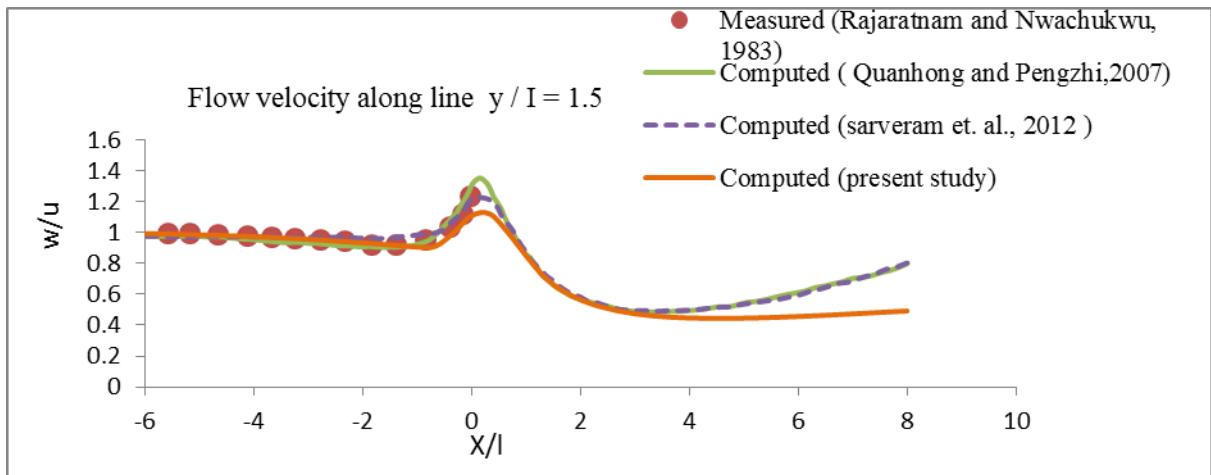
5.4.1 Computed Velocity profiles

For 90° groins, the resultant velocity profiles are compared with available experimental result measured at $y/l = 1.0, 1.5, 2.0, 3.0$ and 4.0 , where $l = 152\text{mm}$ is the length of the groin. Figure 8 shows the comparison of velocity profiles for different lateral distance (y/l). Here, the initial flow velocity profiles for different lateral distance (y/l). Here, the initial flow velocity and water depth were $U_0 = 0.253\text{ m/s}$ and $H = 0.189\text{m}$, respectively. In the figure, all the velocities were normalized by U_0 . In the figure, $x/l = 0$ indicated the groin position along flume direction.

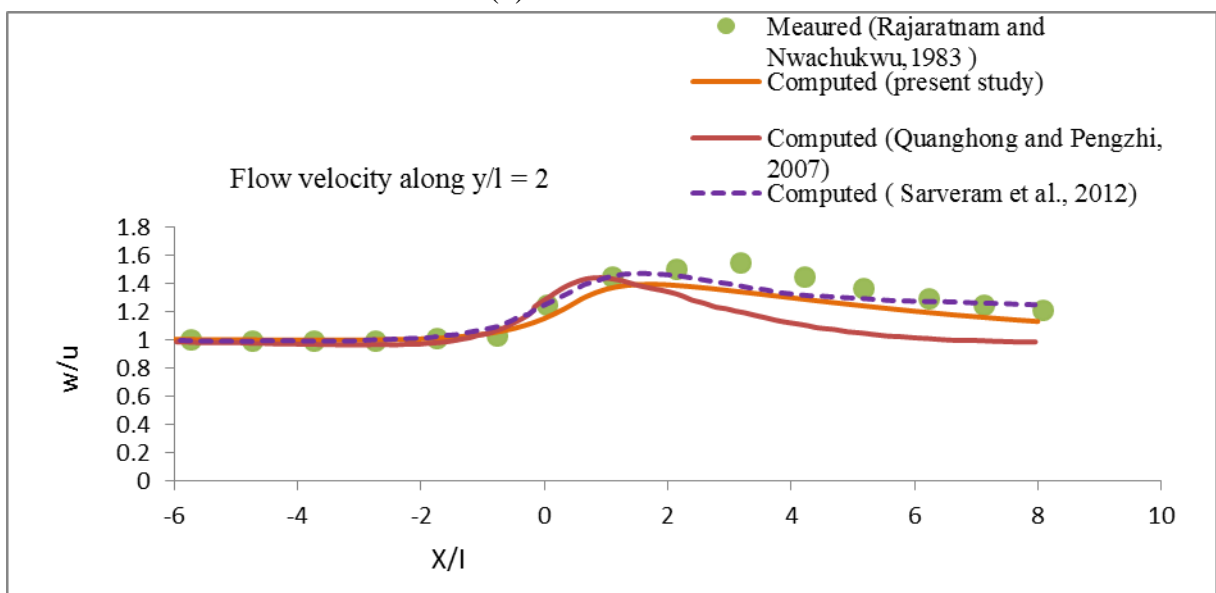
Good agreements are found between experimental and calculated results. For the velocity profiles, the only large discrepancy occurs at $y/l = 2$. Where the calculated results underpredict the experimental data in the downstream zone of the groin. It is noticed that the numerical result reported by Quanhong and pengzhi and Sarveram et al. also underpredicted the experimental data largely in this region. This may be due to the very high velocity gradient arising in this region which makes the depth-averaged model inapplicable. Otherwise, the possible reason may come from the experimental measurement errors in this region.



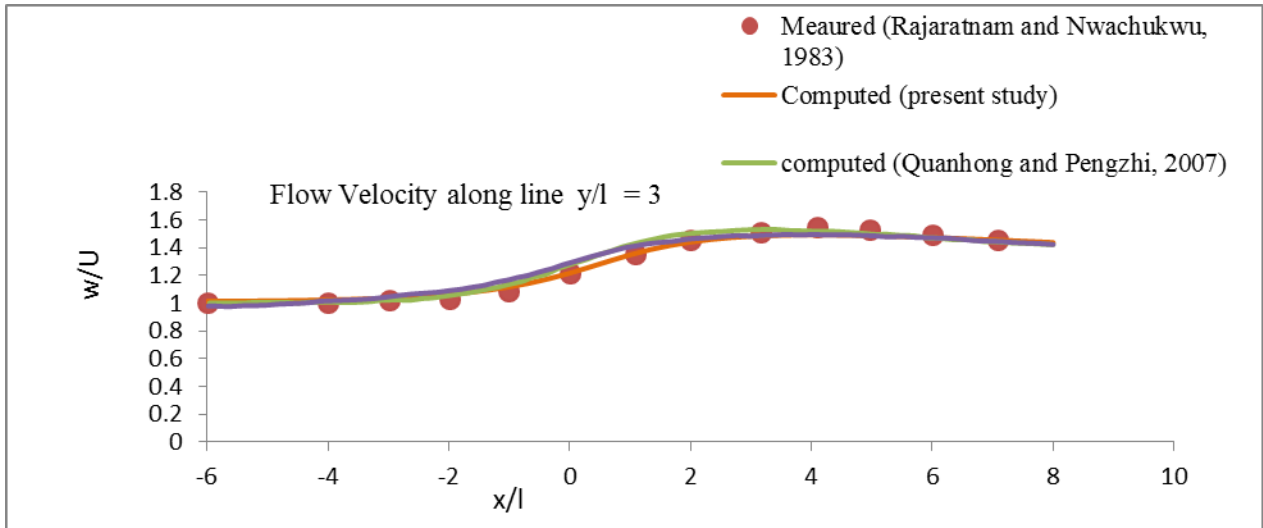
(a)



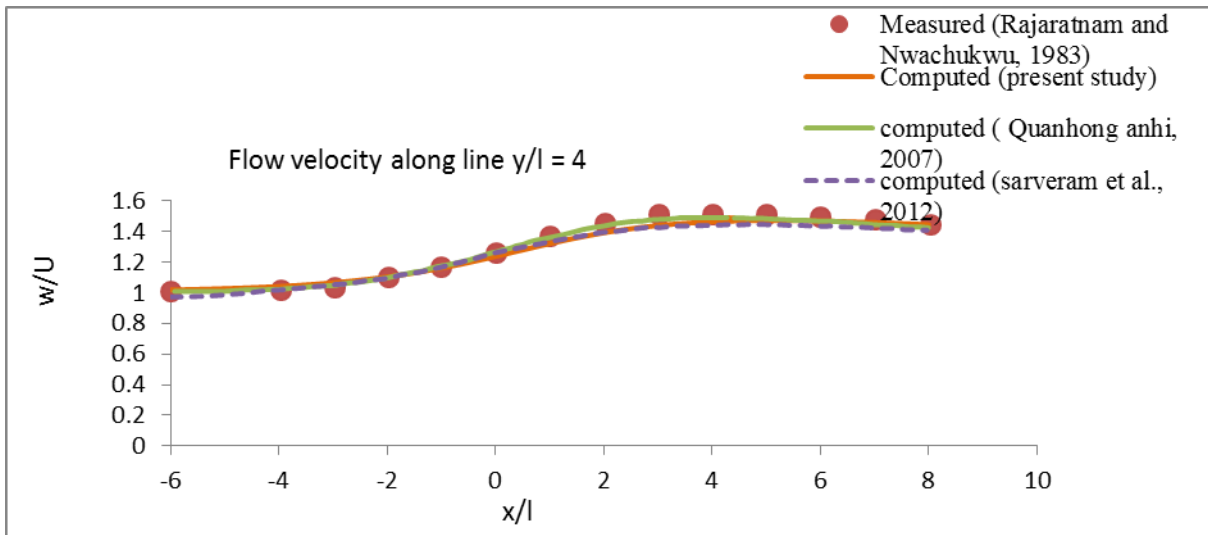
(b)



(c)



(d)

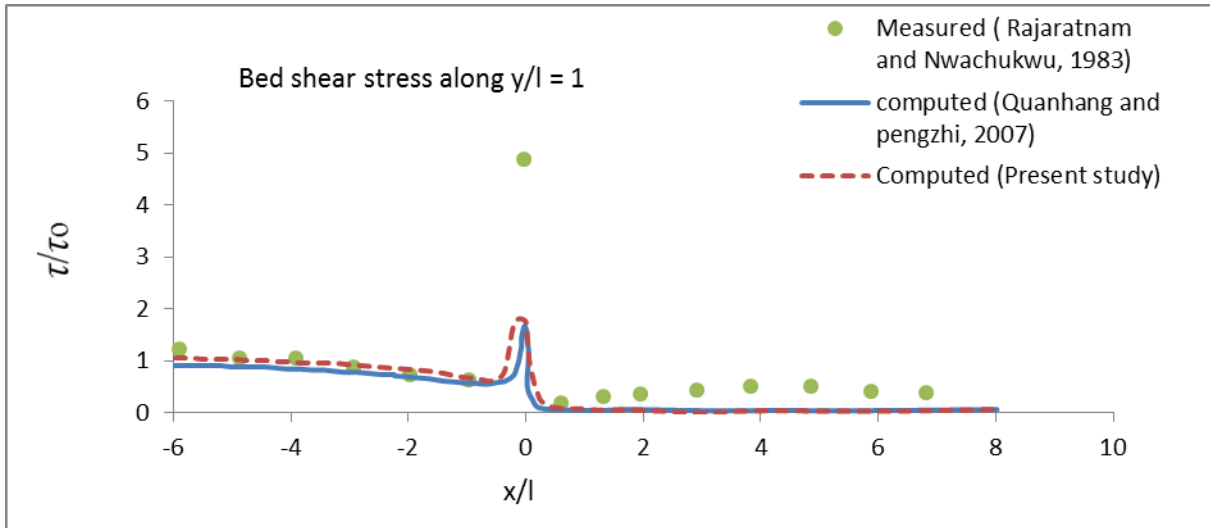


(e)

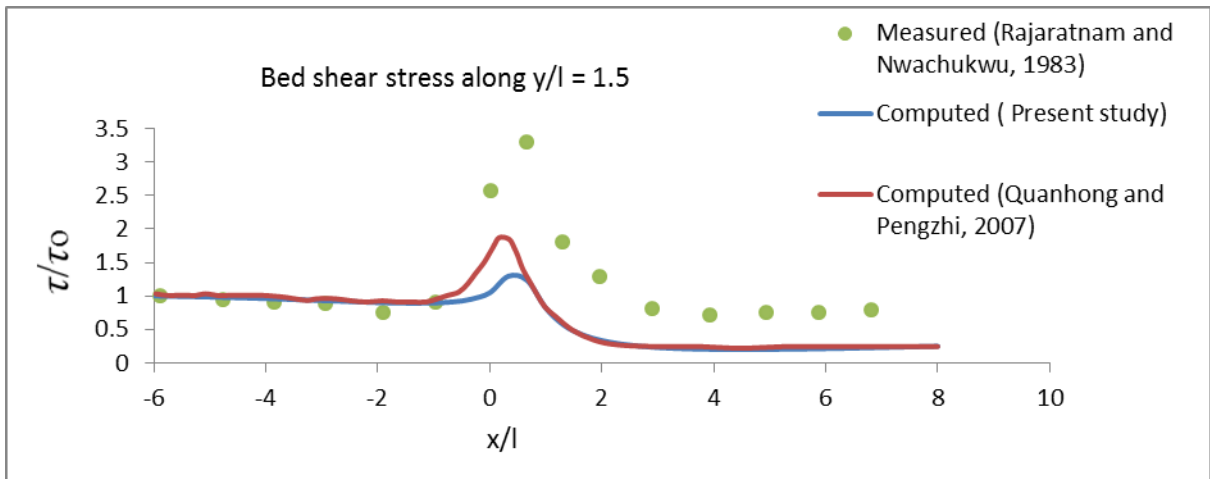
Figure 5.4: Comparison of resultant velocity profiles (W) with the available previous studies for 90° groin (Case S_2C_2).

5.4.2 Computed Bed shear stress profiles

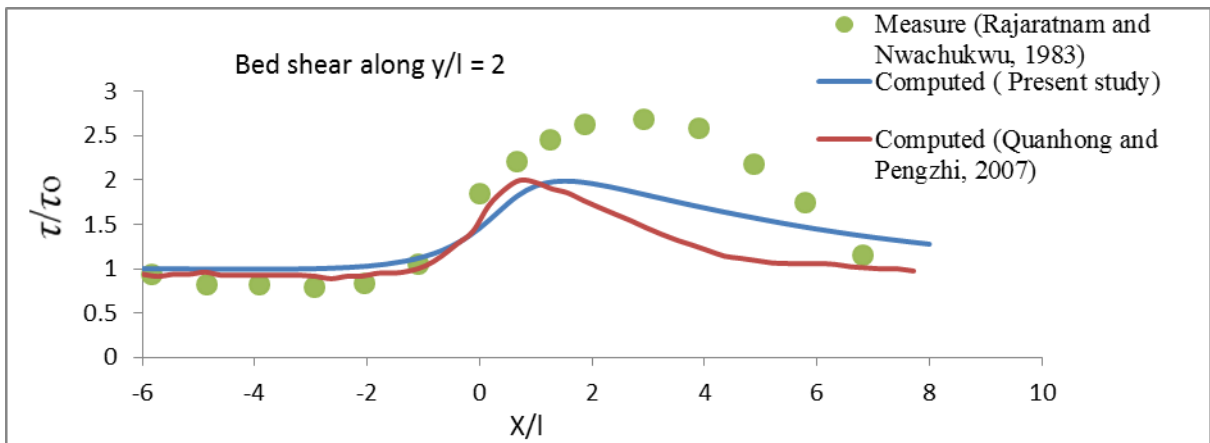
Figure 5.5 shows comparison of bed shear stress profiles (τ) of predicted results with the available previous studies. In the figure, all the shear stresses are normalized by $\tau_0 = 0.1293 \text{ N/m}^2$. The comparison between the numerical results and experimental data shows reasonable agreement. For the lateral sections up to $y/l = 2$, the simulated results underpredict the downstream shear stress slightly. The numerical results reported by Quanhong and pengzhi also show similar prediction. It may be the deficiency of the depth-averaged model to account for the high velocity gradient arising near to the groin.



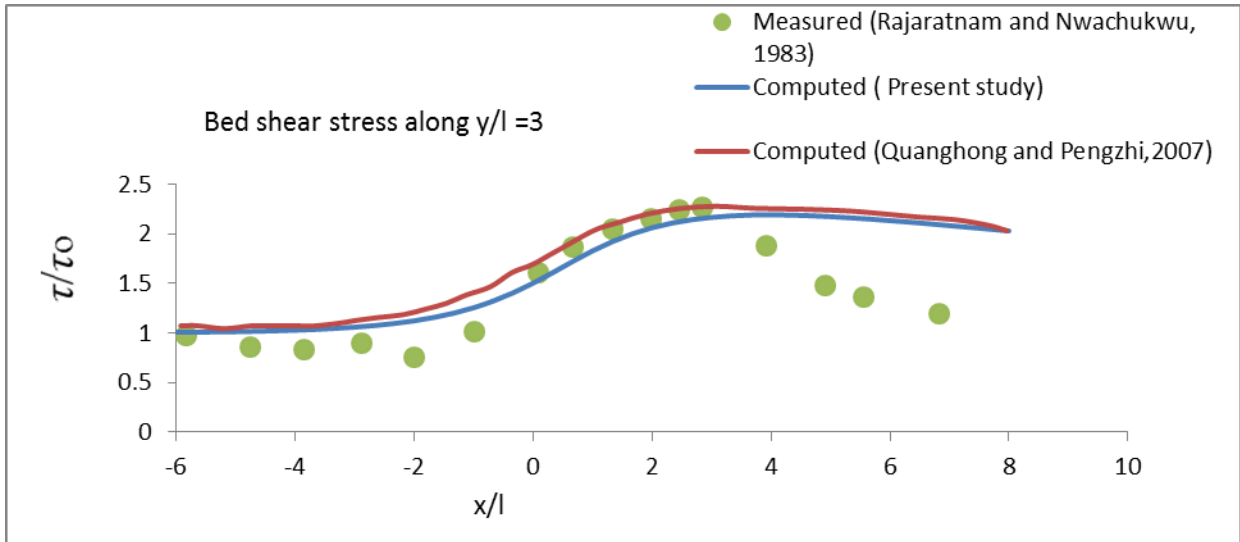
(a)



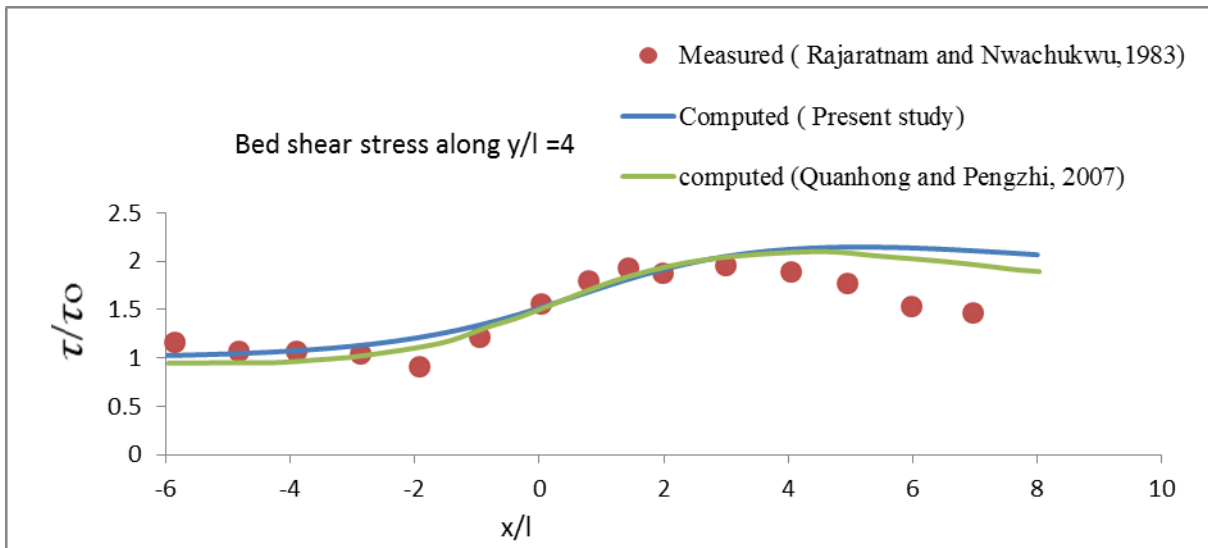
(b)



(c)



(d)



(e)

Figure 5.5: Comparison of bed shear stress profiles (τ) of predicted results with the available previous studies (Case S_2C_2).

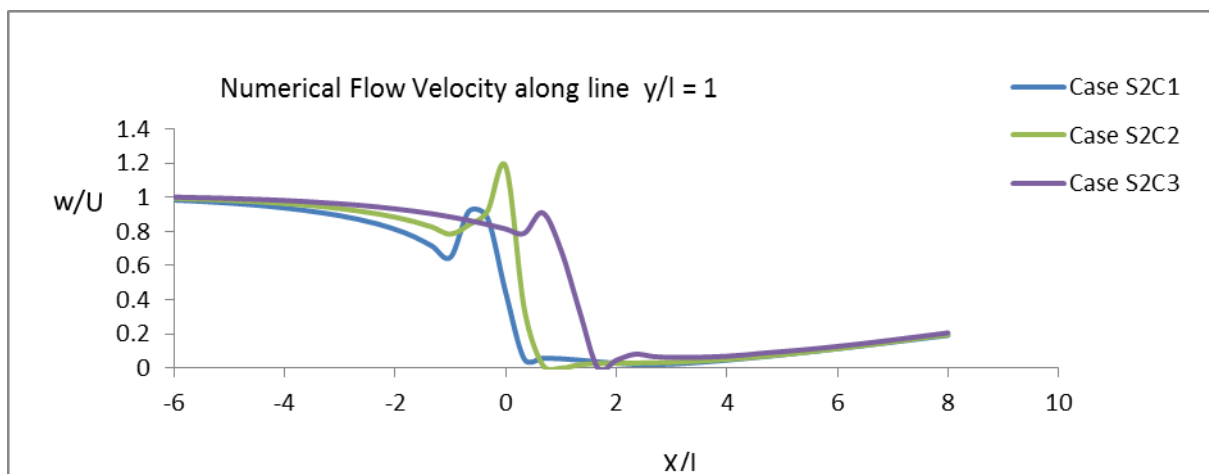
5.5 SIMULATION RESULT FOR DIFFERENT CASES

5.5.1 Predicted velocity profiles

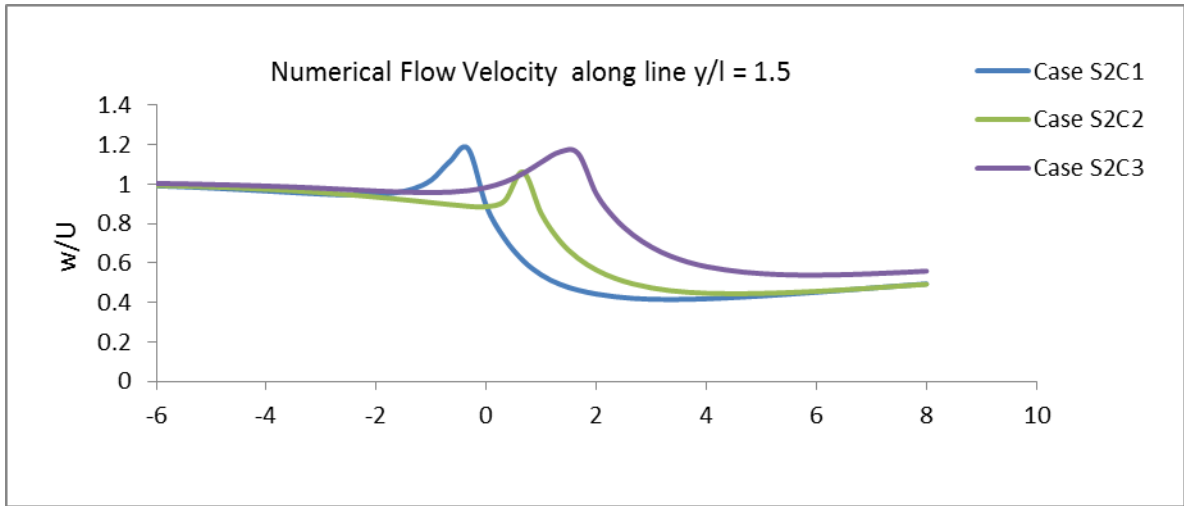
Figure 5.6 shows the predicted velocity profiles (W) of present study for case S_2C_1 , case S_2C_2 and case S_2C_3 . For each case, the longitudinal velocity profiles are compared at a lateral position of $y/l = 1.0, 1.5, 2.0, 3.0$ and 4.0 . In each case, the longitudinal velocity profiles are compared at a lateral position of $y/l = 1.0, 1.5, 2.0, 3.0$ and 4.0 . In the figure, all the velocities

are normalized by $U_0=0.253$ m/s and here $x/l = 0$ indicates the groin position in longitudinal direction. The comparisons among the three cases show reasonable differences. Along line $y/l = 1$, the peak of velocities is found at longitudinal distance of $x/l = -0.28, 0.0$ and 0.56 for case S_2C_1 , case S_2C_2 and case S_2C_3 , respectively. For $y/l = 1.0$ in all the cases, in all the cases, the velocity is found to be decreased from upstream velocity just before the position of groin head. In other words, in addition to the circulation zone at downstream of groin, a small low velocity zone is observed just upstream of groin at right bank. Along the line $y/l = 1.5$, the peak of velocities are found to be decayed with the longitudinal distances of $x/l = -1.0, 0.22$ and 0.67 for case S_2C_1 , case S_2C_2 and case S_2C_3 , respectively. The peak of velocities are found to be decayed with the longitudinal distance x/l . For $y/l = 2$, the peaks of the velocities are found at a distance of $x/l = -0.11, 1.22$ and 2.54 for case S_2C_1 , case S_2C_2 and case S_2C_3 , respectively. For $y/l \geq 2$, the decay of velocity along the downstream is found to be slower compared to the region $y/l \leq 1.5$. Along the line $y/l = 3$, the peak of the velocities is found at longitudinal distance of $x/l = 2.87, 3.53$, and 3.88 for case S_2C_1 , case S_2C_2 and case S_2C_3 , respectively. Along the line $y/l = 4$, the peak of velocities is found at longitudinal distance of $x/l = 3.33, 3.89$, and 4.44 for case S_2C_1 , case S_2C_2 and case S_2C_3 , respectively.

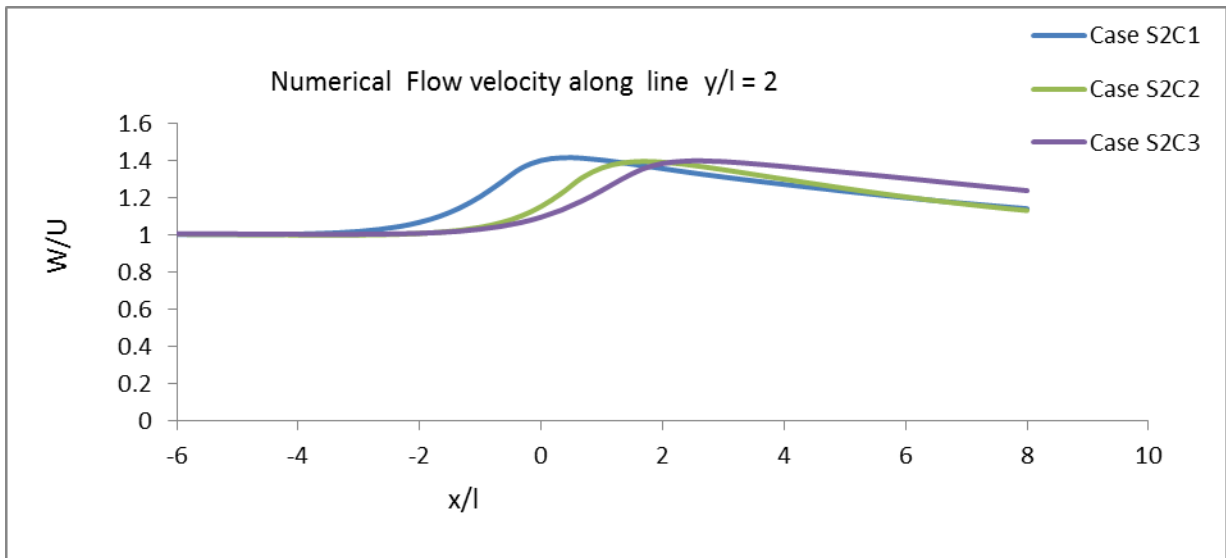
From the figures, it is observed that the peak of the velocity is found maximum velocity is found lower than the other two cases for all the section y/l . However, W/U_0 for 90° groin is found maximum for $y/l \leq 2$; and for $y/l > 2$, the velocity is maximum for 45° angled groin.



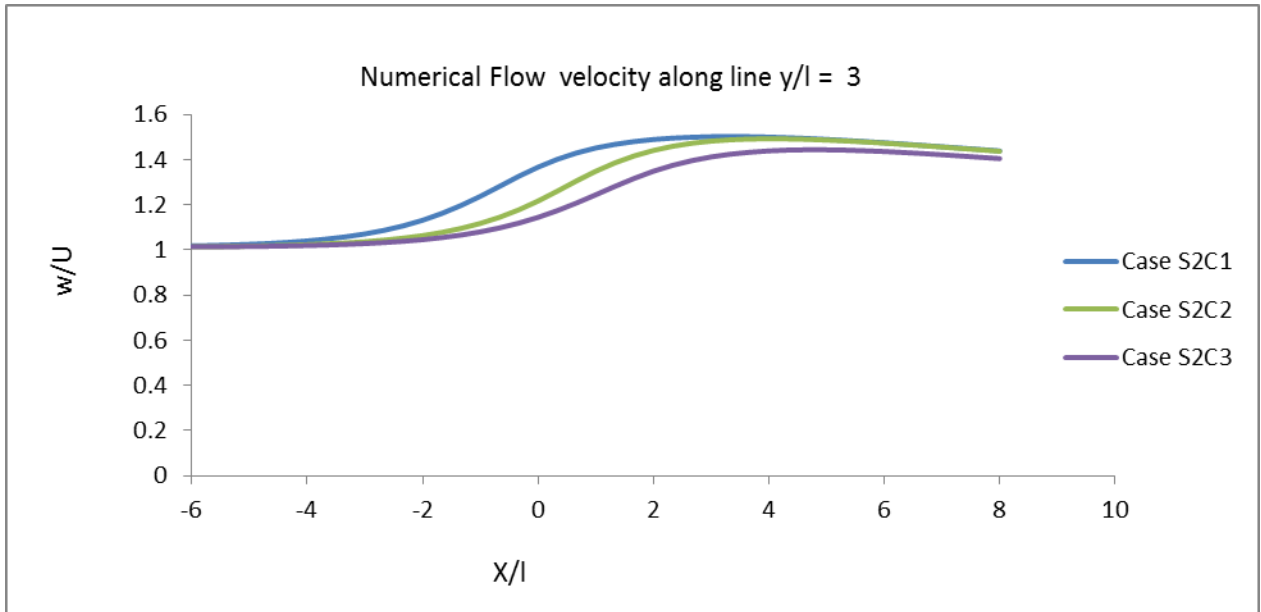
(a)



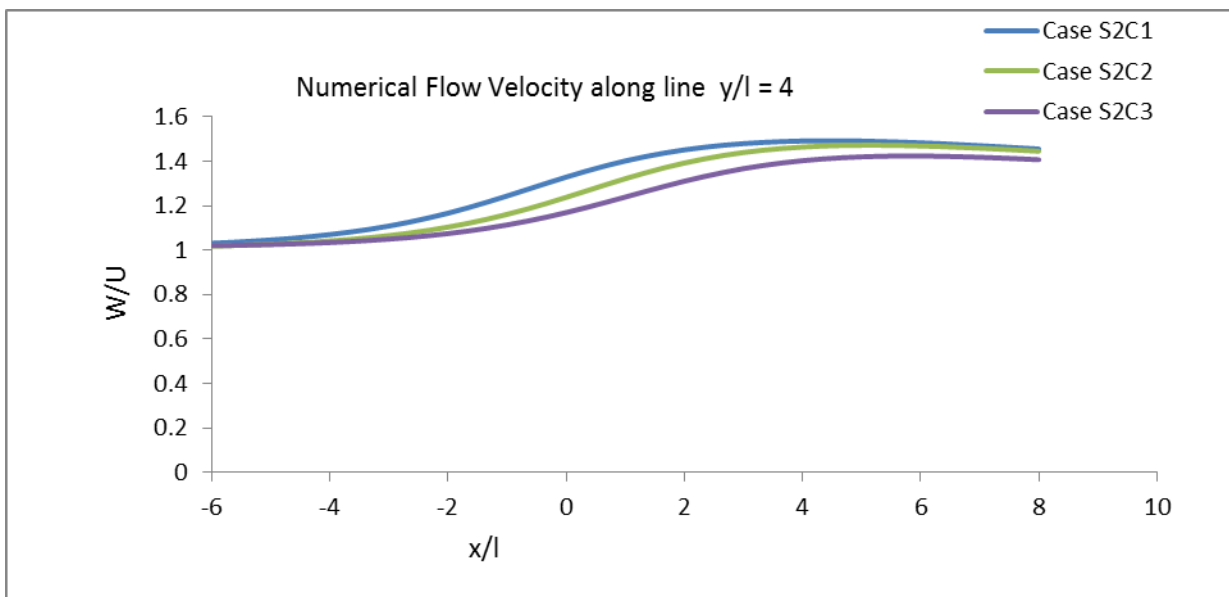
(b)



(c)



(d)



(e)

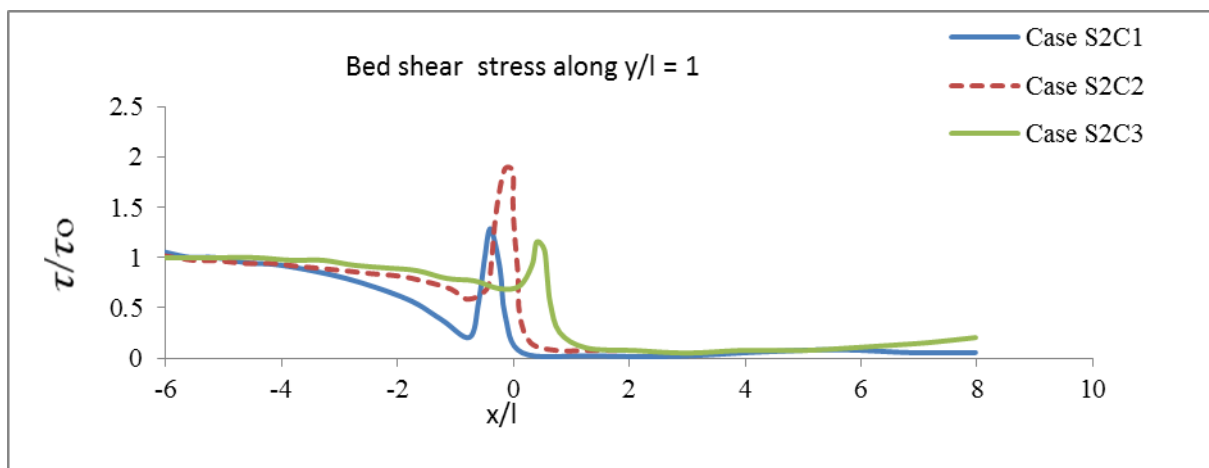
Figure 5.6: Comparison between resultant velocity profiles (W) of present studies for case S_2C_1 , Case S_2C_2 & Case S_2C_3 along lateral distance (a) $y/l=1$, (b) $y/l = 1.5$, (c) $y/l=2$, (d) $y/l=3$, (e) $y/l=4$.

5.5.2. Predicted bed shear stress profiles

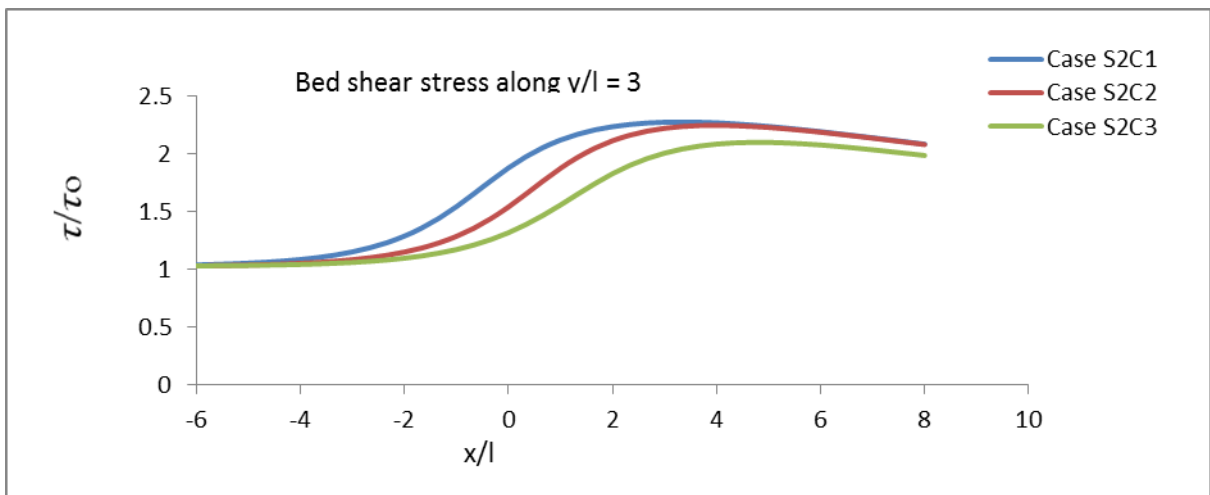
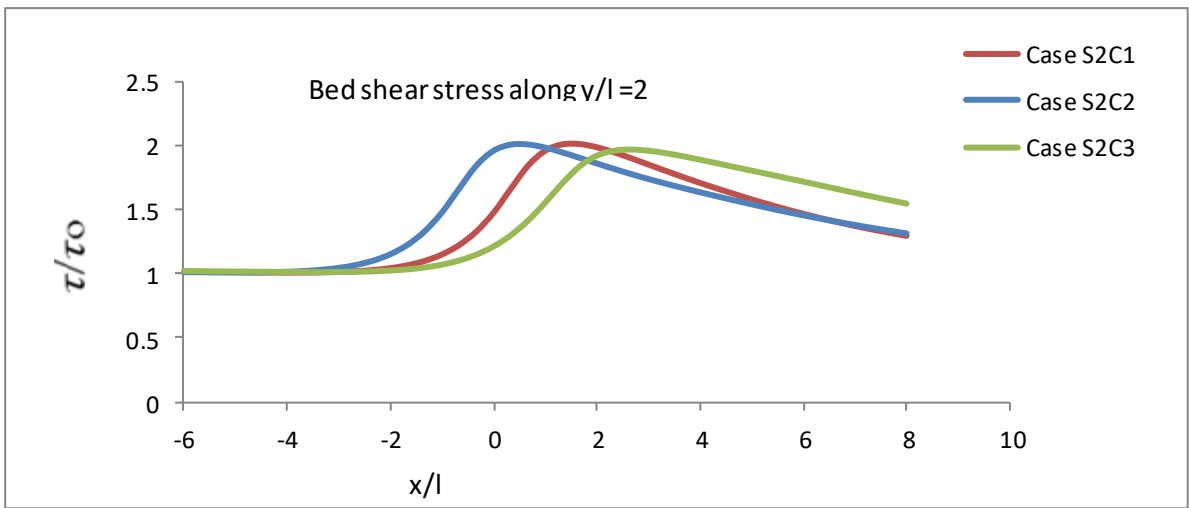
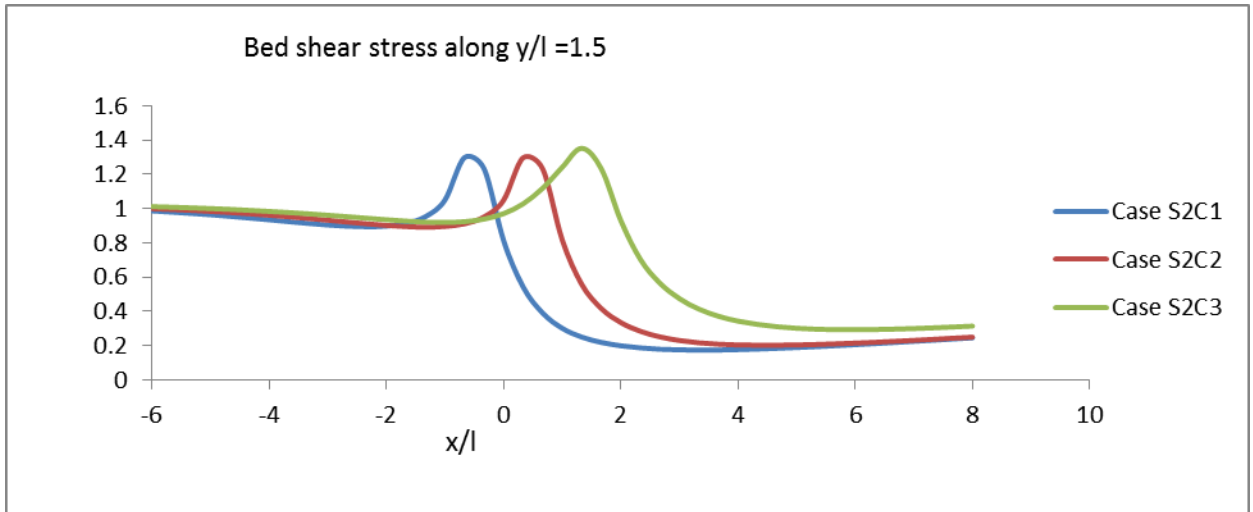
Figure 5.7 shows the predicted bed shear profiles (τ) of the proposed model for Case S_2C_1 , case S_2C_2 , and case S_2C_3 . For each case, the longitudinal shear stress profiles are compared at

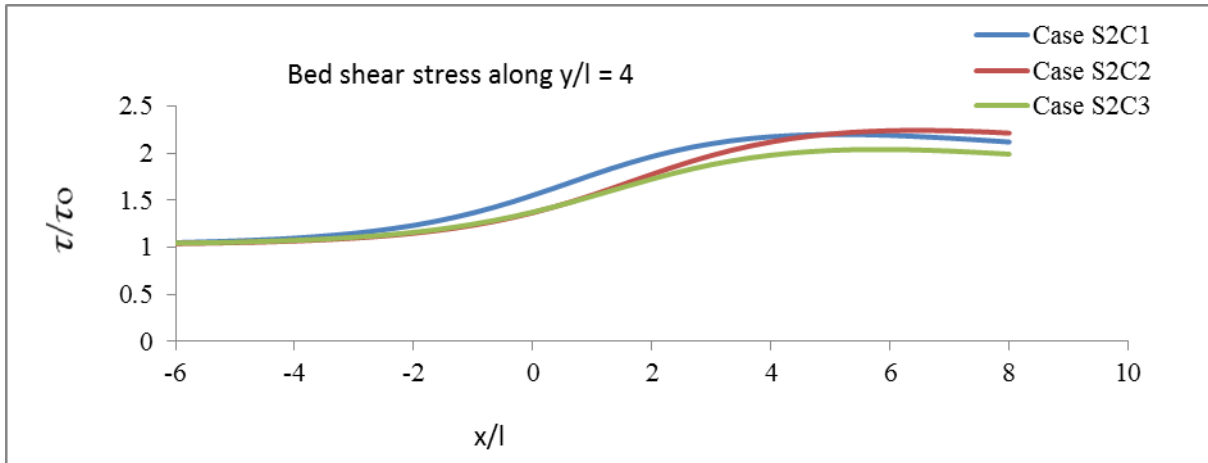
a lateral position of $y/l = 1.0, 1.5, 2.0, 3.0,$ and 4.0 . In the figure, all the shear stresses are normalized by $\tau_0 = 0.1293 \text{ N/m}^2$, which is the value of upstream region. Here, $x/l = 0$ is the groin position along longitudinal direction. The profiles of bed shear stress are found in similar pattern of velocity profiles. For different values of y/l , the peak of shear stresses is found at the same longitudinal distance (x/l) as reported in velocity profiles. For $y/l = 1.0$ in all the cases, the shear stress is found to be decreased from its upstream value just before the position of groin head.

From the figures, it is observed that the peak of bed shear stress is found maximum at the position of head of head of groin when $y/l = 1$. However, the position of maximum bed shear stress is found to be shifted towards downstream with increasing y/l . These peak shear stress are found to be shifted downstream with increasing y/l . These peak shear stresses are found to be decayed with the longitudinal distance x/l . However, for $y/l \geq 2$, the decay of shear stress along the downstream is found to be slower compared to the region $y/l \leq 1.5$. The maximum bed shear stress for case 3 is found lower than the other two cases for all the sections of y/l . However, τ/τ_0 for 90° groin is found maximum for $y/l \leq 1.5$, and for $y/l \geq 2$, the velocity is maximum for 45° angled groin.



(a)





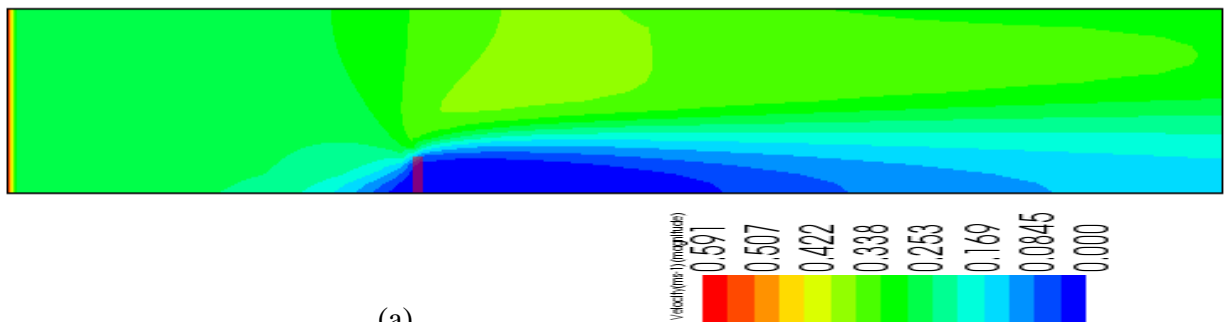
(e)

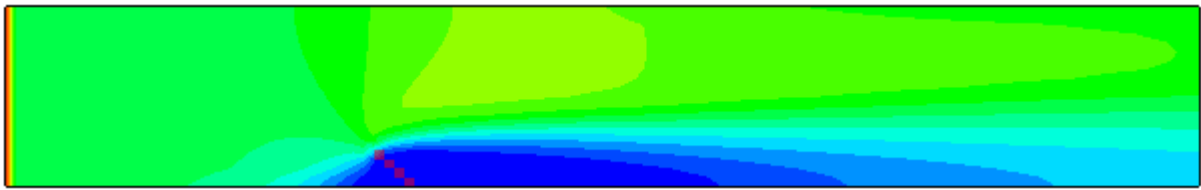
Figure 5.7 : Comparison between computed bed shear stress (τ) of the proposed model for case S_2C_1 , case S_1C_2 , and case S_3C_2 along lateral distance, $y/l = 1, 1.5, 2, 3,$ and 4 .

5.6 COMPUTED VELOCITY CONTOUR

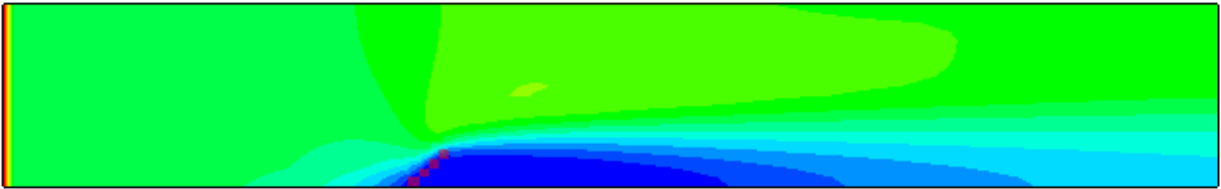
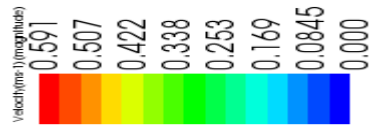
Figure 5.8 shows the simulated velocity contour in shaded color for case S_2C_1 , case S_2C_2 and case S_2C_3 , respectively. The results are found to be similar in nature. For all the cases, the velocity contour along the left bank is higher than right bank at the downstream region of the groin; it indicates the deflection of flow towards right bank and sheltering of flow by groin at east bank. The downstream circulation zone is found to be larger for 45° groin compared to 90° groin; similarly the circulation zone for 90° groin is found to be larger compared to 135° groin.

In the figure, the flow field is seen to be divided into four distinct regions: (I) the uniform flow at upstream end, (II) big circulation of low velocity zone at the downstream of the groin created due to sheltering of groin where the velocity is zero in the center of the circulation (III) a small low velocity zone near the foot at the upstream of groin, and (IV) high velocity zone opposite to the circulation zone created due to the deflection flow. The high velocity zone is found to be decayed towards downstream and the low velocity in circulating zone is found to be regained.





(b)



(c)

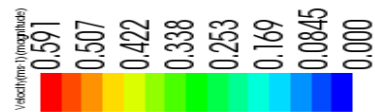
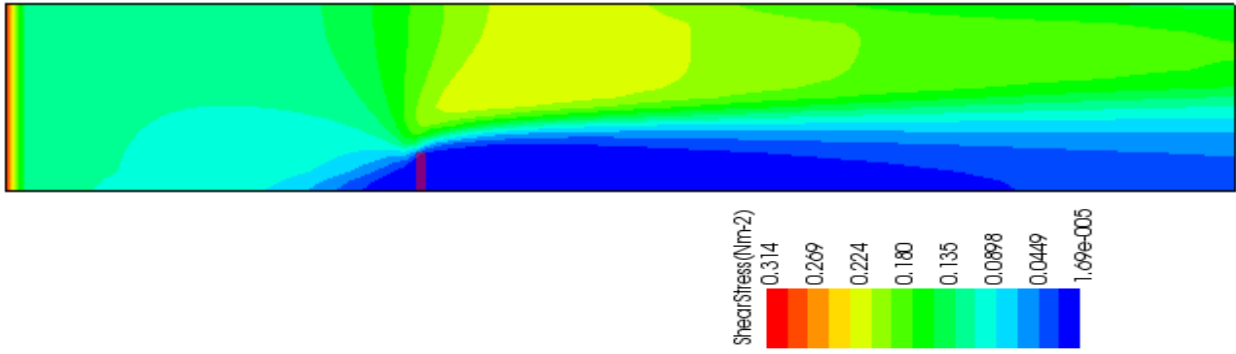


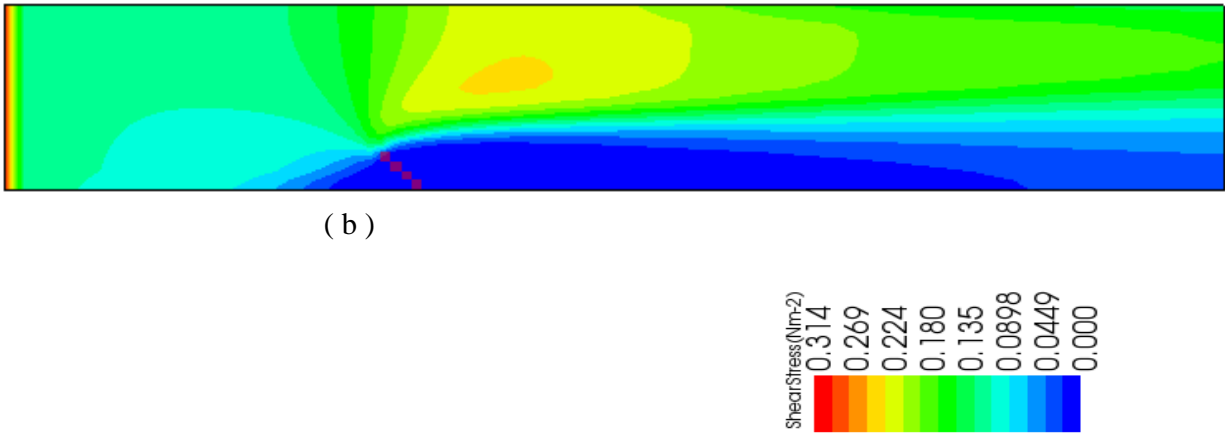
Figure 5.8: Velocity contoured around a groin for (a) case S_2C_1 (b) case S_2C_2 , and (c) case S_2C_3 at the end of simulation by iRIC Nays2DH.

5.7 COMPUTED SHEAR STRESS

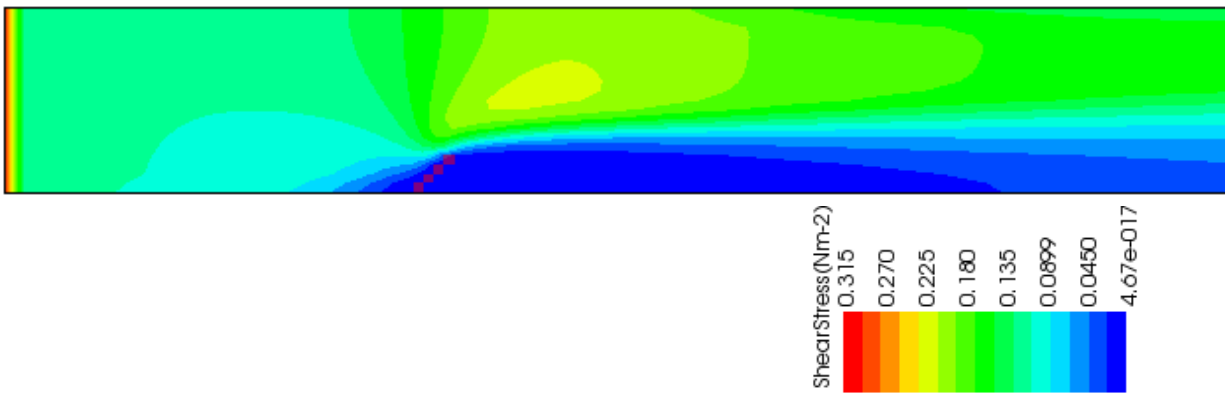
Figure 5.9 shows the simulated bed shear stress contour in shaded color for case S_2C_1 , case S_2C_2 and case S_2C_3 , respectively. The results are found to be similar in nature. Like the velocity contour, for all the cases, the shear stress contour along the left bank is higher than the right bank at the downstream region of the groin. Four distinct flow regions as described in velocity contour are also clearly visible in the contour of shear stress.



(a)



(b)



(c)

Figure 5.9 : Bed shear stress contour around a groin for test (a) case S_2C_1 (b) case S_2C_2 and (c) case S_2C_3 at the end of simulation by iRIC Nays2DH.

Chapter 6

LOCAL SCOUR AROUND GROIN

6.1 INTRODUCTION

iRIC Nays2DH numerical model is also applied to simulate an open channel with single barb with different orientation to observe the effect of barb on flow. Modeling of flow near barb is important, especially associated with developing scour hole and deposition of sediment. The numerical simulation has performed to evaluate the streamline variation, velocity contour line, bed change contour, bed elevation and depth contour diagram in the presence of barb and without barb. Besides, single barb, double barb has also studied with adequate hydraulic parameter. In this study, the numerical tests by Hossain et al (2012) is reproduced. He called groin as barb. Therefore, In this chapter barb is used instead of groin.

6.2 BED DEFORMATION AROUND SINGLE GROIN

Hossain *et al* (2012) has done an numerical simulation on a straight channel to observe the effect of barbs on channel bed configuration. Barbs are used to protect banks for meandering river as well as straight river. The primary function of barbs is to deflect the strong main flow away from critical zones towards the channel center and prevent erosion of banks (Hansen and winter, 1996). It also used on long reach of relatively straight or gently curving banks that need protection. The approaches to protect stream banks from erosion during periods of high flows including various bio-technical type channel revetments (Schiechtl and Stern, 1997). The length of this straight channel is 13.3m and wide is 0.8m which is generated by iRIC-Nays2D. The channel shape was considered as rectangular flat movable bed with simple cross section. The slope of channel is 0.005, the model is designed by subcritical flow. There are hundred grids in longitudinal direction and ten grids in lateral direction, respectively. The change of width of the grid channel in the direction of flow is constant. The model was run two settings: first, before constructing the barb and second, after constructing the barbs. At first flow approached into the channel pre-existing condition and find the velocity vector, flow depth and the elevation of the bed configuration, respectively. In this simulation, barb is used as a obstacle at one channel sidewall and it is 4.5m apart from the upstream. The barb length is taken 24 cm which is one third of the channel width. A rectangular riprap shape barb is formed at 45° angle with channel bank.

According to NRCS (2005), each barb extends from the bank-line to the proposed thalweg location. Generally the length of the barb not exceed one-third of the cross-section top width at bankfull stage, as Matsuura and Townsend (2004) observed in their study that, the overall length should not exceed about one quarter the channel-forming flow width. By decreasing the nodes elevation point at the barb end, the structure set as a sloping ridge from the bank to the main channel flow. The barb placed at an angle of 45° with the upstream bank of the

channel as NRCS (2005) state the horizontal angle between the tangential line placed along the upstream bank and the centerline of the longitudinal axis of the barb have varied from 30° to 60°.

The generated grid channel was used to set the calculation condition and simulation. The symbol L represents as the total length, B is the internal width and S is the slope of the channel, D is the normal flow depth, Q is the discharge, U is the velocity of the flow, B/D is the width to average flow depth ratio, C_f is the roughness coefficient correspond to d_{50} , where d_{50} is the mean sediment diameter and Froude number, $Fr = U / \sqrt{gD}$, here g is gravity acceleration.

Table 6.1: Detail flow calculation condition (for all the cases of series)

Cases	Barb angle	L	B	S	B/D	D	Q	U	F_r	D_{50}
		m	m	m/m	-	m	m^3/s	m/s	-	mm
S3C1	No Barb	13.3	0.8	0.05	18	0.044	0.028	0.64	0.977	0.77
S3C2	45 ⁰	13.3	0.8	0.05	18	0.044	0.028	0.64	0.977	0.77
S3C3	90 ⁰	13.3	0.8	0.05	18	0.044	0.028	0.64	0.977	0.77
S3C4	135 ⁰	13.3	0.8	0.05	18	0.044	0.028	0.64	0.977	0.77
S3C5	Two Barb	13.3	0.8	0.05	18	0.044	0.028	0.64	0.977	0.77

In the calculation condition the professional solver type with bed deformation was used. The finite differential methods of advection term was used as CIP method. For calculation of numerical simulation the cyclic boundary condition was used with initial water surface as uniform flow. The upstream velocity and water surface at downstream was also considered as uniform flow. Constant discharge time series were used from the beginning up to 5 hours. Output time interval was selected as 10sec. the calculation time was set according to Courant-Friedrichs-Lewy (CFL) condition as stated in equation (3). The CFL condition is necessary for convergence of flow while solving certain partial differential equations numerically by the method of finite difference (Courant et al. 1956).

$$\frac{\Delta t}{\Delta x/u} \leq C \quad \longrightarrow \quad \Delta t = C * \Delta x / u \quad (3)$$

Where C is a dimensionless constant and it's vary from 0.1 ~ 0.3. The maximum iteration times of water surface calculation was set as 20. The diameter of the bed material was used as 0.77 mm and bed roughness calculated from the bed materials using equation (1).

6.2.1 Velocity Field

From the simulation, the velocity vectors at water surface were found for pre-existing condition without barbs and with barbs, respectively. In this section, the outcomes of the flow fields and bed-topographies are given to understand the morphodynamics resulted from dealing of two settings: in before constructing the barbs and in the presence of the barbs. Figure 6.1 and 6.2 show the simulation result of velocity vector without barb structure after 1 hour and 5 hours, respectively. In the figures, the simulated results of present study (in Fig b) compared with the previous study by Hossain et al (2012) (in Figure a). Figure (b) found well agreed with Figure (a). At the time of entering the flow into the channel without barbs, the flow towards the channel creates parabolic flow patterns that is influence to formation of double row bar. The flow pattern is not change into entire channel after long time simulation. Single barb has installed to the purpose of simulation and run for 1 hour and 5 hours, respectively. Figure 6.3 and 6.4 show the simulated vector for 45° angled barb. In this situation owing to the flow separation at barb head return current developed at the upstream side and creates a mixing zone just behind the structure along the near bank line. The flow passes over the structure contraction-accelerated discharge occurs at the barb end. The convergence of these flow components result turbulent mixing around the barb head and vector flow directed towards the outer bank near water surface.

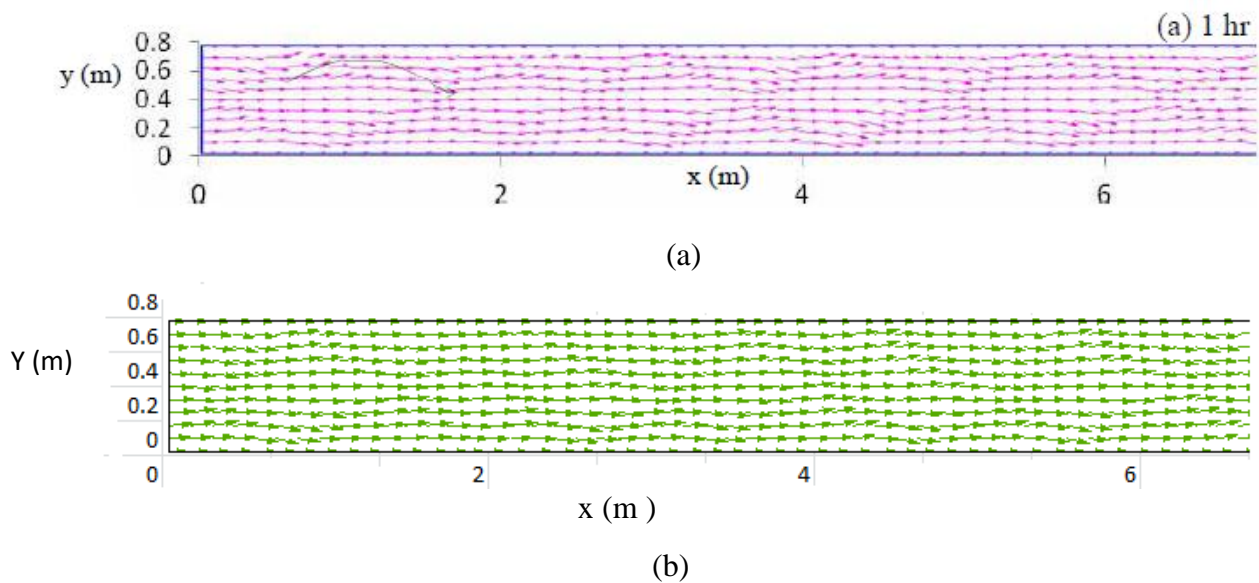
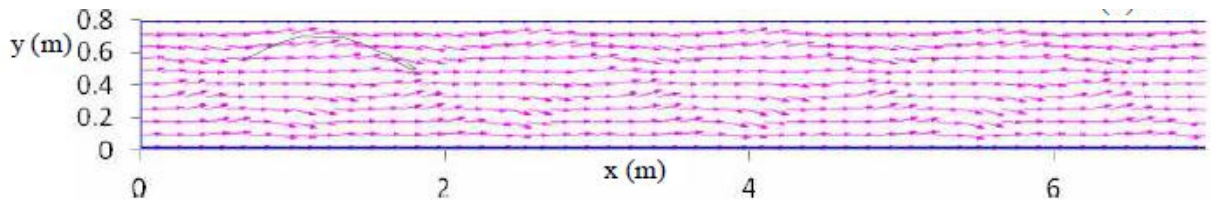
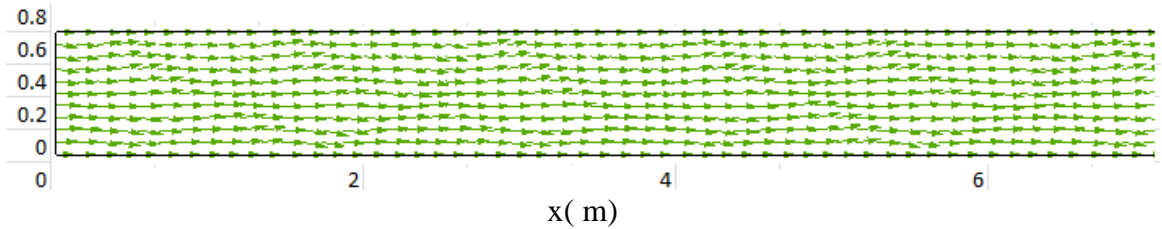


Figure 6.1 : velocity field simulation result at water surface into the channel without barb after 1 hour simulation (a) by Hossain et al (2012) (b) present study (Case S₃C₁).

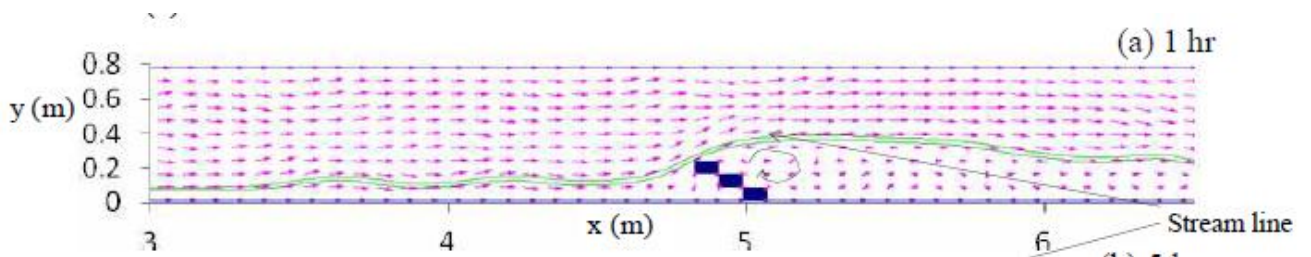


(a)

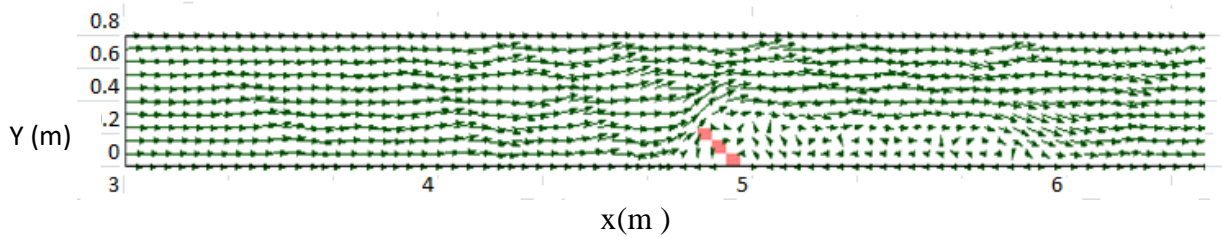


(b)

Figure 6.2 : Velocity field simulation result at water surface into the channel without barb after 5 hours (a) by Hossain et al (2012) (b) present study.



(a)



(b)

Figure 6.3: Velocity field with a barb installed one side of the channel after 1 hour simulation (a) by Hossain et al (2012) (b) present study (Case S₃C₂).

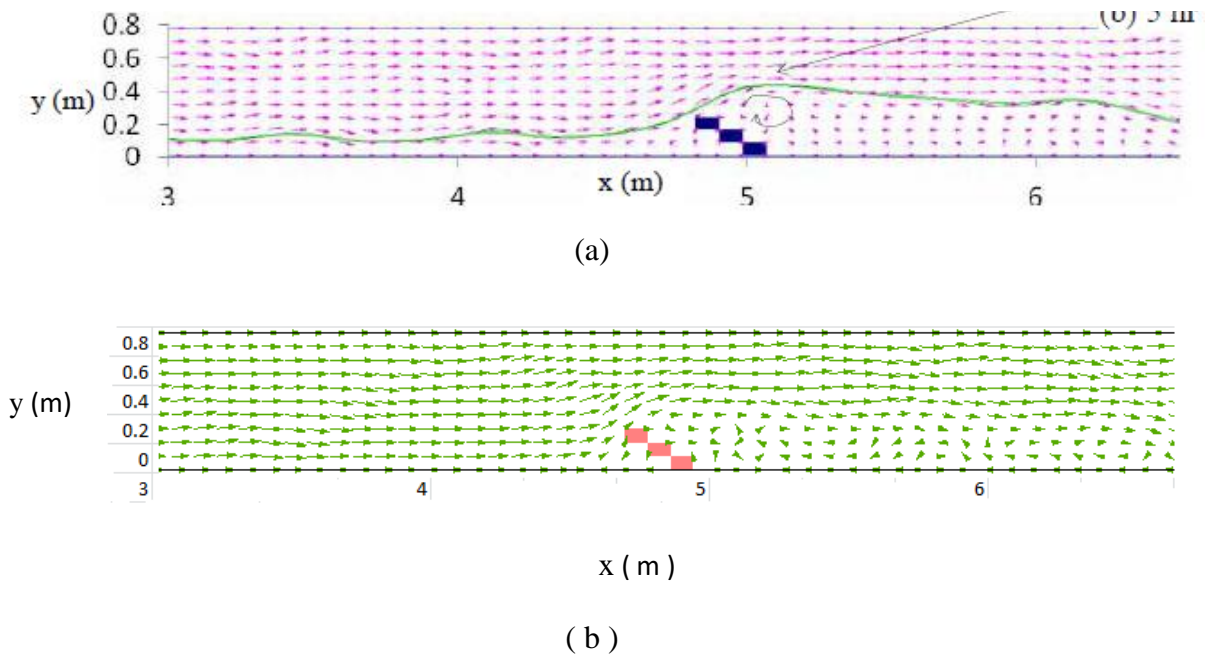


Figure 6.4: Velocity field with a 45° barb installed at one sidewall of the channel after 5 hour simulation (a) by Hossain et. al (2012) (b) present study (Case S₃C₂).

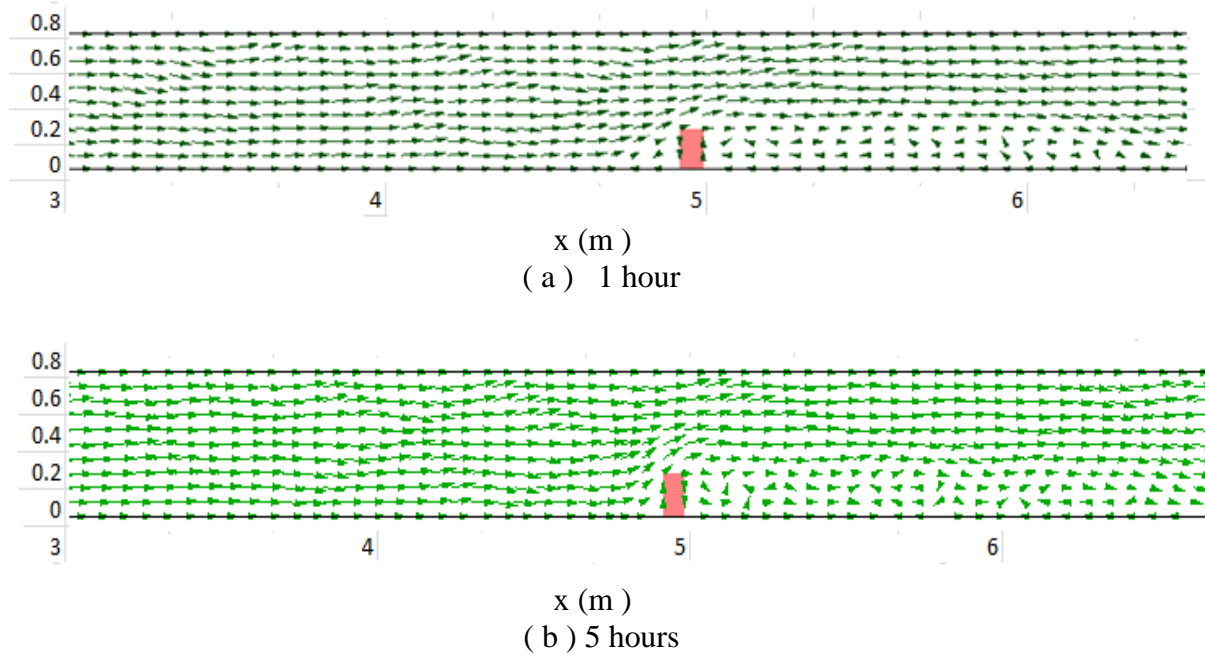


Figure 6.5 : Velocity field with 90° barb installed at one side of the channel (a) after 1 hour simulation, (b) after 5 hours simulation (Case S₂C₃).

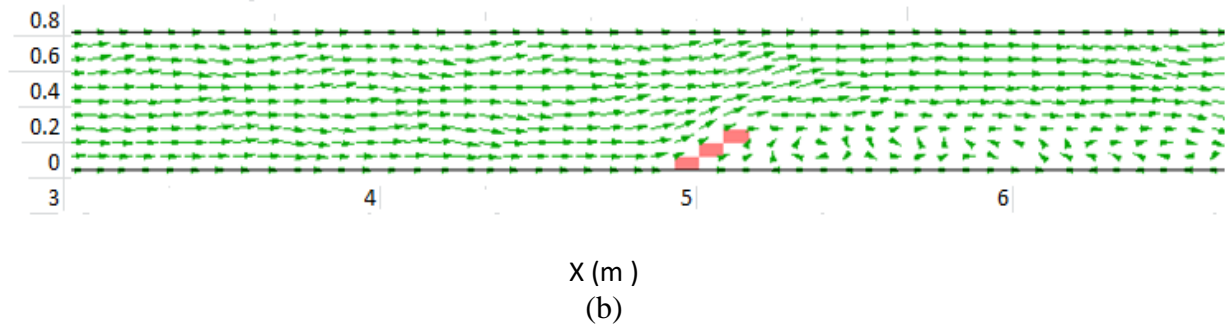
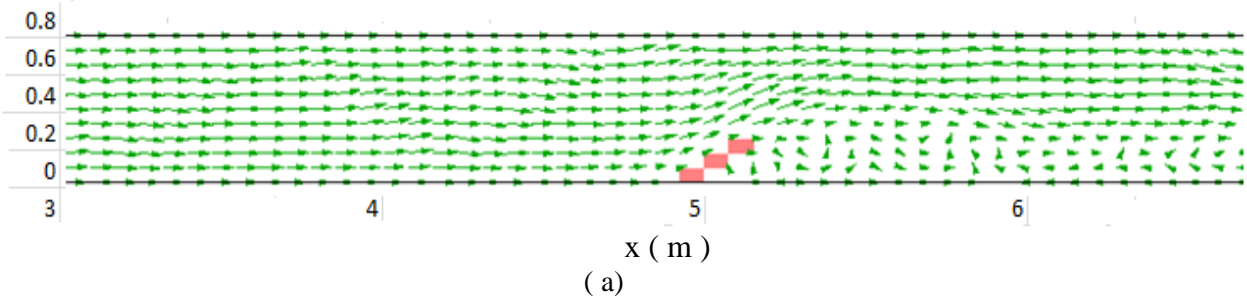
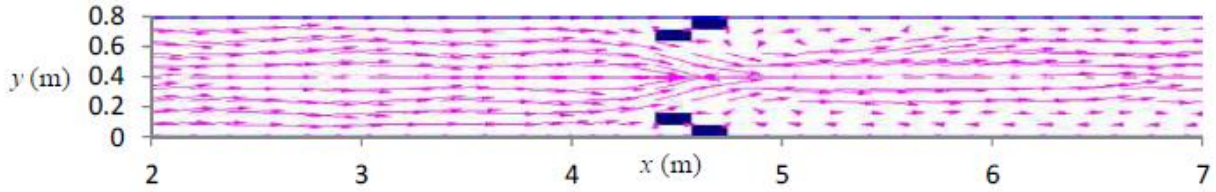
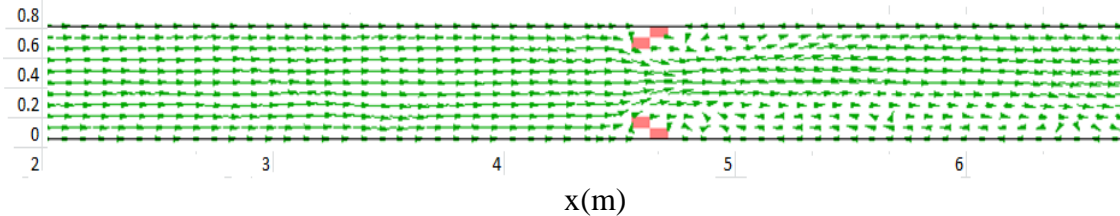


Figure 6.6 : velocity field with 135° barb installed at one sidewall of the channel (a) after 1 hours simulation (b) after 5 hours simulation.

Figure 6.5 shows the velocity vector with 90° barb for simulation of time 1 hour and 5 hours. It is observed that the double row bars at upstream are not regular in the downstream of the barbs. Figure 6.6 shows velocity field with 135° barb for simulation time of 1 hour and 5 hours. The general features such as circulation behind the barb and deflected flow at the tip of the barb are reproduced successfully. In this case, deflected flow at the tip of barb is found to be weaker than other two cases. Stream barbs at both side of barb are simulated and result are presented in figure 5.7 and 5.8. From those figure sit is observed that because of using barbs at both side the flow component converge around the both barb head and flow vector directed towards the centre of the channel.

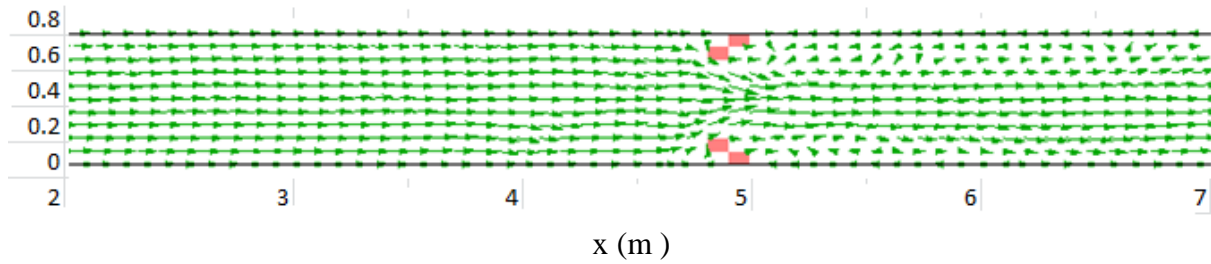


(a)



(b)

Figure 6.7 : Velocity field result with double barb installed at both sides at the channel after 1 hour simulation (a) by Hossain et al (2016) (b) present study (Case S_3C_5).



(b)

Figure 6.8 : Velocity field result with double barb installed at both sides at the channel (b) computed simulation after 5 hours (Case S_3C_5).

6.2.2 Bed Elevation Around the Structure

With sediment transport, the flow patterns were persuaded so that it can build the scour-hole and deposition. Generally, scours and deposition phenomena depend on the flow. Fig. 6.9 and 6.10 depict the simulation result with the depositional contour lines of pre-existing channel after 1 hour and 5 hours, respectively. In pre-existing channel double row bars are formed because of flow. After 5 hours these formation of barbs become more perceptible. Fig. 6.11 and Fig. 6.12 represent bed level contour results of the channel with a barb after 1 hour and 5 hours simulation, respectively. In these Figures, Figure (b) is the simulated results of present study, which is compared with the previous study by Hossain et al (2012) in Fig (a). Figure (b) is found to be well agreed with Figure (a) in both the cases. Figure 6.13 delineates the simulation results of a 90° barb with depositional contour lines after 1 hour and 5 hours, respectively. Fig 6.14 illustrates the simulated contour lines of 135° barb after 1 hour and 5 hours, respectively. 6.15 and 6.16 depict the simulation result of both side barbs with depositional contour lines after 1 hour and 5 hours, respectively. Deposition happens like sand bars along the bank-line at the upstream side of the structures. On the upstream side the

formation of bars changing trend from double row to alternate for long time simulation of the barb field. As a result of increased potential energy in the zone of upstream through backwater effects, the progression of the subcritical flow reaches in the bank region and controls erosion. Ultimately, it leads to deposition of sediments along the bank-line. Moreover, reduction of velocity gradient near bank through the subcritical backwater effect promotes sediment deposition upstream of the barb structure. Head scour occurs due to hydraulic jump and turbulence from flow mixing at the downstream side of barb especially near the barb. The scour depth occurs at the barb end and downstream of the structure because of energy redistribution away from the outer bank towards the center of the channel results in scour near the ends of the barbs (Matsuura and Townsend, 2004). The scour result is from contraction flow acceleration by local barb and deposited in the upward side of the barb.

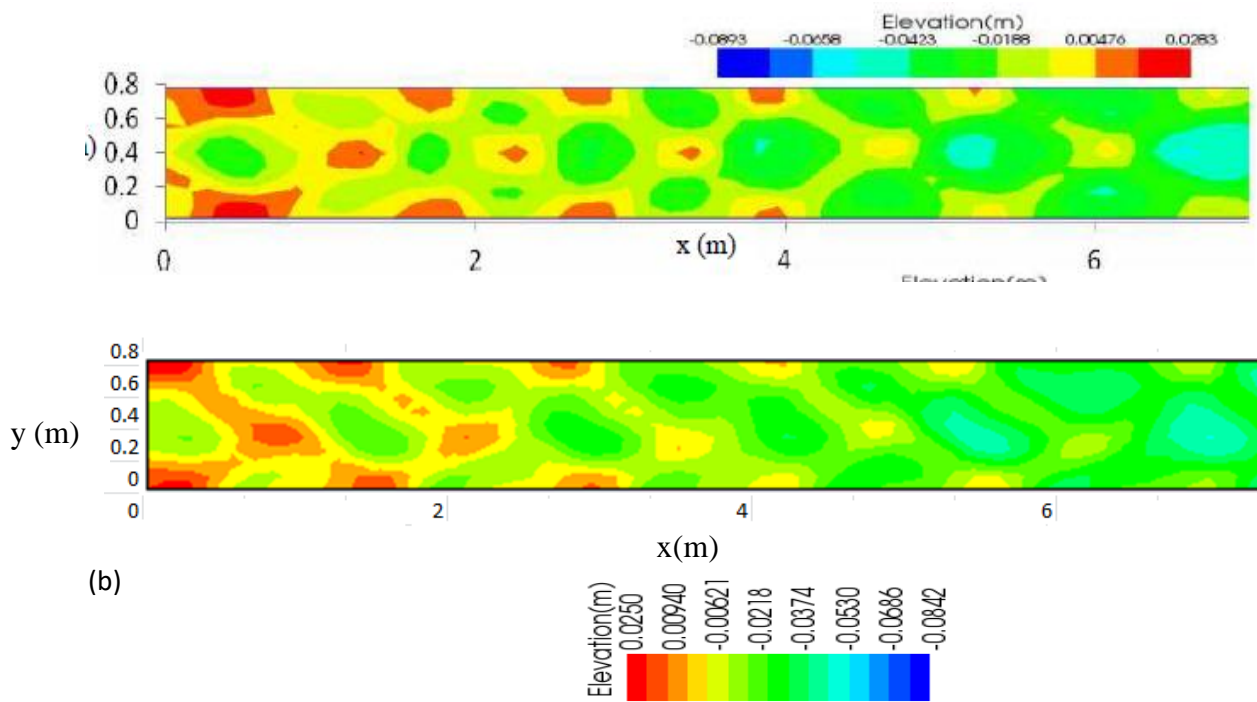


Figure 6.9 : Bed level contour result of the channel without any structure after 1 hour simulation (a) by Hossain et al (2012), (b) present study (S_3C_1).

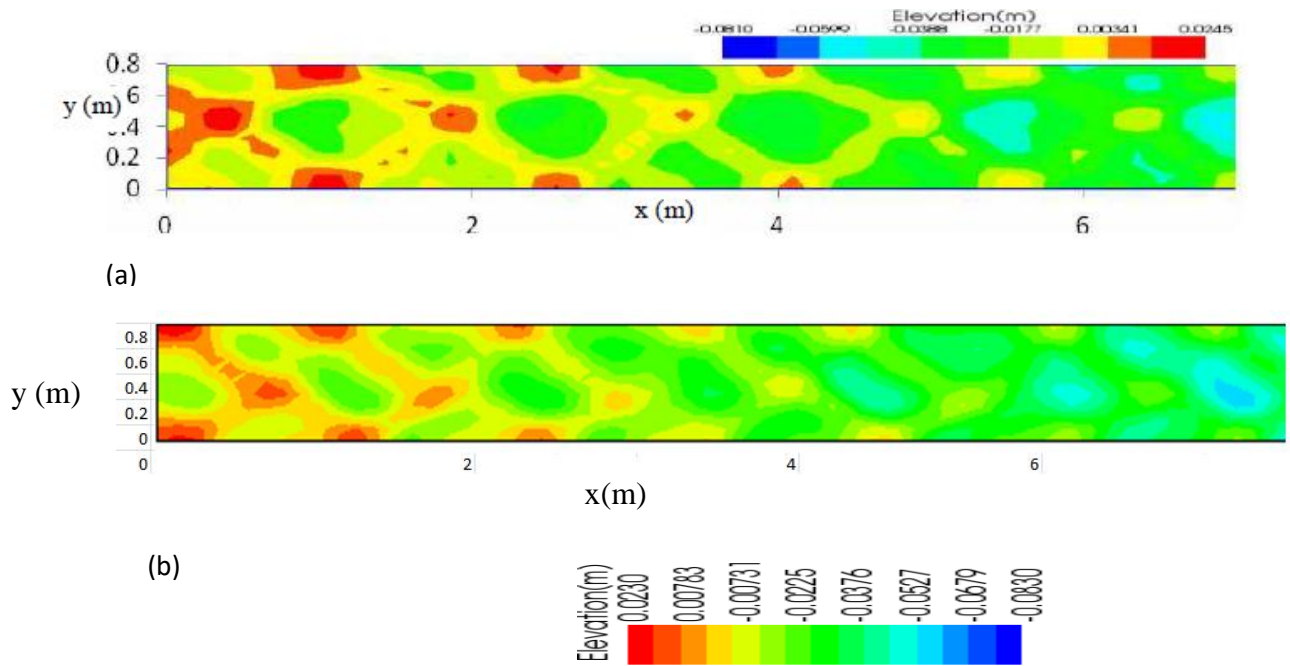


Figure 6.10 : Bed level contour result of the channel without any structure after 5 hour simulation (a) by Hossain et al (2012), (b) present study (Case S_3C_1).

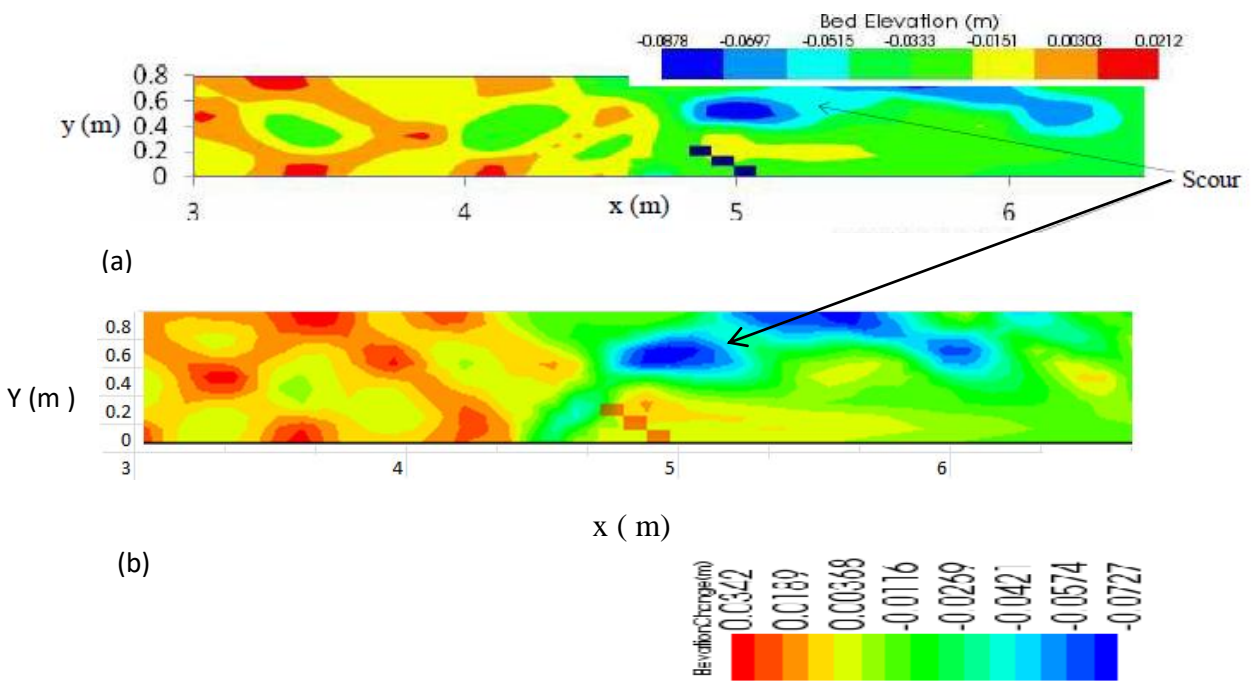


Figure 6.11: Bed level contour result of the channel with a barb installed at sidewall of the channel after 1 hour simulation (a) by Hossain et al (2012), (b) Present study (Case S_3C_2).

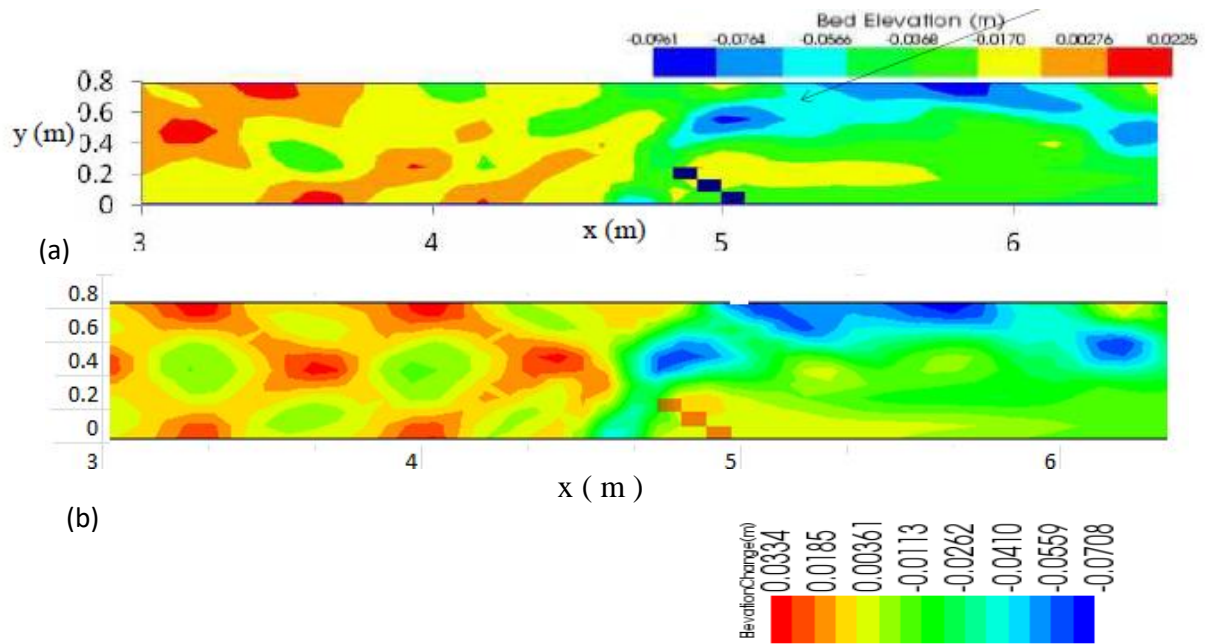


Figure 6.12 : Bed level contour result of the channel with a barb after 5 hour simulation (a) by Hossain et al (2012), (b) present study (Case S_3C_2)

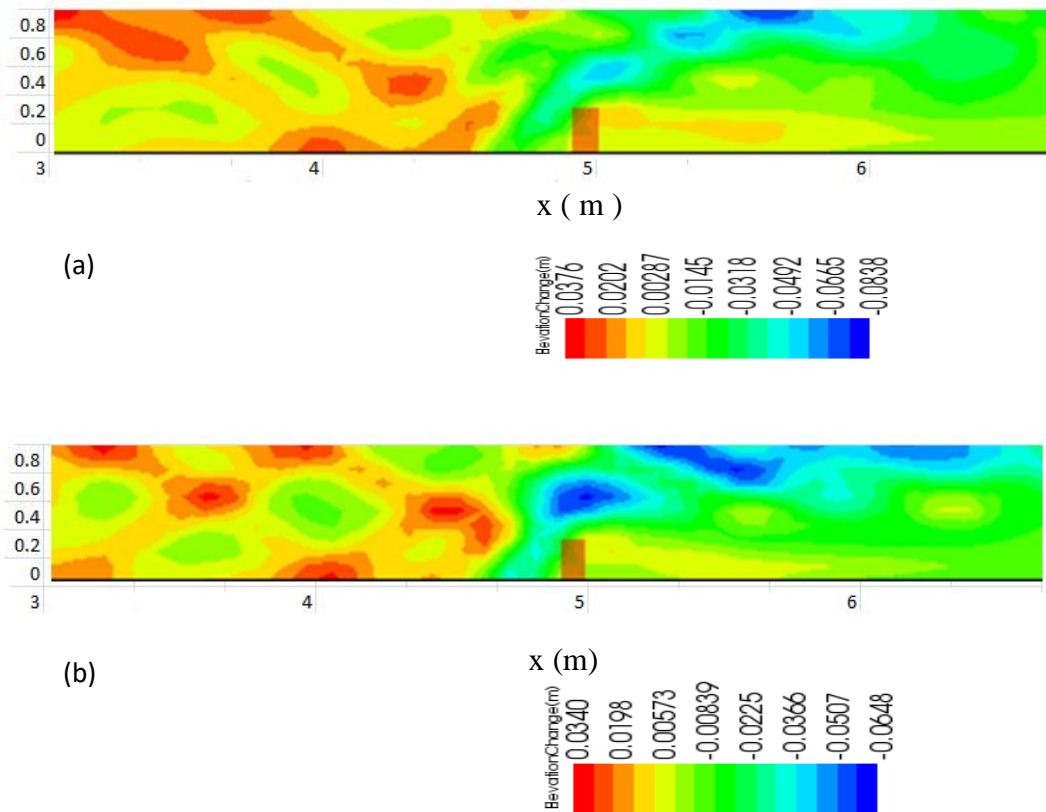


Figure 6.13: Bed level contour result of the channel with a 90° barb installed at one sidewall of the channel (a) after 1 hour (b) after 5 hour simulation (S_3C_3).

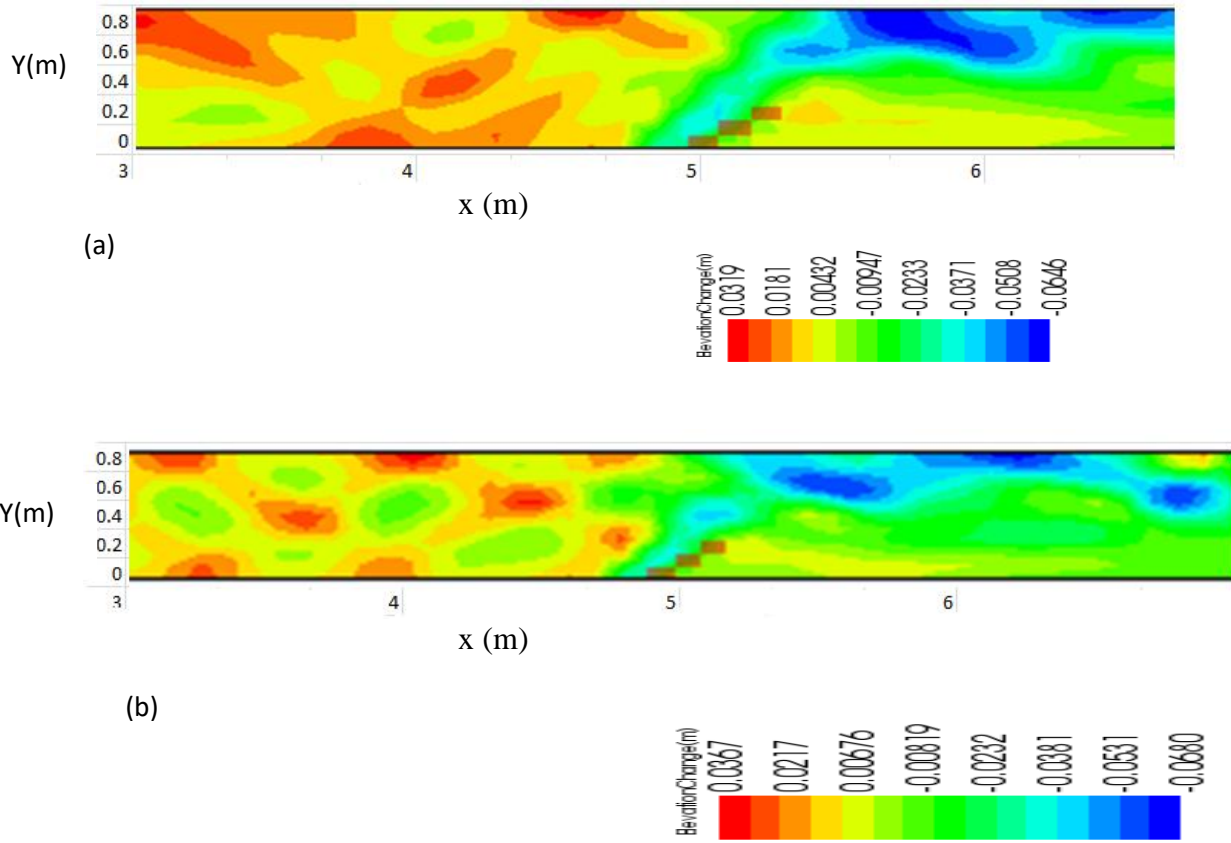


Fig 6.14: Bed level contour result of the channel with a 135° barb installed at one sidewall of the channel (a)after 1 hour simulation, (b) after 5 hour simulation (Case S₃C₄).

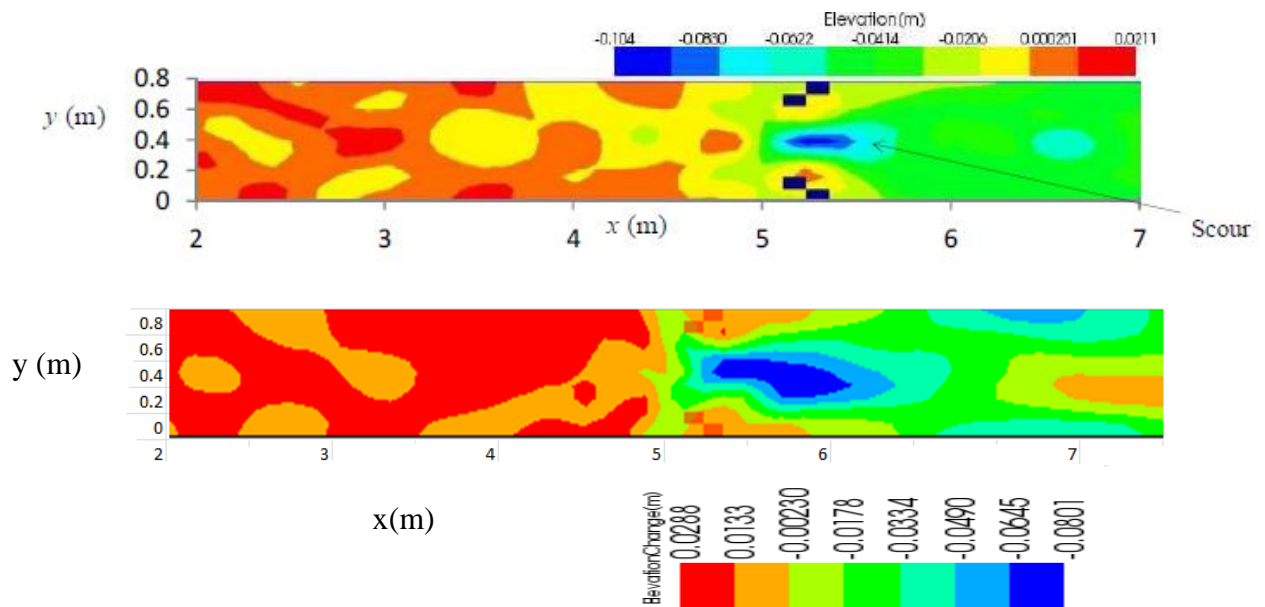
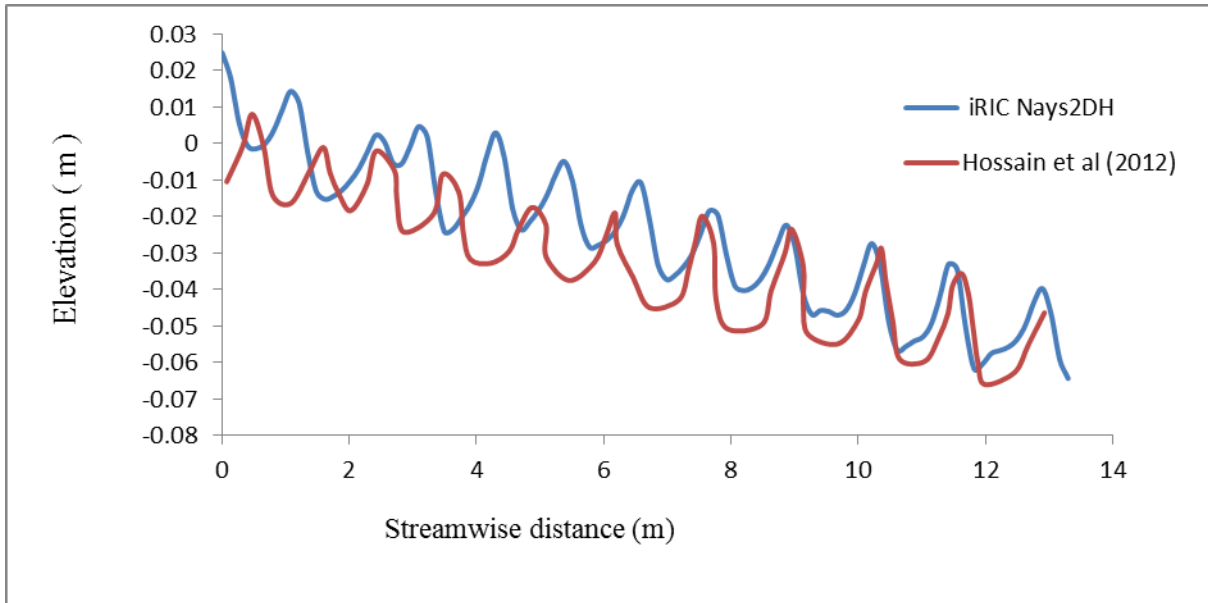
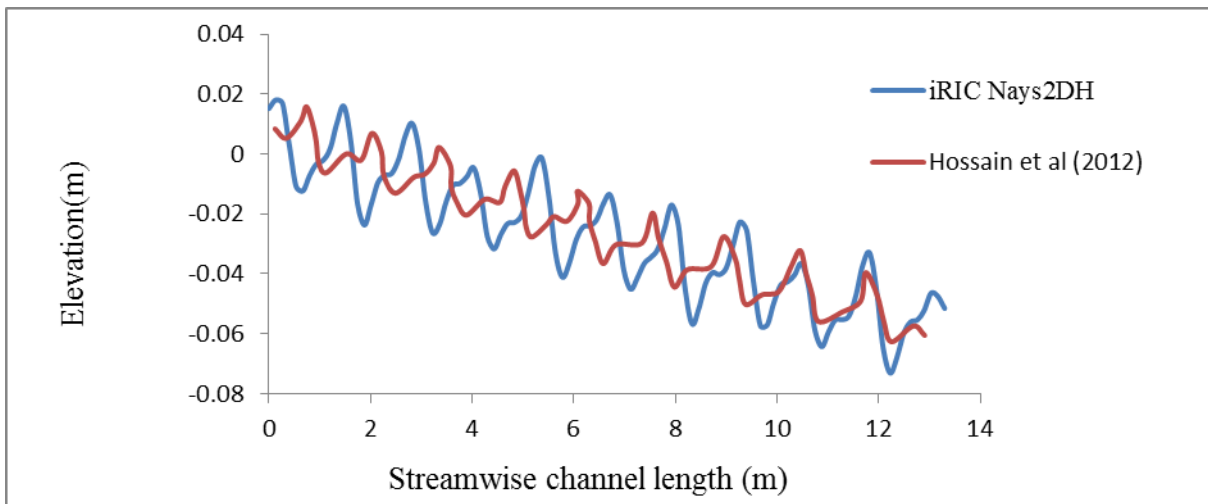


Figure 6.15: Bed level contour line after installed barb both side of the channel after 1 hour simulation (a) by Hossain et al (2016), (b) present study (S₃C₅).



(a)

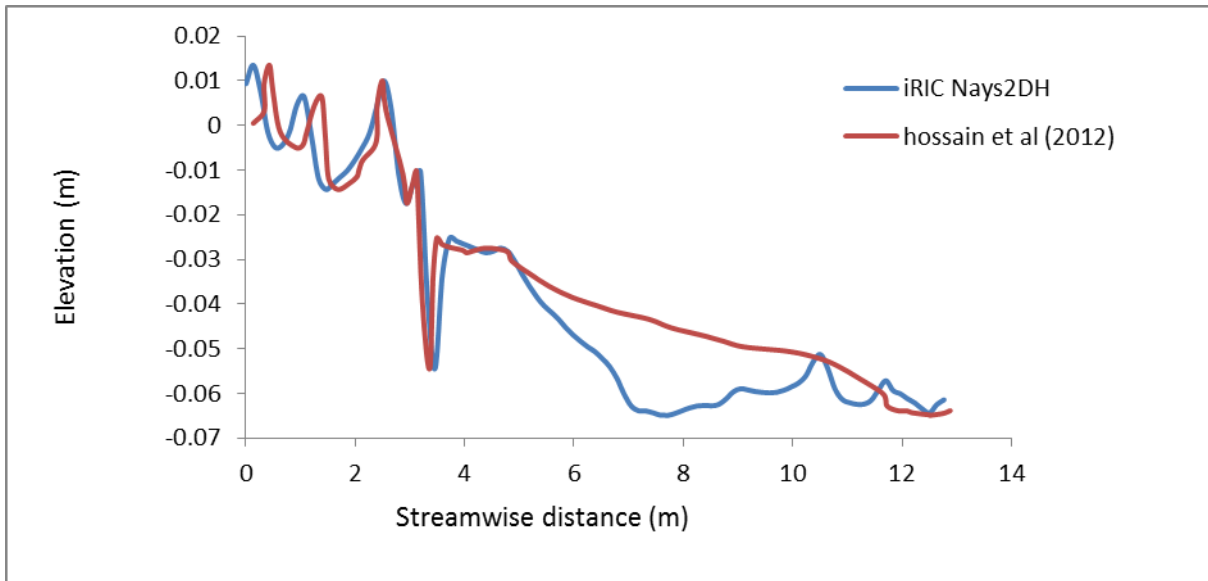


(b)

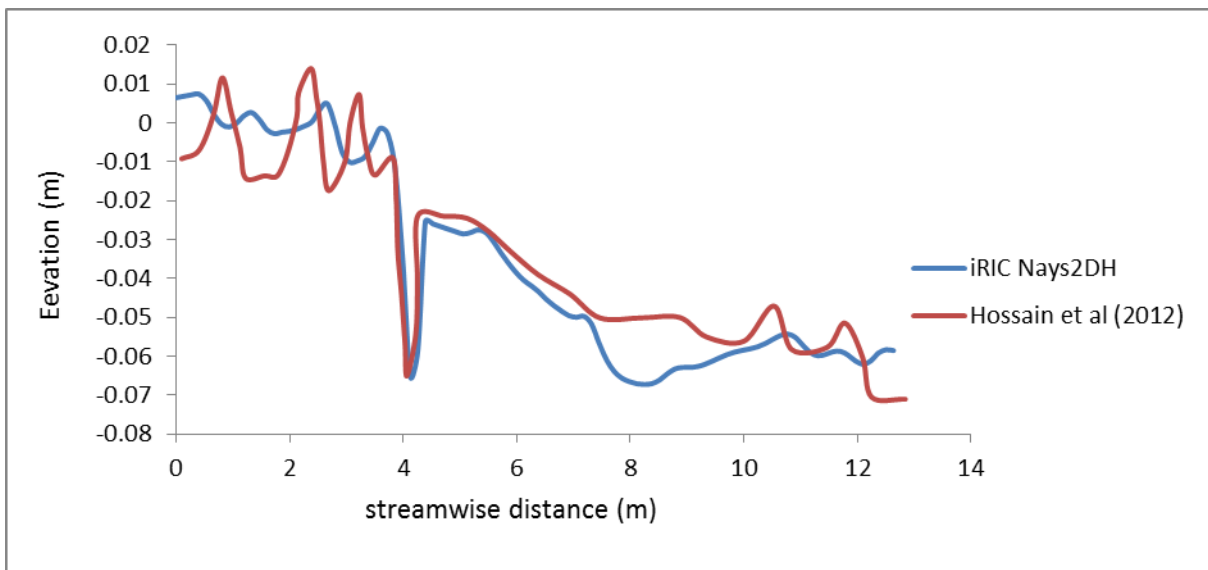
Figure 6.16: Evolution of bed profile & Comparison before installing barb (a) after 1 hour (b) after 5 hours (Case S_3C_1).

Fig. 6.16 (a) and 6.16 (b) show the comparison of bed elevation after 1 hour and 5 hours, respectively, in which present study has considerable agreement with previous numerical results presented by Hossain et al (2012). Similarly 6.17 (a) and 6.17 (b) depict bed elevation comparison with a 45° barb after 1 hour and 5 hours, respectively, where present study perfectly matched with previous numerical studied by Hossain et al (2012). The result shows clearly the applicability of barbs that reduced the erosion around the structure and increase the pool habitat near the thalweg, which can be useful for natural rivers training work. Figure 6.18(a) and 6.18 (b) represent bed deformation for 90° angled barb after 1 hour and 5 hours, respectively. Figure 6.19 (a) and 6.19 (b) show the evolution of bed profile for 135° barb.

Maximum scour is found for 45° angled groin which is .065 m and minimum scour is found in case of 135° angled groin which is 0.054 m.

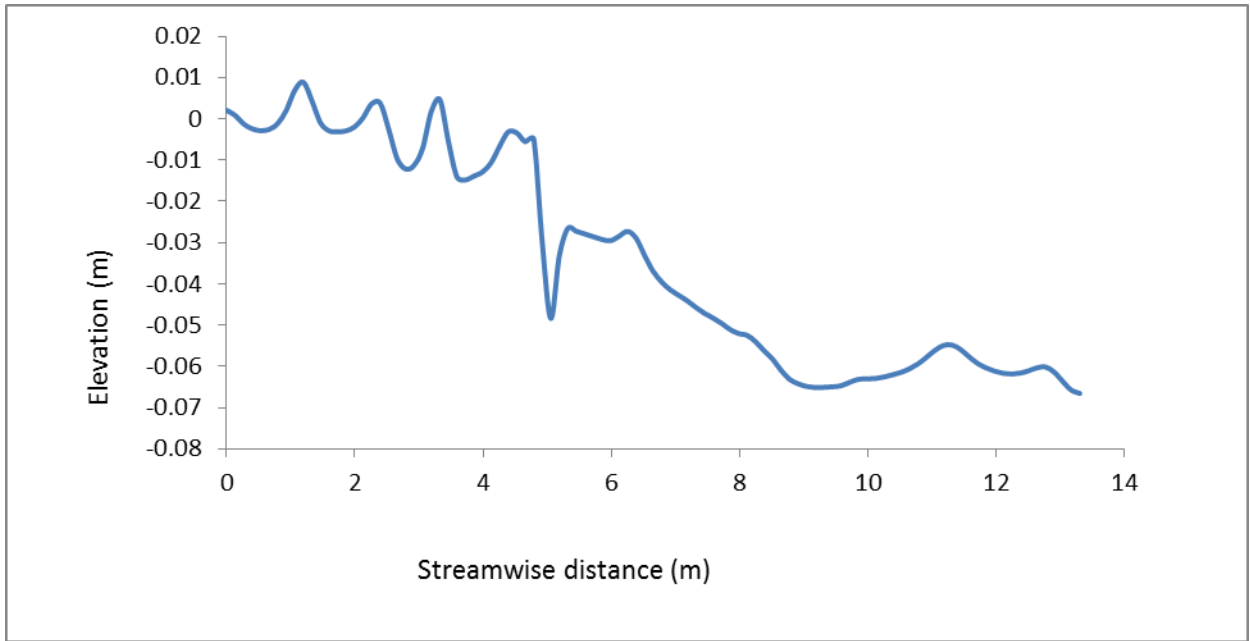


(a)

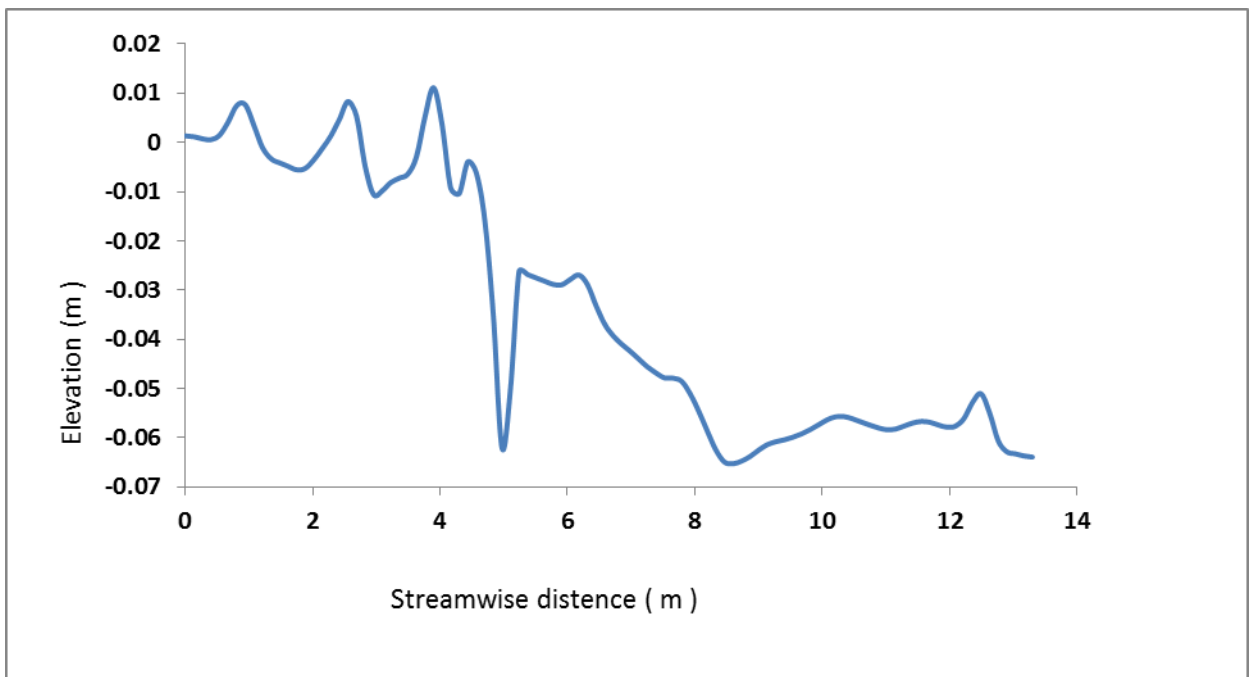


(b)

Figure 6.17: Evolution of bed profile and bed elevation with 45° barb (a) after 1 hour and (b) after 5 hours.

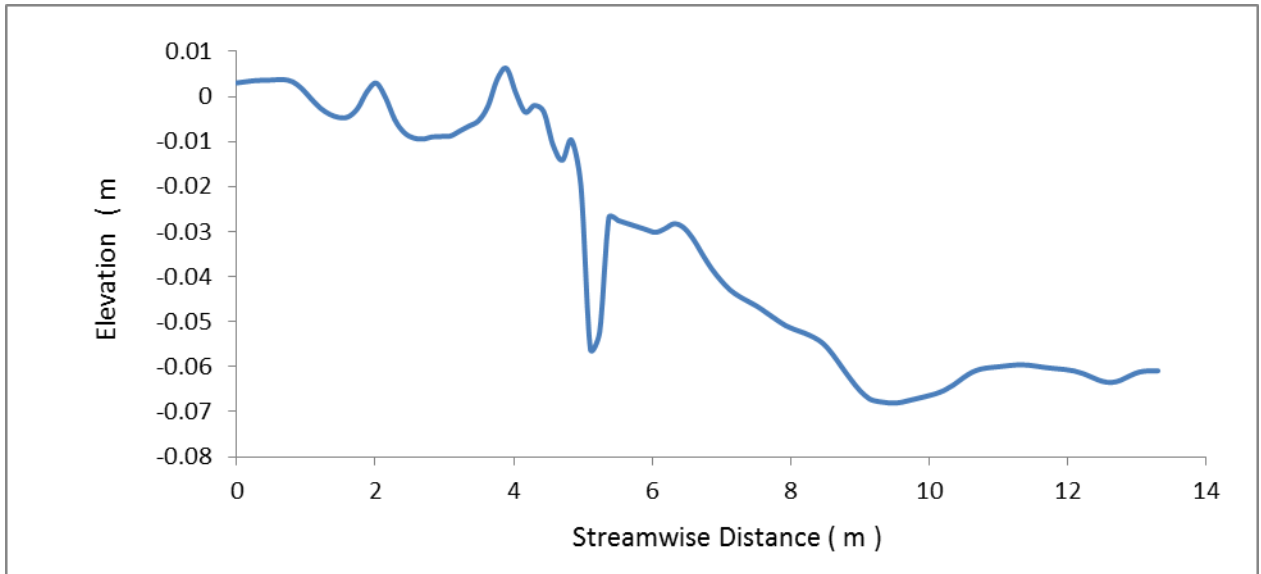


(a)

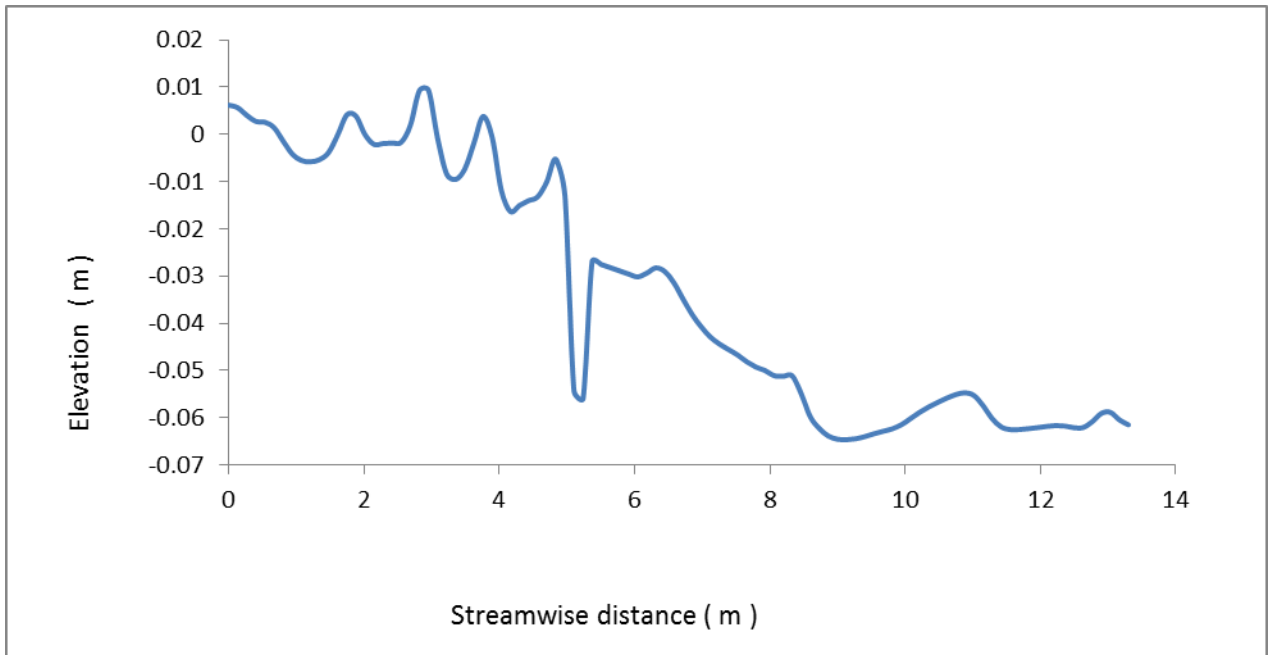


(b)

Figure 6.18: Evolution of bed profile represents bed elevation with 90° barb (a) after 1 hour (b) after 5 hours.

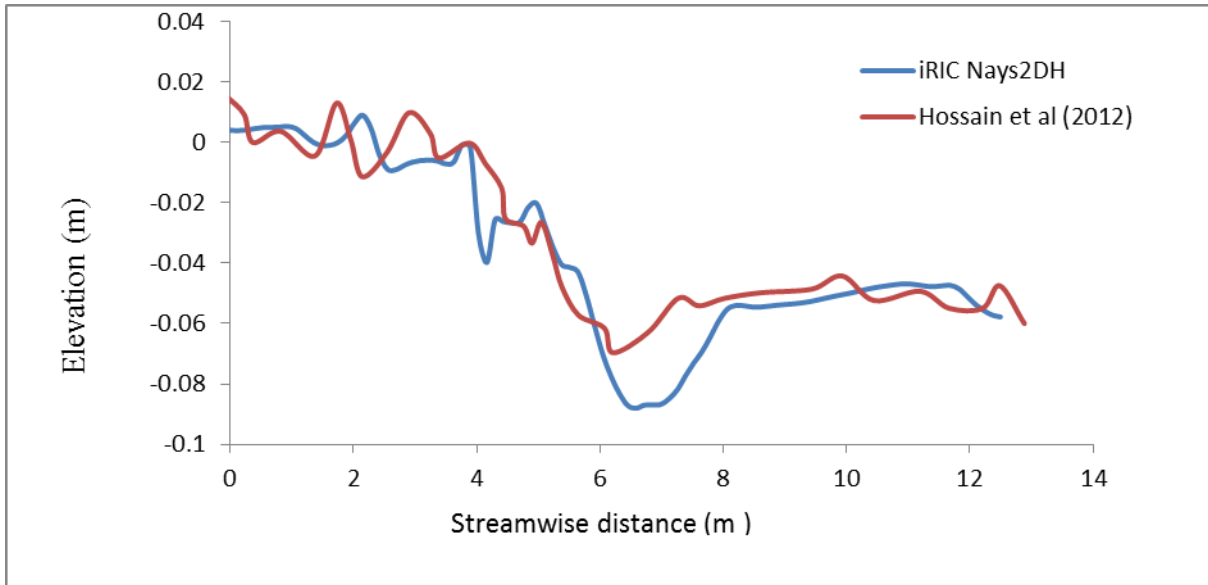


(a)



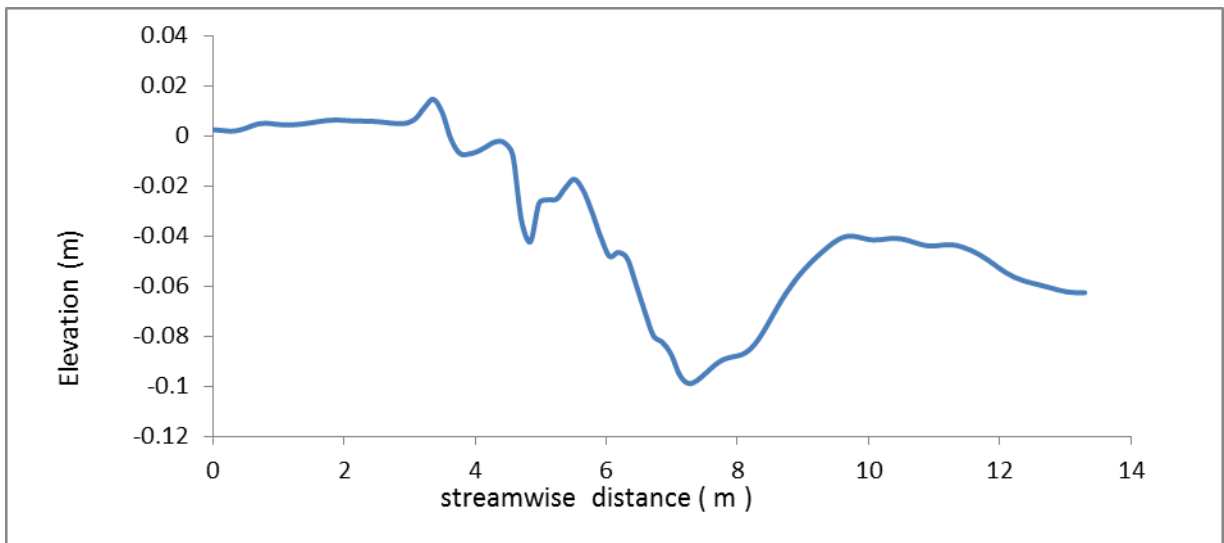
(b)

Figure 6.19 : Evolution of bed profile bed elevation with 135° (a) after 1 hour (b) after 5 hours.



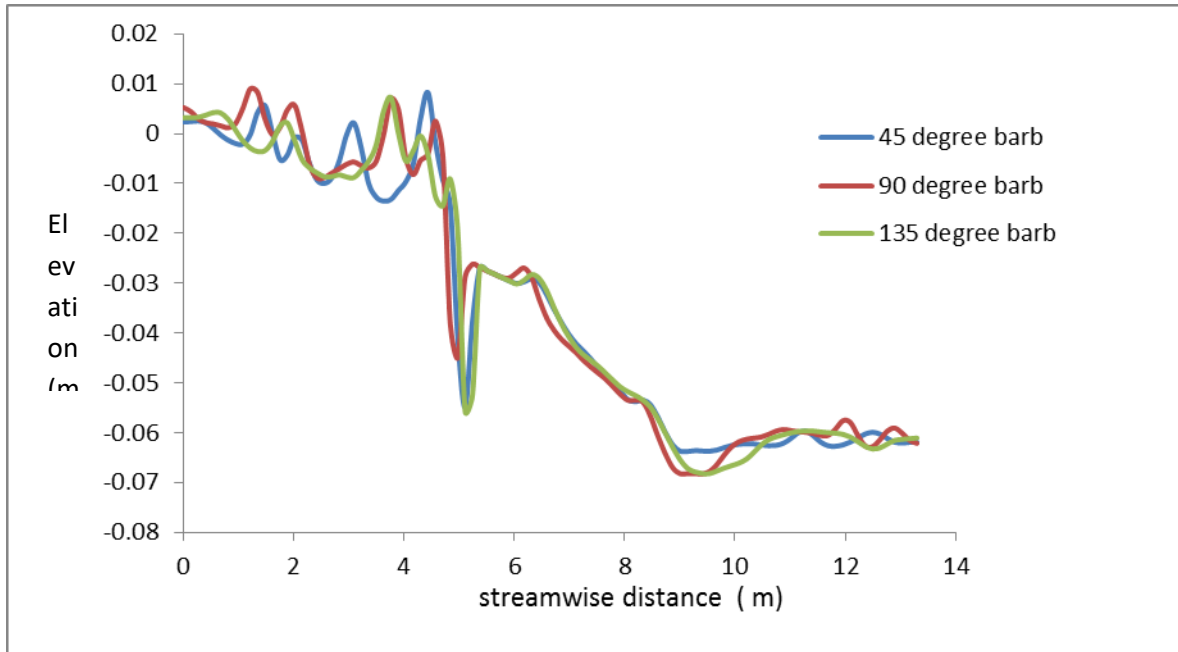
(a)

Figure 6.20: Evaluation of bed profile and comparison of Bed Elevation double at both side (a) after 1 hour.



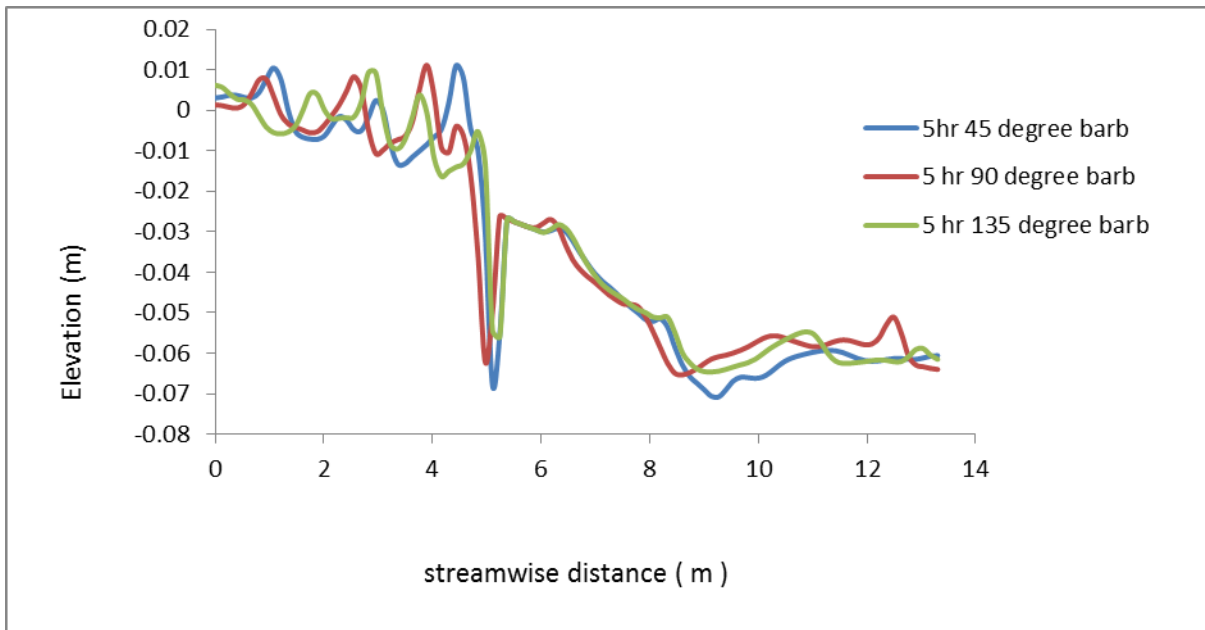
(b)

Figure 6.21: Evaluation Bed Elevation double barb at both sides of double barb (b) after 5 hours.



(a)

Figure 6.22 : Comparison of Bed Elevation of 45°, 90° and 135° barbs after 1 hour simulation.



(b)

Figure 6.23 : Comparison of Bed Elevation of 45° , 90° and 135° barbs (b) after 5 hour simulation.

After 5 hours, equilibrium scouring is attained and the maximum scour depth for 45°, 90° and 135° are found as 0.065 m, 0.062 m and 0.054m, respectively. After 1 hours, the equilibrium scour was not achieved. Therefore the result for maximum scour is not consistent with that of 5 hours result.

6.2.3 Flow Depth

For flow depth, comparisons were shown before barb installation and after barb installation. Based on numerical result, it can conclude that the maximum scour depth is increased at a decreased rate with the increasing in approaching flow depth. In case of shallow flow, scour depth increased with flow depth proportionally. In pre-existing channel, flow depth with scour hole varied from 2 cm to 10 cm and showed small variation in the entire simulation. When barb installed in the river left bank, maximum depth occurs near the thalweg due to turbulence flow. Expected flow depth is found to be occurred around the end of the barb and bed level scouring found to be varied from 2 cm to 14 cm.

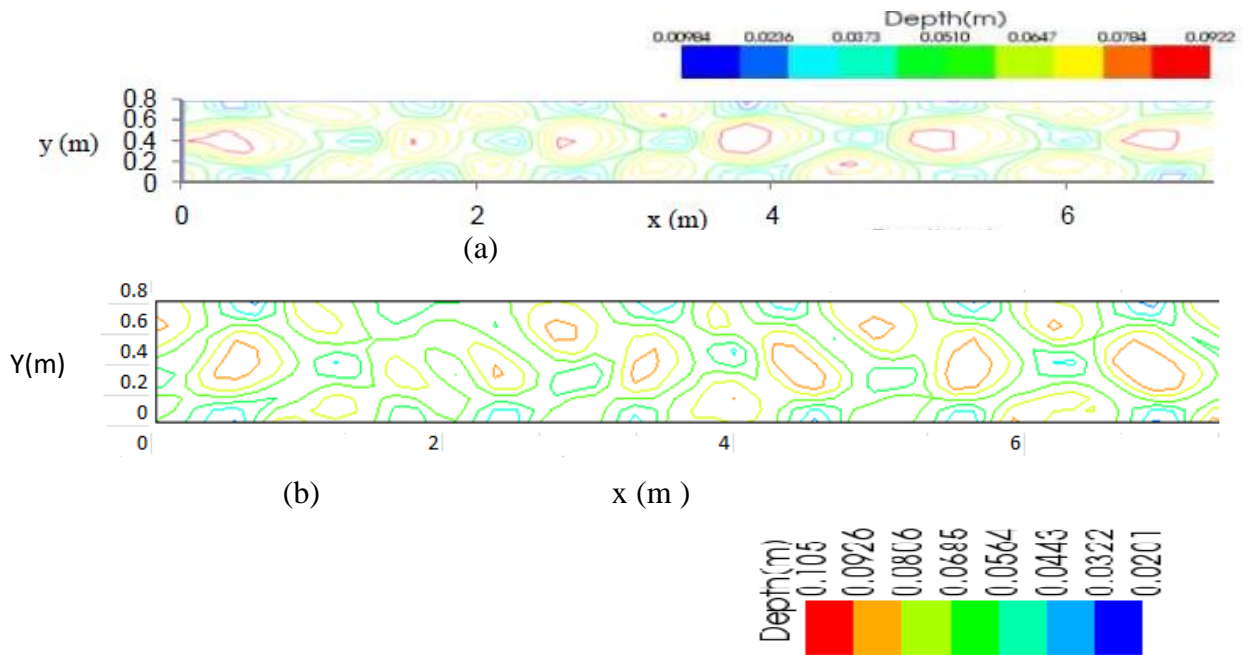


Figure 6.24: Water depth contour result of the channel without barb after 1 hour simulation (a) by Hossain et. al (2012), (b) present study (case S₃C₁).

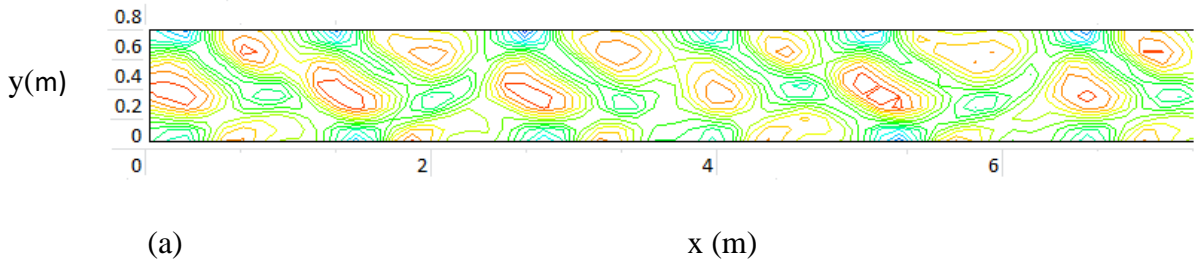


Figure 6.25: Water depth contour result of the channel with a barb installed at one sidewall of the channel after 5 hours simulation (S_3C_1).

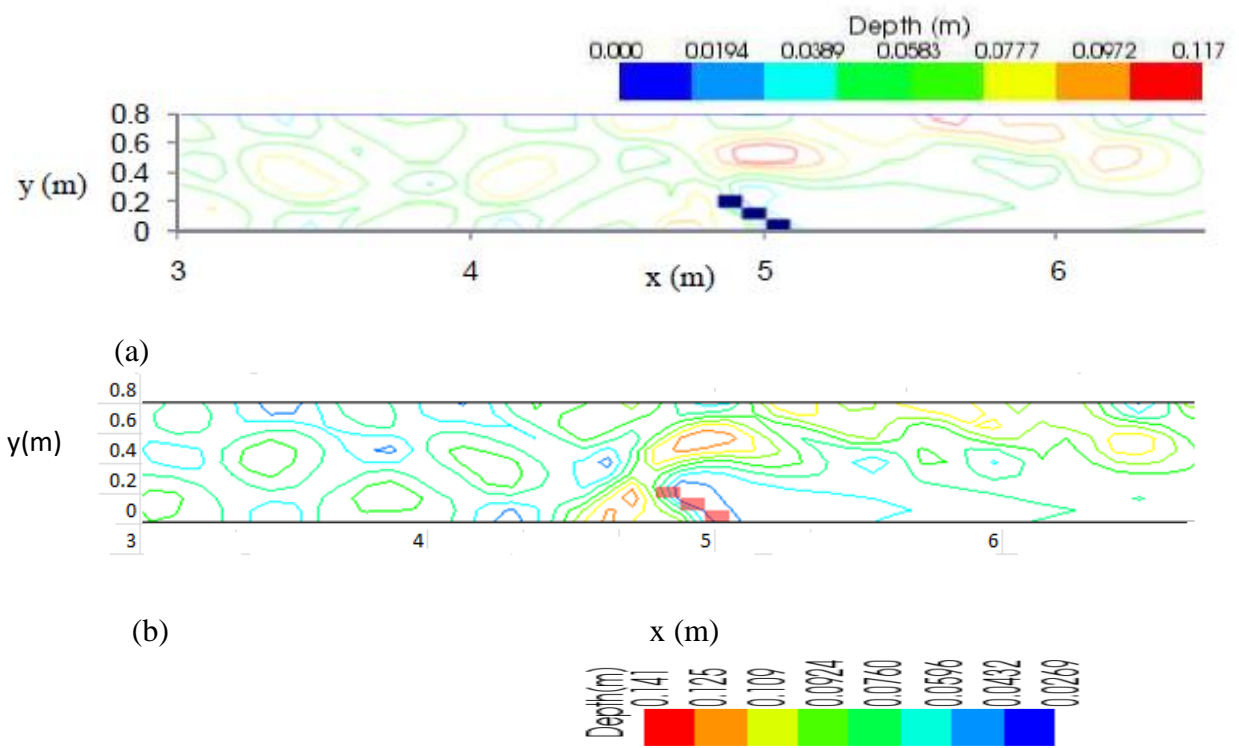


Figure 6.26: water depth contour result of the channel with a 45° barb installed at one sidewall of the channel after 1 hour simulation (a) by Hossain et al (2012), (b) present study (case S_3C_2).

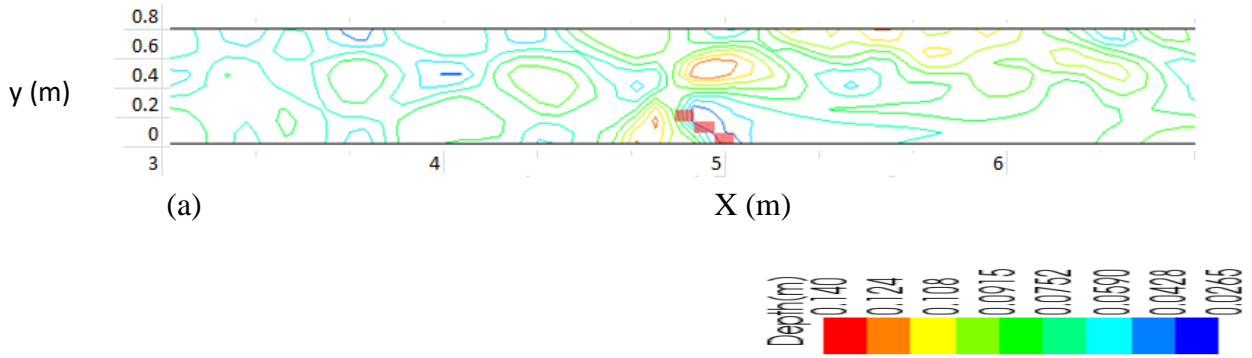


Figure 6.27: water depth contour result of the channel with a 45° barb installed at one sidewall of the channel after 5 hours computation (case S_3C_2).

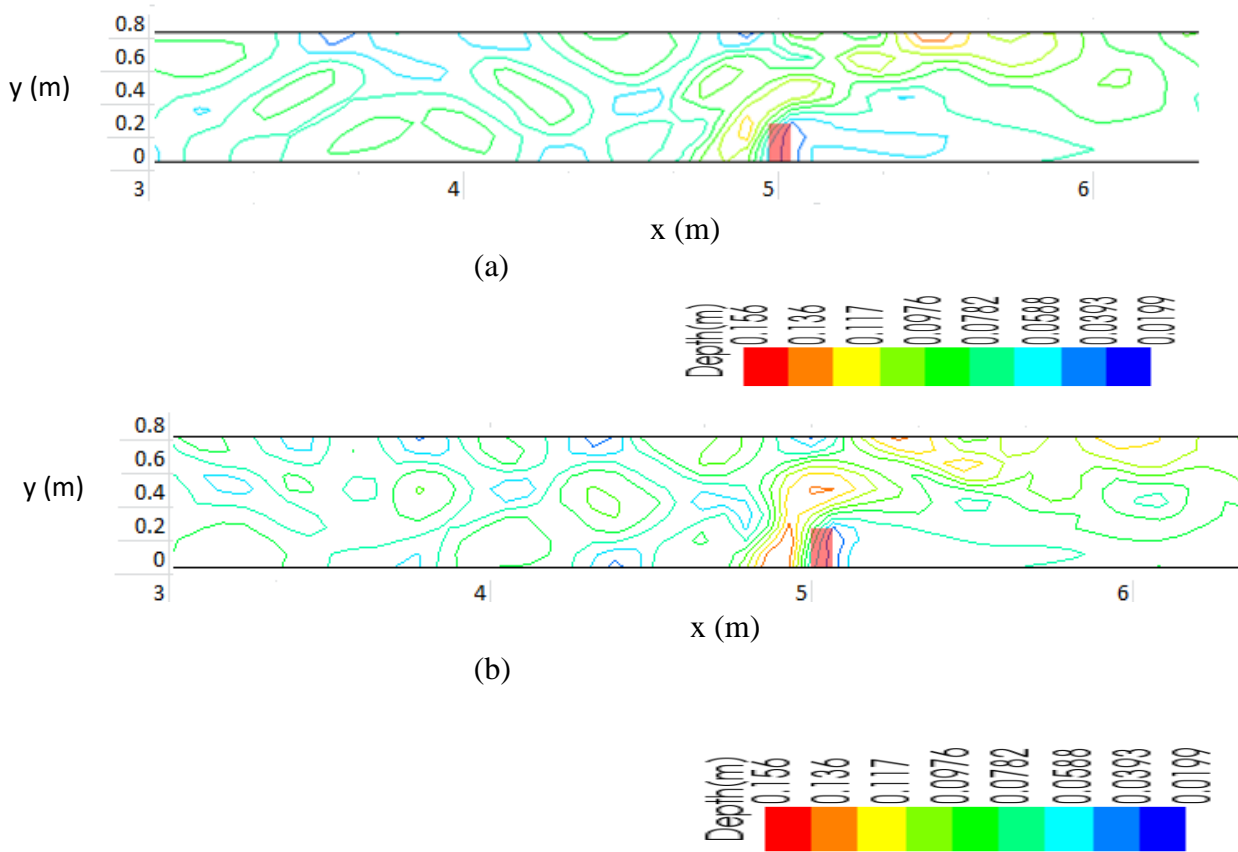


Figure 6.28 : water depth contour result of the channel with 90° barb installed at one sidewall of the channel (a) after 1 hours simulation, (b) after 5 hours simulation (S_3C_3).

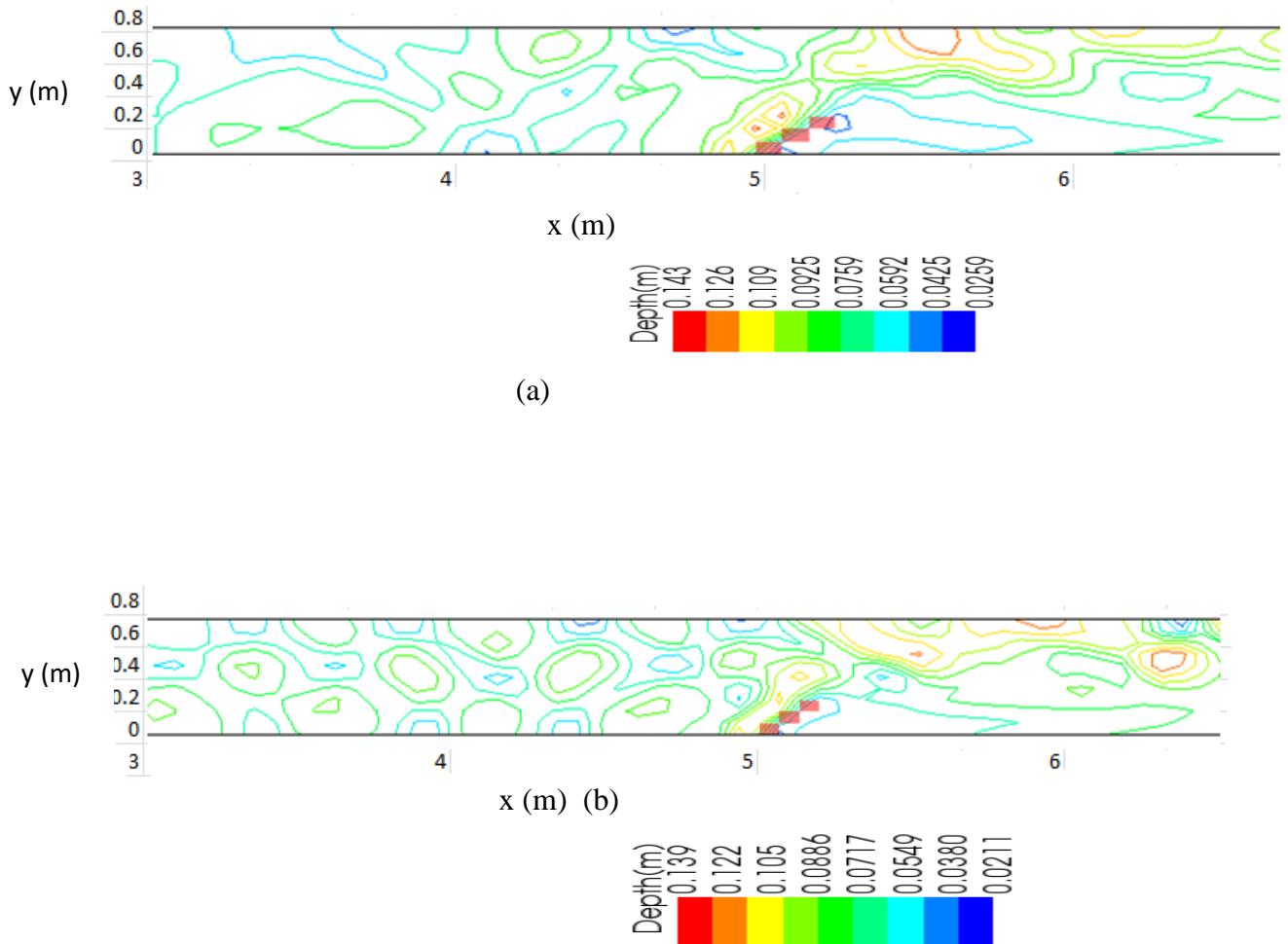


Figure 6.29 : water depth contour result of the channel with 135° barb installed at one sidewall of the channel after 5 hours computation (S₃C₄).

6.3 SIMULATION OF A CHANNEL WITH MULTIPLE SPUR DIKES

The purpose and function of spur dikes are same as barb and groin, different paper named them differently. Experimental study presented by karami et al (2014) is reproduced by iRIC Nays2DH to find out scouring phenomenon. They constructed a rectangular 14m long flume, with 1m width and 1 m depth in the laboratory of the amirkabir University of Technology. Three non-submerged, impermeable 25 cm length spur dikes were perpendicularly installed in channel. The first dike installed at a distance of 3.16 meters from the beginning of the channel and the distance of 3.16 meters from the beginning of the channel and the distance between them selected twice the length.

6.3.1 Flow Domain and Hydraulic parameters

For the numerical simulation, the channel length was chosen 5 meters. The computational mesh consist of 130 grids in longitudinal direction and 26 grids in lateral direction. The constant discharge for S₄C₁ is 0.035 m³/s and S₄C₂ is 0.046 m³/s. The depth of water is kept

constant at 15 cm. Manning's roughness co-efficient is considered 0.02 in this simulation. The simulation are performed in moveable bed condition with bottom slope, $S_0 = 0.001$. The finite differential methods of advection term are used as CIP method.

Pourshahbaz et al (2017) also used same experimental data of Karami et al (2014) to validate their model. In their model, they used k- ϵ turbulence model with the development of Renormalized group (RNG). According to them, changing the channel dimensions seem more reasonable and the length of channel should not be too short or too long to minimize computing costs.

Table 6.2 Hydraulic parameter for this numerical simulation

No. of test	L	B	Y	Q	U	Fr	d ₅₀
	m	m	m	m ³ /s	m/s	-	mm
S ₄ C ₁	5	1	0.15	0.035	0.233	0.19	0.91
S ₄ C ₂	5	1	0.15	0.046	0.307	0.25	0.91

Here, L = Length of the channel, B=width, Y= depth of water, Q=Discharge, U= velocity, Fr = Froude number and D₅₀ = Sediment size. S₄C₁ and S₄C₂ represents two different test with different hydraulic parameter.

6.3.2 Numerical Simulation Result

Numerical simulation by iRIC Nays2DH are performed for three perpendicular spur dikes with two different discharge. According to the result which are shown in Figures 6.30 and 6.31, maximum scour is 0.145m for Case S₄C₁ and 0.24 m for case S₄C₂. Figure 6.32 and 6.33 show the computed velocity vector for case S₄C₁ and S₄C₂, respectively. It is observed that spur dikes influenced the flow at downstream zone and created a mixing zone among the spur dikes. Figure 6.34 shows the definition sketch for different cross and longitudinal sections. Two longitudinal and two cross-sections are taken for whom the sectional bed elevation are compared in the following section.

Figure 6.35 shows the bed level changes comparison for case S₄C₁ with previous experimental results. Maximum scouring are found in Figure 6.35 (d). For case S₄C₁, the scour depth from first spur dike to third spur dikes are found as 0.123m, 0.005m and 0.005m, respectively. For case S₄C₂, the scour depth from first spur dike to third spur dikes are found as 0.16 m, 0.01m and 0.012m, respectively (Figure 6.36 (d)). From simulated results, it is observed that maximum scouring occurs at the first spur dike. The amount of scouring and sedimentation are also found to be depended on flow discharge. From the comparison of results between two cases, it can be concluded that higher discharge is responsible for higher scouring and sediment deposition. Table 6.3 shows the comparison of the scouring amount found by present study with previous studies of FLOW-3D simulation (pourshahbaz et al.,

2017) and previous experimental results (Karami et al., 2014). The results are found to be consistent with each other.

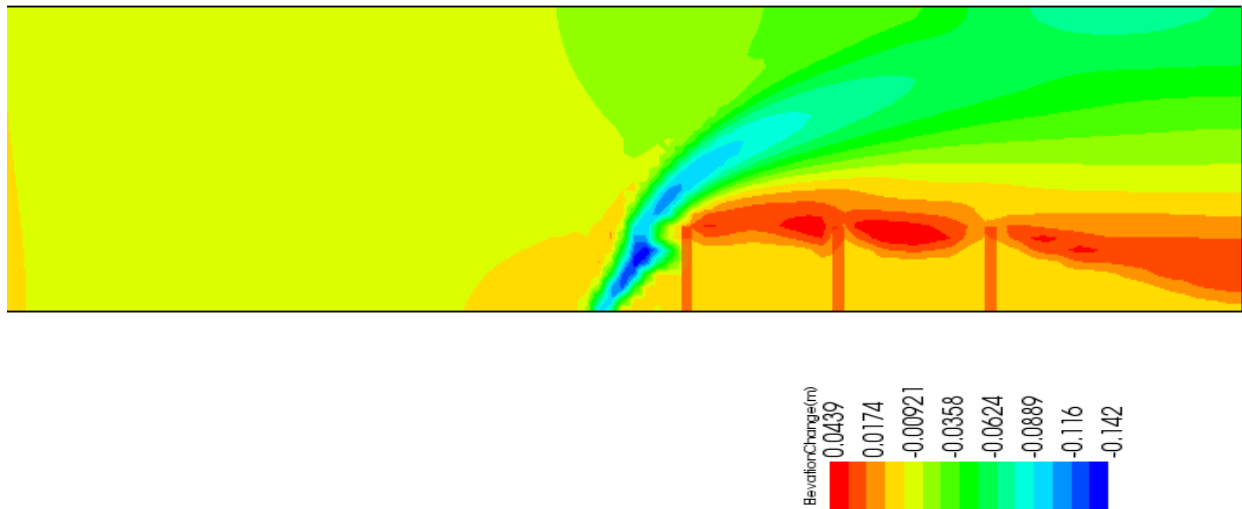


Figure 6.30 : Bed deformation contour line of case S₄C₁ simulated by iRIC Nays2DH

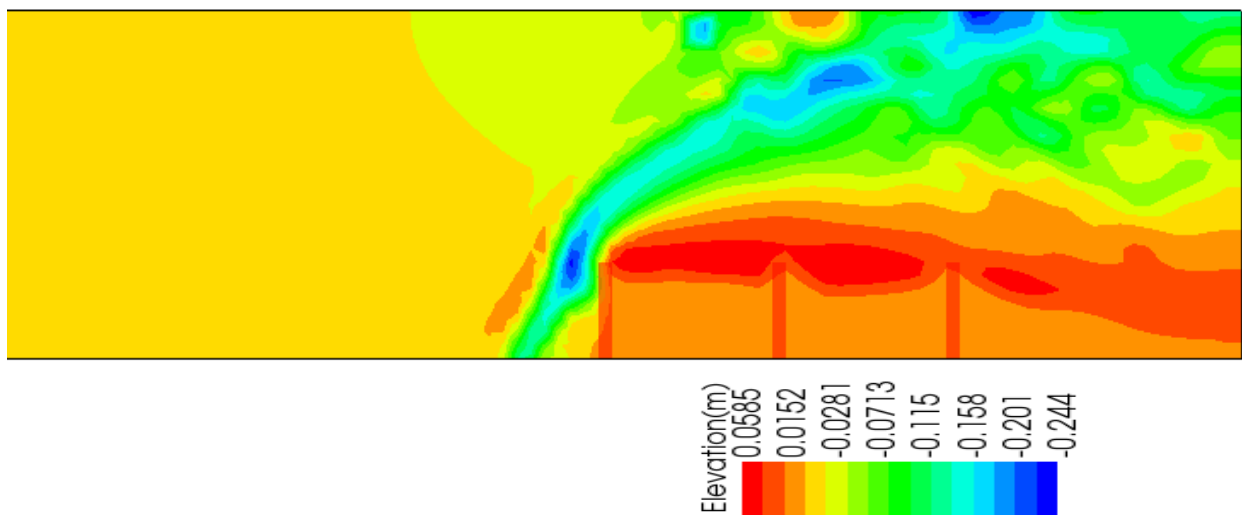


Figure 6.31 : Bed deformation contour line of case S₄C₂ simulated by iRIC Nays2DH.

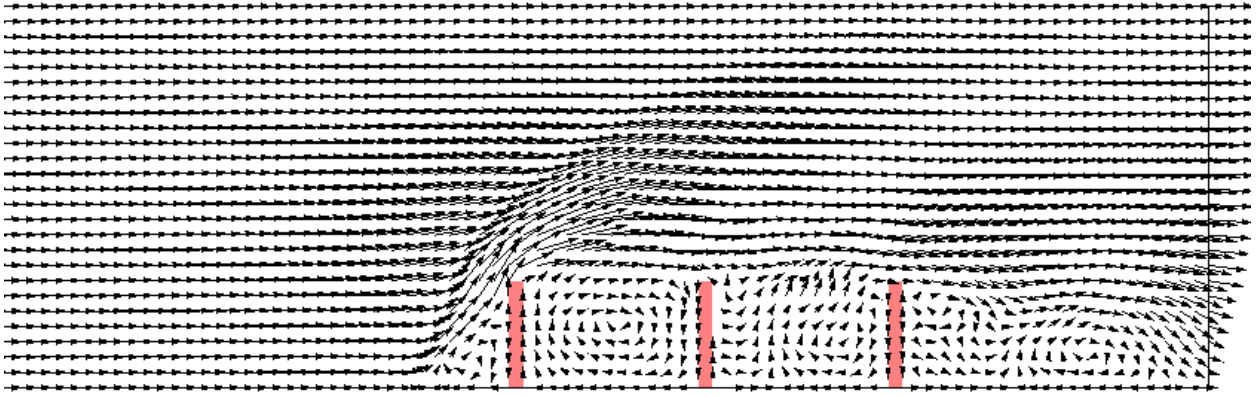


Figure 6.32: Computed velocity vector in case of case S_4C_1 developed by iRIC Nays2DH.



Figure 6.33 : Computed Velocity vector in case of S_4C_2 developed by iRIC Nays2DH.

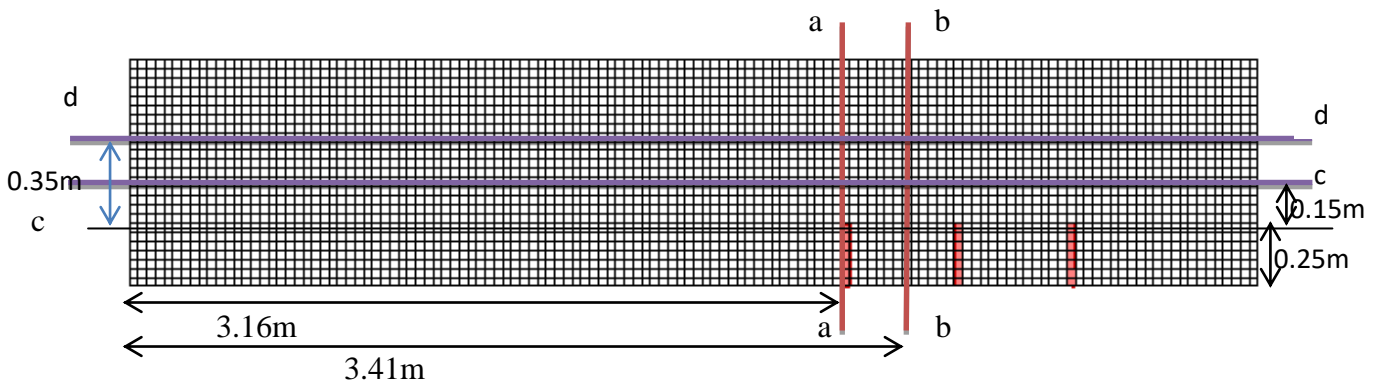
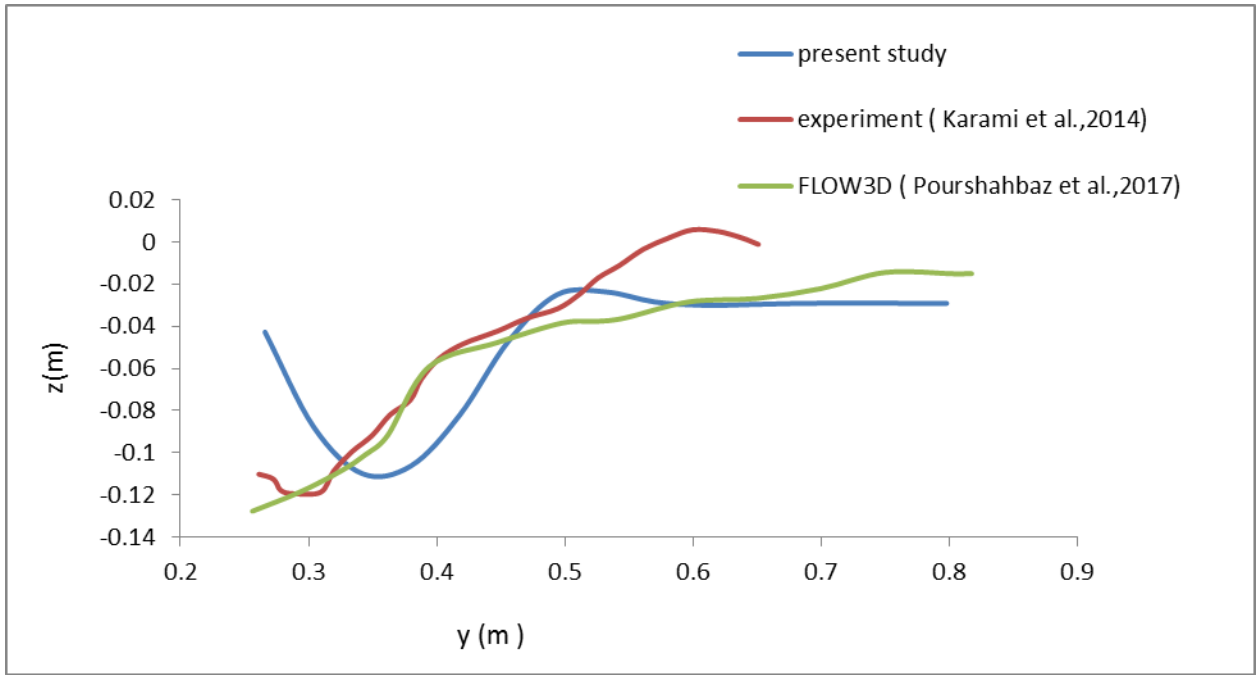
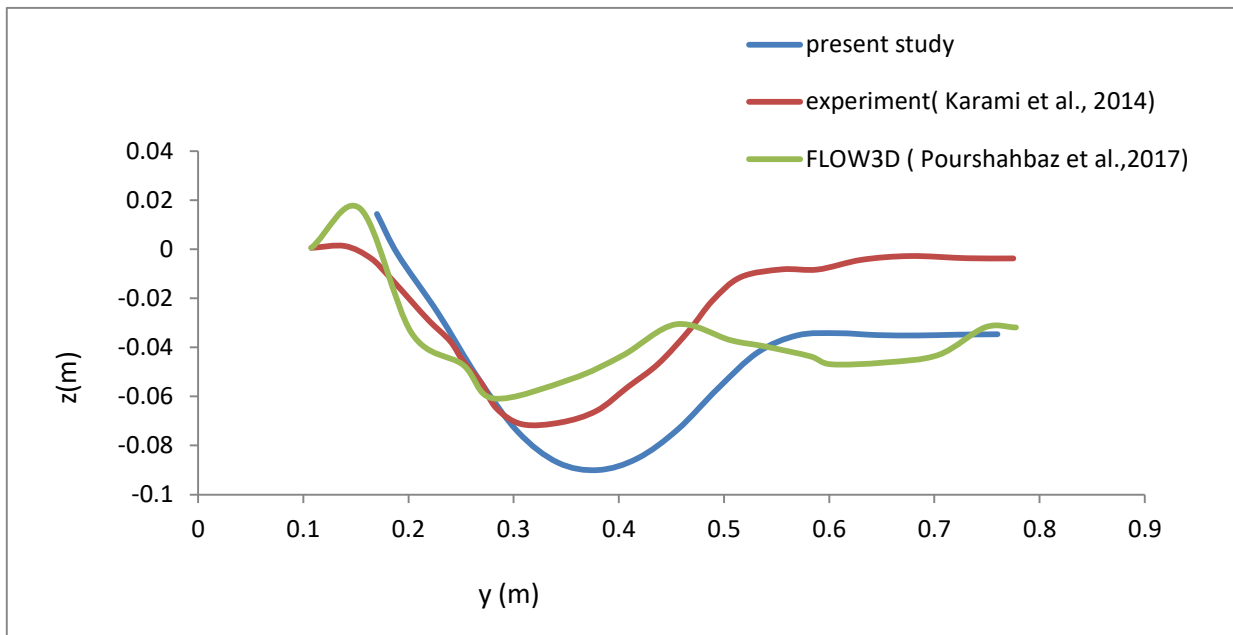


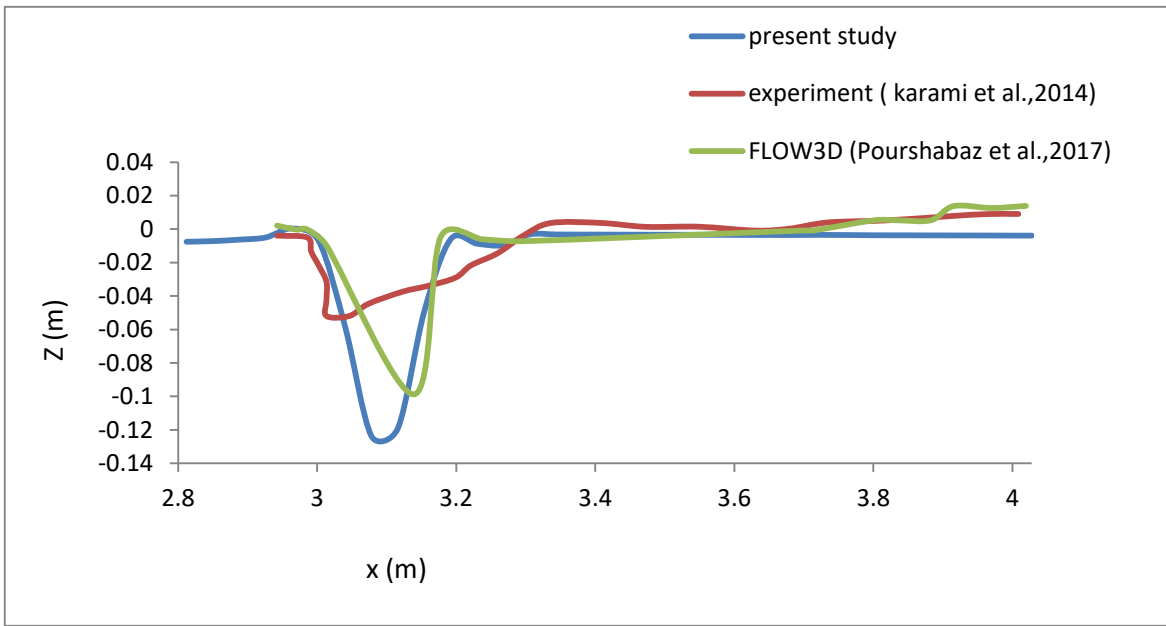
Figure 6.34 : Definition sketch for different cross and longitudinal sections.



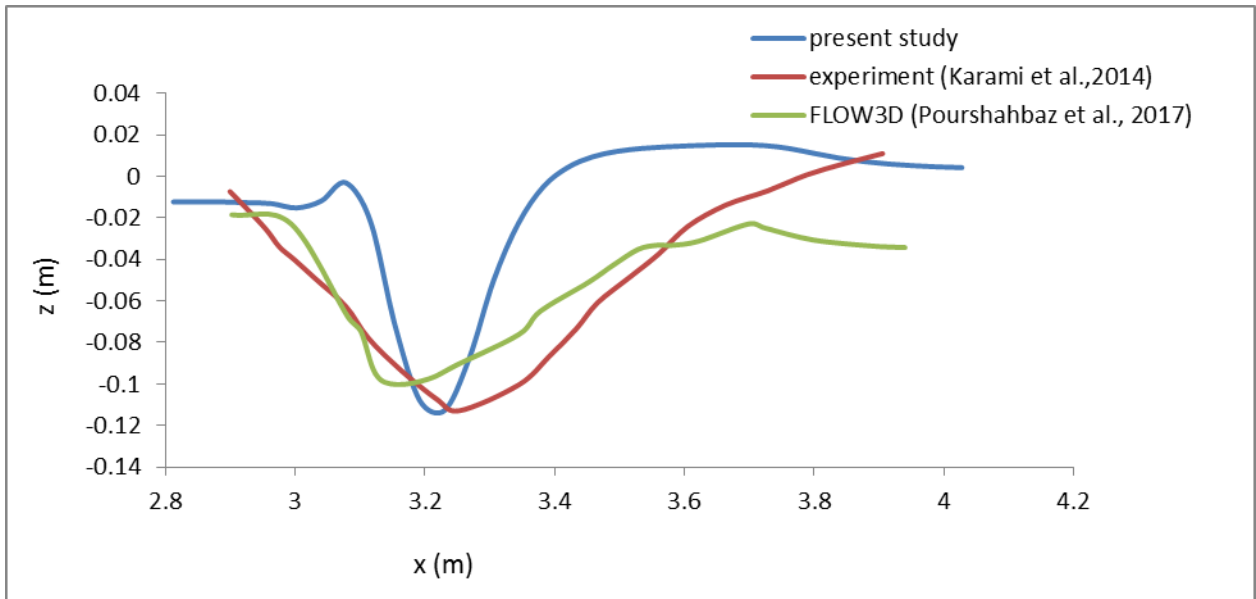
(a) Transverse bed profile at X= 3.16 (section a-a)



(b) Transverse bed profile at x =3.41(section b-b)

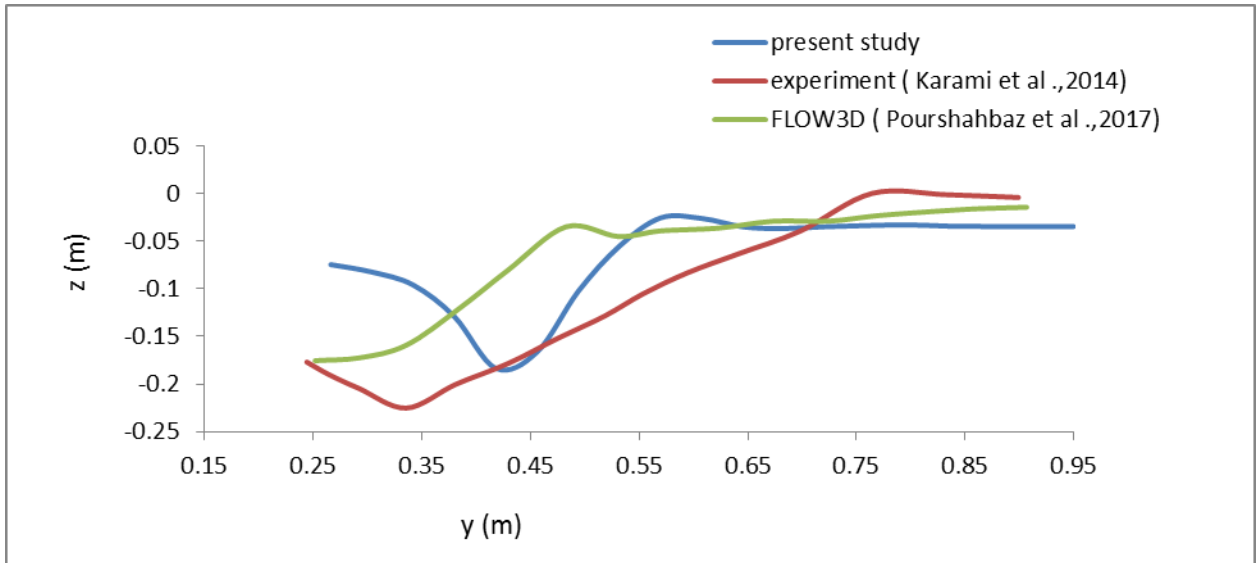


(c) Longitudinal bed profile at $y = 0.15$ (section c-c)

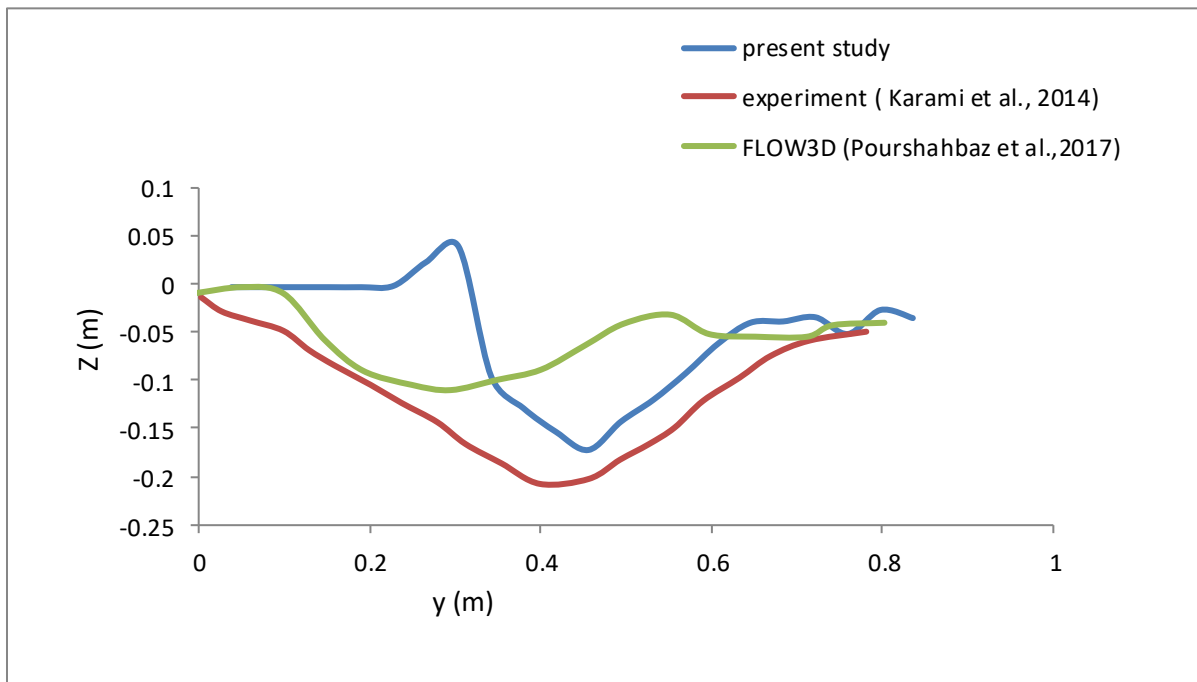


(d) Longitudinal bed profile at $y = 0.35$ (section d-d)

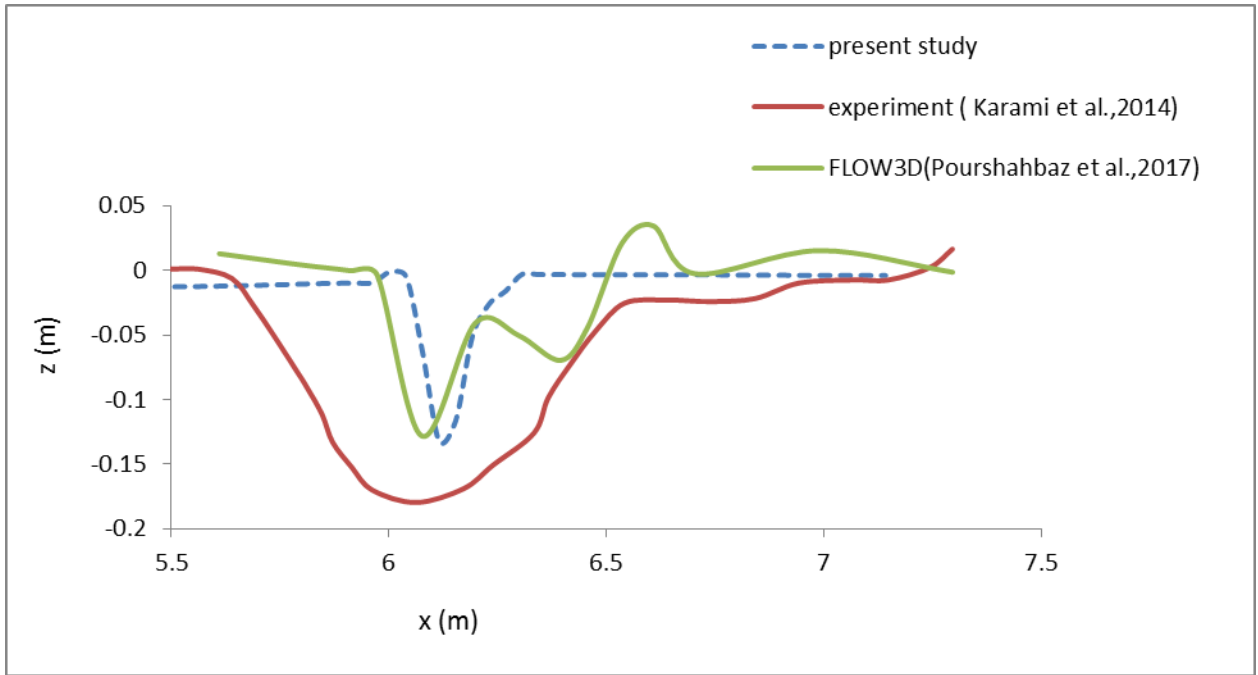
Figure 6.35: Bed changes comparison of case S_4C_1 results found by iRIC Nays2DH with FLOW-3D and previous experimental results.



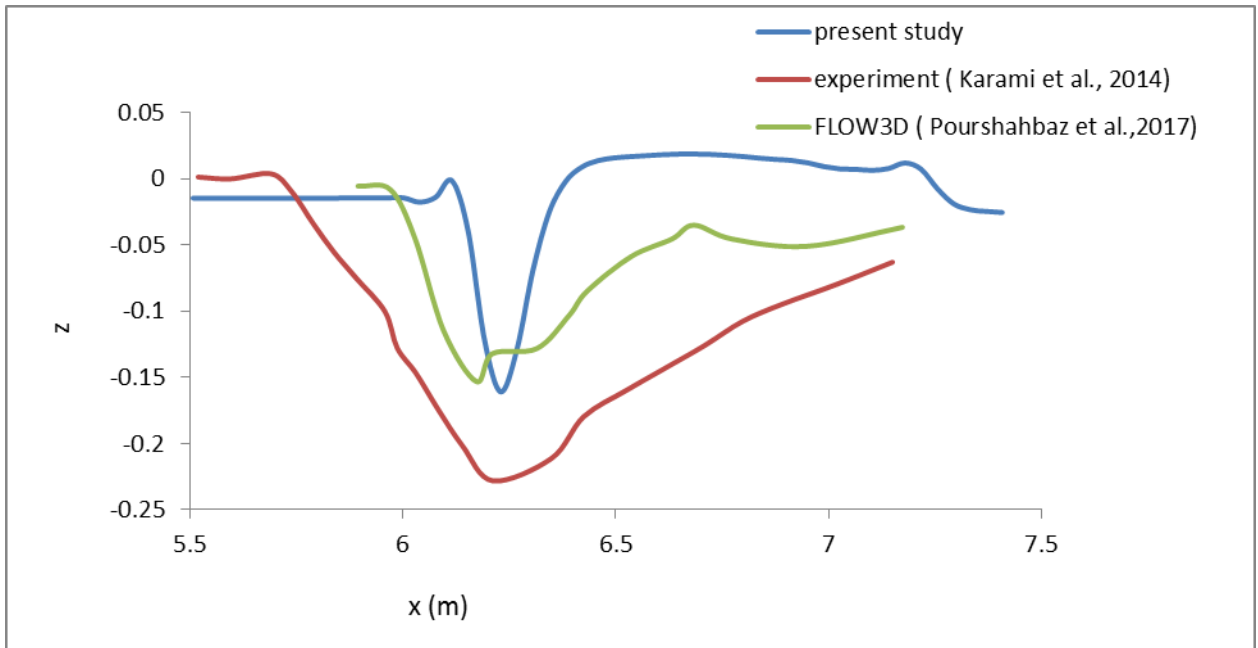
(a) Transverse bed profile at X = 3.16 (section a-a)



(b) Transverse bed profile at X = 3.41 (section b-b)



(c) Longitudinal bed profile at $y = 0.15$ (section c-c)



(d) Longitudinal bed profile at $y = 0.35$ (section d-d)

Figure 6.36 : Bed changes comparison of case S_4C_2 results found by iRIC Nays2DH with FLOW-3D and experimental results.

Table 6.3 : Comparison of the scouring amount in iRIC Nays2DH results with Flow-3D (Pourshahbaz et al., 2017) and experimental results (Karami et al., 2014).

Case		ds1	ds2	ds3
S ₄ C ₁	Experimental	0.156	0	0.026
	FLOW-3D	0.123	0.005	0.023
	iRIC Nays2DH	0.123	0.005	0.005
S ₄ C ₂	Experimental	0.225	0.029	0.072
	Flow-3D	0.178	0.0177	0.0321
	iRIC Nays2DH	0.16	0.01	0.012

Chapter 7

CONCLUSION AND RECOMENDATION

7.1 INTRODUCTION

The study employed two dimensional simulation model Nays2DH to investigate the characteristics of flow and bed change around a groin like structures. The simulation is performed for single and multiple groins with different discharges. To examine the performance of software with strong secondary current, open channel flow with 180° sharply and mildly curved channels are also simulated.

7.2 Conclusions

For all the channel bends, the simulation predicts the flow field accurately at the inlet straight portion, at bend as well as at the outlet straight portion of the channel. The simulated flow field and water surface profile for 180° bends obtained from the two-dimensional model showed good comparison with experiments. Therefore, iRIC Nays2D is suitable to deal a flow field which is highly affected by secondary current.

This simulation has provided us with detailed information regarding the flow pattern, the velocity and bed shear stress profiles around a groin. This adds to the effort of work done by others on different types of groins. The flow features around a groin is reproduced successfully. The flow field is found to be divided into four distinct regions: (i) the uniform flow at upstream end, (ii) big circulation of low velocity zone, (iii) a small low velocity zone near the foot at the upstream of groin and (iv) high velocity zone opposite to the circulation zone created due to the deflected flow. The high velocity zone is found to be decayed toward downstream and the low velocity in circulating zone is found to be regained. The computed velocity and bed shear stress profiles of presents study are compared among different cases.

From the simulation, it is observed that the peak of velocity and bed shear stress is found maximum at the position of head of groin when lateral distance $y/l = 1$, where l is the groin length. The position of maximum velocity and bed shear stress is found to be shifted towards downstream with increasing y/l . The maximum velocity and bed shear stress for 135° groin are found lower than the other two cases for all the section of y/l . W/U_0 and τ/τ_0 for 90° groin are found maximum for $y/l \leq 2$, and for $y/l \geq 2$, the velocity and bed shear stress are maximum for 45° angled groin. The downstream circulation zone is found to be larger for 45° groin compared to 90° groin; similarly, the circulation zone for 90° groin is found larger compared to 135° groin. In order to examine the present model, the computed results are compared with previous numerical and experimental results. The comparison are found to be well agreed with each other.

A barb is installed with 45° angled to the flow direction similar to Hossain et al (2012) in a straight channel and simulated for 1 hour and 5 hours. Same hydraulic data is also used for 90° as well as 135° angled barb and also simulated for 5 hours. After 5 hours simulation, the flow is found to be reached in equilibrium scouring. In that case maximum scouring has found for 45° angled groin and minimum scouring has found for 135° angled groin. After barb installation, due to the flow separation at barb head, return current developed at the upstream side induced zone of subcritical flow along the stream bank. It influenced the flow at downstream side creates a mixing zone just behind the structure. At the downstream side of barb especially near the barb head scour occurred due to hydraulic jump and turbulence from flow mixing. In pre-existing channel flow depth with scour hole varied from 1 cm to 8cm. As expected flow depth was present around the end of the barb and the water depth including scour hole varied between 2 cm to 12 cm. Simulation results showed that the installed barb successfully reduced the flow velocity along the bank.

The numerical simulation is also performed for three perpendicular groin in a straight channel. Two different test S₄C₁ and S₄C₂ were run for 8 hours with 0.035 m³/s and 0.046 m³/s, respectively. Maximum scouring occurred at first spur dike than the other two spur dikes. Considerable agreements are found between computed and previous experimental results. It is found that the amount of scouring and sedimentation are also depend on flow discharge. From the simulation results, it can be concluded that higher discharge is responsible for higher scouring and sediment deposition.

7.2 RECOMMENDATIONS FOR FURTHER STUDY

Following recommendation can be made for further research on this topic.

- Since the flow near a groin is highly three-dimensional, it is recommended that for field, a 3D numerical model needs to be employed.
- The study can be extended to simulate the sediment and nutrient transport near a groin using 3D software.
- The model can be applied for different spacing between two groins to study the effect of spacing.
- The study can be extended for different groin length to channel width ratios to study the effect of groin length to the flow field and sediment transport.

REFERENCES

- Ahmad, M. (1951), Spacing and protection of spurs for bank protection, *Civil Engineering and Publication Review*, 46, 3-7.
- Ahmad, M. (1953), Experiments on design and behaviour of spur dikes. In *Proceedings: Minnesota International Hydraulic convention* (pp. 145-159). ASCE.
- Barbhuiya, A.K., & Dey, S. (2004). Local scour at abutments: A review. *Sadhana*, 29 (5), 449-476.
- Chow, V.T. (1959). "Open-channel hydraulics". Mc Graw-Hill Book co., Inc., New York, N.Y.
- De-Vriend, H.(1980). "Velocity redistribution in curved rectangular channels." *J. Fluid Mech.*, 107, 423-439.
- De-Vriend, H. (1981). "Flow measurement in a curved rectangular channel. Part 2: Rough bottom." Internal Rep. No. 5-81. Tech. Rep., Laboratory of Fluid Mechanics, Dept. of Civil Engineering, Delft Univ. of Technology, Delft, The Netherlands.
- Davinroy, R. D.(1990). Bendway Weir Concept in the Mississippi River, *Proceedings, International Association of Navigation Congress, Secille, Spain*, pp. 115-123.
- Davinory, R. D. (1994). The Bendway Weir, A New Structural Solution to Navigation Problems Experienced on the Mississippi River, *International Association of Navigation Congresses, Bulletin 69, Osaka, Japan*, pp. 5-19.
- Fox, j.F., Papanicolaou, A.N., and Kjos, L.(2002). An Environmentally Friendly Barb design for Washington state, *Research and Extension Regional Water Quality Conference, February 20-21, Vancouver, WA*.
- Garde, R., Subramanya, K., & Nambudripad, K.D. (1961), Study of scour around spurdikes, *Journal of Hydraulics Division*, 86, 23-37.
- Gill, M.A. (1972), Erosion of sand beds around spur dikes. *Journal of Hydraulic Divison*, 98
- Hossain, S.A.A.M, Uddin, M.J., Ali, M. S. (2012). "Effect of stream barb on straight channel bed configuration: Numerical simulation". *ICCESD-2012, KUET, Khulna, Bangladesh*.
- Hasen, E. M. and Winter, E. R. (1996). Abstract 0027: design abstract for barb. Northwest Region Hydraulic Section (Draft).

Jamieson, E.C., Rennie, CD., Townsend, R.D. (2013). Turbulence and Vorticity in a Laboratory Channel Bend at Equilibrium Clear-Water Scour with and without Stream Barbs. *J. Hydraul. Eng., ASCE*, 139: 259-268.

Kim, T.B. and Choi, S.U. (2003). “conducted an experiment on numerical simulations of open-channel flows in a bend using the finite element method”. School of Civil and Environmental Engineering, Yonsei University, Seoul, Korea.

Kuhle, R. A., Alonso, C.V., & Shields, F.D. (1999), The geometry of Scour holes associated with 90 spur dikes, *Journal of Hydraulic Engineering*, 125 (9), 972-978.

Kothyari, U.C., & Rangaraju, K.G. (2001), K.G. (2001), Scour around spur dikes and bridge abutments. *Journal of hydraulic research*, 39 (4), 367-374.

Karami, H., Basser, H., Ardeshir, A., & Hosseini, S.H. (2014), Verification of numerical study of scour around spur dikes using experimental data. *Water and Environment journal*, 28(1), 124-134.

Kang, J., Yeo, H., Kim, S., & Ji, U. (2011). Experimental investigation on the local scours characteristics around groynes using a hydraulic model. *Water and Environmental Journal*, 25 (2), 181-191.

Lloyd, P.M. and Stansby, P. K. (1997). Shallow-water flow around model conical islands of small side II: submerged. *J. Hyd. Engr., Asce*, 123 (12), pp. 1068-1077.

NRCS (2005), Technical Note 23, Design of stream Barbs (Version 2.0). U.S. Department of Agriculture, Portland, Oregon. Oregon Bulletin No. OR210-2005, pp 1-25.

Quanhong, L., Pengzhi, L.(2007). Numerical Simulation of Recirculating Flow Near a Groyne. The 2nd International Conference on Marine Research and Transportation. Ischia. Naples. Italy, pp. 61-68.

Rajaratnam, N. and Nwachukwu, B.(1983) ‘Flow near Groin-like Structure’,*Journal of Hydraulic Engineering*, 109 (3): 463-480.

Rozovskii, I.L. (1961). “Flow of water in bends of open channels.” Academy of Science of krainian SSR, Russia.

Shimizu, Y. (2002). A method for simultaneous computation of bed and bank deformation of a river, *Proceedings of the International Conference on Fluvial Hydraulics, River Flow 2002*, Louvain-la-Neuve, Belgium, vol. 2, pp 793-802, September, 2002.

Schiechl, H. M. and R. Stern. (1996). Water Bioengineering Techniques for Watercourse, Bank and Shoreline protection. Trans by L. Jaklitsch. Blackwell Scientific. Oxford, UK. P.185.

Sarveram, H., Shamsai, A., Banihashemi, M.A. (2012). Two-dimensional simulation of flow pattern around a groyne using semi-implicit semi-Lagrangian method. International Journal of Physical Science, Academic Journals, 7(20): 2775-2783.

Shields Jr, F.D., Cooper, C.M., & Knight, S.S. (1995), Experiment in stream restoration Journal of Hydraulic Engineering, 121(6), 494-502.

Tingsanchali, T. and Maheswaran, S.(1990) '2-D Depth-averaged Flow Computation near Groyne' Journal of Hydraulic Engineering, 116(1):71-86.

USDA, (2001). Design of Stream Barbs, Technical Notes, Engineering No. 12, Version 1.4, US Department of Agriculture, Natural Resources Conservation Service, Boise, ID.